NORTHWESTERN UNIVERSITY

New Insights from Network Theory and Analysis: From the Mechanics of Granular Materials to the Robustness of Cellular Metabolism

A DISSERTATION

SUBMITTED TO THE GRADUATE SCHOOL
IN PARTIAL FULFILLMENT OF THE REQUIREMENTS

for the degree

DOCTOR OF PHILOSOPHY

Field of Chemical and Biological Engineering

By

Ashley Gerard Smart

EVANSTON, ILLINOIS

December 2007

To my mother, Linda Smart, and my brother, Carl Smart, Jr.

– in your memory I find inspiration.

ABSTRACT

New Insights from Network Theory and Analysis:
From the Mechanics of Granular Materials to the Robustness of Cellular Metabolism

Ashley Gerard Smart

Granular matter and living cells represent two extremes of what have come to be regarded as *complex systems* – systems characterized by a richness in global behavior that is not easily deduced from the interactions of their individual parts, even when those interactions are simple and well understood. On the one hand, granular matter is perhaps the simplest prototype of a complex system, whereas living cells are among the most complex of the complex systems studied in science.

Recently, network theory has emerged as a valuable framework for analyzing, classifying, and understanding complex systems. In this dissertation, we use networks – applying established analysis techniques as well as developing new techniques – to investigate specific problems pertaining to granular matter and cellular metabolisms. From network analysis we gain new insights into (1) the distributions of particle pressures in bi-disperse granular packings; (2) the structural evolution of a gradually tilted granular bed; (3) the transport properties of granular media; and (4) the relationship between

structure and robustness of cellular metabolisms. The studies on granular systems are supported by particle dynamics simulations; the study on metabolic robustness is supported by genome-scale *in silico* reconstructions of *Escherichia coli*, *Saccharomyces cerevisiae*, *Methanosarcina barkeri*, and *Staphylococcus aureus*.

Acknowledgements

I am grateful to have been advised over the course of my dissertation work by Julio M. Ottino. His guidance – always thoughtful and insightful – has helped me to mature as a researcher and as a writer. I am also grateful to have worked with Paul Umbanhowar, who has served as a co-advisor for portions of my dissertation. His comments, critiques and suggestions have helped to bring clarity and focus to my research. I also thank Luis Amaral for valuable discussions regarding network analysis techniques.

I am very appreciative of the discussions and feedback provided by current and former members of the Ottino group, including: Pengfei Chen, Stephen Cisar, Jim Gilchrist, Gabe Juarez, Dean Malmgren, Steven Meier, Nick Pohlman, Benjamin Severson, Ben Socie, and Kurt Smith.

Finally, I am grateful for the seemingly endless support provided by my friends and family – first and foremost among them, my father, Carl Smart Sr.

Table of Contents

List of Tables

List of Figures

CHAPTER 1

Overview and Organization

Nearly every facet of life involves complexity. Even simple, individual actions (flying from New York to L.A., viewing a website, turning on a light switch) are made possible by a complex underlying system of interacting parts (the air traffic system, the internet, the electrical power grid). Complex systems have resisted traditional paradigms – they are characterized by a richness in global behavior that is not easily deduced from the interactions of their individual parts, even when those interactions are simple and well understood. They exhibit emergence, self-organization and adaptability [**1**]. They are observed in physical, biological, social, and economic systems [**2**]. While complex systems are not new – complexity long predates humankind – the capacity to analyze, classify, and understand complex systems has only recently begun to emerge as a science. Tools such as cellular automata and networks are being developed into a framework for the systematic study of these kinds of systems. But much remains to be learned. In this dissertation, we investigate specific problems pertaining to two classes of complex systems – granular matter and cellular metabolism – from the vantage point of network analysis.

1.1. Granular Matter, Living Cells: Unique Examples of Complex Systems

Granular matter can be loosely defined as matter composed of discrete, solid particles – it represents perhaps the simplest prototype of what have come to be known as complex systems [**3**, **4**]. Interactions between individual particles are relatively simple and well

understood – interparticle contacts are repulsive, frictional, dissipative and, in some cases, adhesive. But knowledge of these interactions reveals little about the collective behavior of the system. The simple rules that govern granular interactions yield a surprisingly rich array of phenomena: fingering at the leading edge of the granular front in a rotating tumbler [**5**], localized excitations in a shallow vibrated granular bed [**6**], and spontaneous segregation in shaken or rotated systems [**7**–**10**] are just a few examples. In fact, no single description can universally describe granular matter – under various conditions, it can behave like a solid, liquid, or gas [**11**].

At the other end of the spectrum, living cells are among the most complex of the complex systems studied in science. Whereas the components in a granular system (solid particles) are similar and behave virtually identically (i.e., they obey Newton's laws of motion), the components in a cell comprise numerous distinct classes and functional groups, each with very specialized tasks – ATP synthase is responsible for producing energy from adenosine diphosphate; messenger RNA carry genetic information to ribosomes for protein synthesis. Whereas granular particles interact, indiscriminantly, with whichever particles are nearby, cellular components must be transported – often selectively – to allow for very specific interactions. Granular materials experience only a few types of stresses – e.g., compression, shear. Cells, however, must adapt to temperature fluctuations, changes in food supply, pH, mutations, and other stresses, while maintaining the ability to perform critical processes such as reproduction and metabolization.

Although they represent extrema, granular matter and cellular systems both typify the evolution of the complex system as a new paradigm. Isaac Newton's early attempt to describe force propagation in granular matter was simple and deterministic – grain

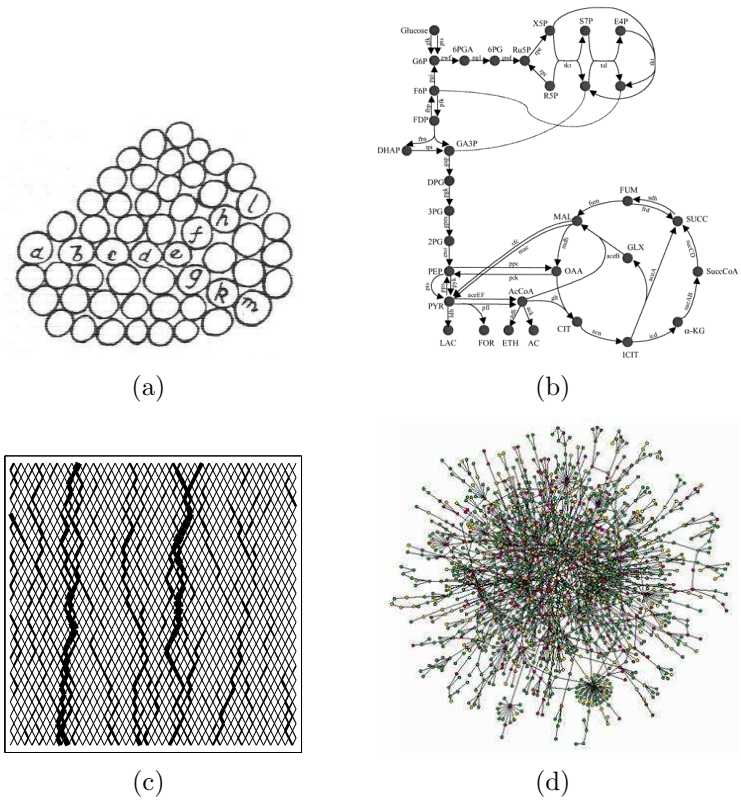

Figure 1.1. **The evolution of the complex system as a new paradigm.** (a) A sketch from Isaac Newton's *Principia* describes force propagation in a granular system – grain a presses against b, which presses against c, and so on (Image from [**12**]). (b) The pathway representation of glycolysis, a metabolic process (from [**13**]). Although (a) and (b) are both valid descriptions, they are limited. Neither comes close to capturing all aspects of the underlying complexity. The emergence of new analytical tools have redefined our view of complex systems. They include cellular automata – such as the 'q' model which is used to describe forces in a granular packing (c) – and networks – such as those used to describe metabolic structure in living organisms (d) (from [**14**]) .

'a' presses against grain 'b', which presses against 'c', and so on [**12**] (See Fig. 1.1a). Similarly, the earliest conceptualizations of the cell metabolism resembled assembly lines, comprising sets of independent, linear reaction pathways (Fig. 1.1b). But recently, new descriptions and tools have emerged. For example, forces in granular matter are frequently studied from the vantagepoint of ensemble theory [**15**], or cellular automata [**16**]; the cell metabolism is now widely regarded as a highly interconnected set of reactions and metabolites. In both cases, scientific understanding has been aided by the arrival and development of a new framework – networks.

1.2. Networks, and Complex Systems Analysis

We define a network as a system of nodes (vertices) connected by edges (links). Adopting this definition, the 'network' description can be applied to an extraordinary range of systems – language patterns [**17**], transportation systems [**18**], social interactions [**19**], etc. In fact, any system composed of interacting parts can be described as a network. Perhaps the biggest recent impact of network theory has been to reveal underlying similarities between systems that, at first glance, appear completely unrelated.

In this dissertation we apply the network framework, separately, to granular and cellular systems. In studying granular systems, we are concerned primarily with granular packings – that is, granular matter in a solid-like, compressed state. In studying cell behavior, we focus on cellular metabolism – the process by which nutrients are converted into energy, waste, and cellular components.

1.3. Organization

The dissertation is organized into two parts. Part I deals with granular packings, and comprises three independent case studies. In Case Study I (Pressure in a Bi-disperse Granular Packing), we investigate effects of of particle size dispersity on the structure of forces in granular networks. In Case Study II (Forces in a Tilted Bed), we use network concepts to gain insight into the granular phenomenon of shear failure. Finally, in Case Study III (Effects of Self-Organization on Transport in Granular Matter), we explore the relationship between granular network structure and transport properties. Part II of the dissertation deals with the cell metabolism. Specifically, we explore the relationship between structure and robustness of metabolic networks (Case Study IV: Robustness of Metabolic Networks). We conclude with a brief discussion of some potential future research directions regarding granular and metabolic networks.

Each of the case studies are self-contained, with a methods section, results, and a brief discussion. Also, each case study has self-consistent notation (whenever possible, we use consistent notation throughout the whole of the dissertation, but occasionaly, variables are defined differently for different case studies). Also, each chapter is preceded by a brief sentence or phrase – extracted from the body of the chapter – that reflects an essential finding or result. The phrase is followed by an abstract-like introduction; together, they are meant to orient the reader with the ensuing chapter material.

CHAPTER 2

Introduction to Part I

'granular force structure can be distinguished by a unique hallmark – heterogeneity and self-organization.'

In 1957, a relatively simple experiment performed by Dantu – in which photoelastic disks were compressed by a piston – provided the first true glimpse of how force propagates through a granular system [**20**]. The result was remarkable. Stresses were localized into an intricate, weaving network of chains. Granular systems – at scales on the order of several particles – deviated significantly from the often assumed continuum approximation. The result spawned a new paradigm in granular physics, and a new challenge: to understand the origins of granular micro-structure, and its implications towards macroscale phenomena. Ensuing studies have confirmed, in precise and quantitative terms, what Dantu observed in his early experiment: granular force structure can be distinguished by a unique hallmark – heterogeneity and self-organization.

2.1. Heterogeneity and Self-Organization in Granular Matter

Experiments [**22**–**26**], phenomenological models [**22**,**27**,**28**], particle dynamics simulations [**22**,**23**,**29**], Monte Carlo simulations [**15**,**30**,**31**], thermodynamics analogies [**32**,**33**], and analytical solutions [**34**] indicate that a relatively few inter-particle contacts in a granular packing tend to support most of the compressive load. The remaining contacts

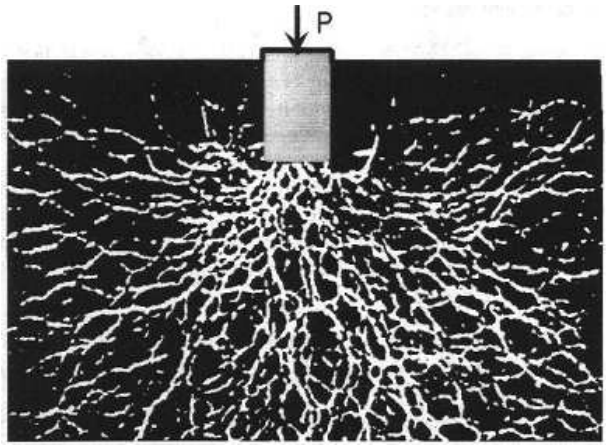

Figure 2.1. **An unusual medium.** Dantu's experimental with photoelastic rods compressed by a piston reveals an intricate network of force chains. Image from [**21**]

support little. This yields a force probability distribution function $p(f)$ that has a broad-tail at high forces. The precise form of $p(f)$ remains an open issue. In jammed packings of rigid particles, evidence supports exponential decay of $p(f)$ at large f, with a peak at small f [**24**, **25**]. Such packings are well described by the relationship proposed by Mueth *et al.* [**24**]:

$$p(f) = \alpha \left[1 - \beta \exp(-f^2)\right] \exp(-\gamma f) \tag{2.1}$$

where the coefficients are $\alpha \approx 3, \beta \approx 0.75$ and $\gamma \approx 1.5$. (Fig. 2.2, curve b)

If the packing is at or above the jamming transition (i.e., slow flow) the peak at small f disappears, and $p(f)$ decays monotonically [**35**, **36**]. In (2.1), this corresponds to $\beta \to 0$. (Fig. 2.2, curve a)

It has been argued – from a theoretical basis – that if particles are either (1) very soft, or (2) allowed to freely explore the entire phase space, as by tapping, the large force

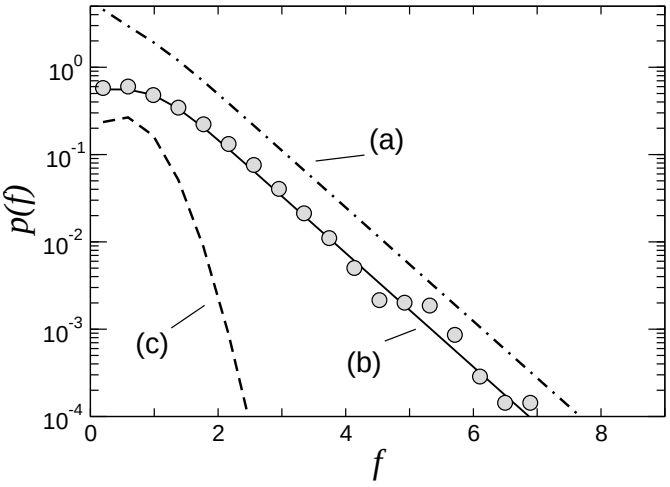

Figure 2.2. **The contact force distribution for a vertically compressed granular packing.** The data represent the contact force distribution, $p(f)$, for a typical granular packing used in this dissertation. The data exhibit a peak at small forces and exponential decay at large forces, and are described by eq. (2.1), with coefficients $\alpha = 3$, $\beta = 1.78$, and $\gamma = 1.5$ (curve (b)). Curve (a) represents an upper limit, and is typical of granular packing near the the jamming transition. Curve (c) represents a lower limit, and has been proposed for granular packings of either very soft particles, or particles allowed to freely explore the entire phase space (as explained in the text).

decay of $p(f)$ may be faster than exponential, approaching Gaussian [**23**, **32**, **37**]. (The γf term in (2.1) approaches γf^2, see Fig. 2.2, curve *c*)

The force distributions observed for the packings used in this dissertation exhibit a peak at small forces and exponential decay at large forces, consistent with (2.1), with coefficients $\alpha = 3$, $\beta = 1.78$, and $\gamma = 1.5$ (See Fig. 2.2).

Although less precisely understood, elements of self-organization in granular matter are also evident, and are extensively documented in the literature: spatial and force correlations are known to extend over distances on the order of tens of particles [**38**]; strong and weak contacts have been found to comprise sub-groups that align along opposing axes

in response to shear [**39**]; and so-called *force chains*, chains of highly compressed particles, are observed to interconnect, forming intricate sub-networks [**40**].

2.2. Some Open Questions

The heterogeneous, self-organized nature of granular force structure complicates several questions that might otherwise be straightforward:

- **When does size matter in a granular packing?** Granular materials rarely consist of uniformly sized particles. In fact, a distribution of sizes is often desired – space filling arrangements of large and small particles are known to enhance strength in materials such as concrete [**41**]. But how small is too small? How is load distributed between small and large particles, and when do the small particles become irrelevant?
- **What causes granular matter to flow?** Shear failure, perhaps more than any other granular phenomenon, generates widespread interest: geologists and civil engineers aim to predict the occurrences of avalanches, mudslides, and earthquakes [**42**,**43**]; chemical and process engineers aim to know why different materials flow at different tilting angles [**44**, **45**]; physicists aim to understand jamming and its relation to the glass transition [**46**, **47**]. Although certain structural precursors to the flow transition are known – increasingly large fluctuations [**48**]; anisotropy in $p(f)$, with $p(f)$ in the shear direction exhibiting monotonic decay [**49**]; emergence of a percolating network of contacts at the Coulomb friction limit – current understanding of shear failure is, at best, incomplete.

- **How does granular matter transport heat?** Granular materials are unusual transport media. A sound wave initiated at one end of a granular packing is dispersed and distorted when it reaches the other end [**50**–**52**]. Metallic powders heat and coalesce non-uniformly when sintered. A slight change in pressure is the difference between 'on' and 'off' in a conducting granular switch [**53**]. Each of these behaviors are sensitive to granular force structure.

The ability to answer such questions hinges on our capacity to distill detailed structural data into physically meaningful information. It is here that the network viewpoint has emerged as a useful paradigm.

2.3. A Networks Framework

In Part I of the dissertation, we employ the network description to investigate some of the questions listed above. We represent each particle as a node, i. Two nodes i and j are connected by an edge, c_{ij}, if the particles are contacting (see Fig. 2.3). The normal force along the contact defines an edge weight, f_{ij}. On occasion, we will employ a 'vector' edge form, $\vec{c}_{ij}$, where $\vec{c}_{ij}$ is the vector connecting the centers of two contacting particles i and j (generally, the direction in which the vector points is unimportant, i.e., $\vec{c}_{ij}$ and $\vec{c}_{ji}$ are interchangeable. The edge weight, f_{ij}, is always scalar and positive.

The network viewpoint is accompanied by new statistical methods – including concepts such as percolation, clustering, and new measures of distance [**54**]. However, the application of these tools to granular matter is not straightforward. We develop some of these tools for application to specific problems in granular physics. The resulting tool set includes both established and new concepts: in some instances we simply tailor

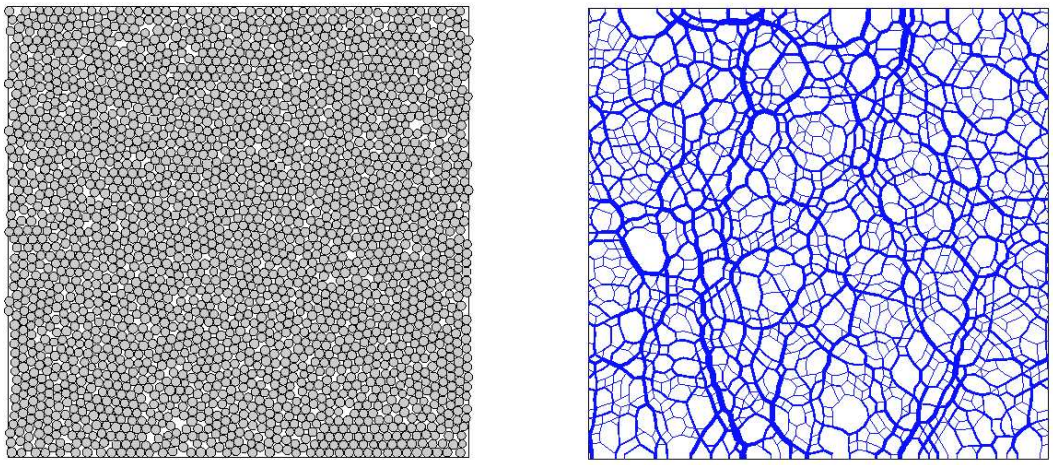

Figure 2.3. **The granular packing as a network.** (Left) A granular packing, consisting of two-dimensional disks between vertical walls. (Right) The network representation. Each line (edge) represents an interparticle contact; the width of the line (edge weight) corresponds to the normal force along the contact.

conventional granular concepts to the networks view, whereas other instances represent a significant leap from the traditional granular paradigm (and can be thought of as tailoring networks concepts to the granular view).

We can organize the tool set according to scale. At one extreme, we analyze the granular network based on the statistics of single elements – contacts and particles. Such measures provide the basis for Case Studies I (Partitioning of Pressure in Bi-Disperse Granular Media) and IIa (Evolving Forces and Structure in a Gradually Tilted Bed: Predicting Stress). At a slightly larger scale, we can consider structural motifs comprised of a few clustered elements. This is our approach in Case Study IIb (Evolving Forces and Structure in a Gradually Tilted Bed: Loops and Fragility). A third subset of tools can be used to analyze network structure and organization at a scale much larger than the

grain size – these tools guide our approach to Case Study III (Effects of Self-Organization on Transport in Granular Matter). All work is supported by 2-D particle dynamics simulations (see Appendix).

CHAPTER 3

Case Study I: Pressure in Size Bi-disperse Granular Packings

'...the subsets (of large and small particles) display different statistics from the whole, and each other.'

Most granular systems – natural, industrial, and experimental – have size dispersity. In materials such as cement, detergent, and soil, particle sizes may vary by an order of magnitude or more. In experiments, size-dispersity is often introduced to generate random packing structures. Still, the influence of size dispersity on the granular force structure remains imprecisely understood, largely because disperse systems are frequently analyzed much like monodisperse systems – all particles, regardless of size, are treated as a single set and assumed to share common statistical properties. Rarely are forces and stresses distinguished according to particle size. But stress properties within a granular packing *are* size dependent – the subsets (of large and small particles) display different statistics from the whole, and each other.

In this chapter, we look separately at the force statistics of small and large particles in bi-disperse packings, observing notable traits: (1) smaller particles are more likely to experience extreme (either very low or very high) pressures; and (2) although pressure distributions for small and large particles are very different, there is a special region where their average pressures are the same. This region, which we call the *equipartion*

region, spans a large range of size and fill ratios. We use numerical simulations to predict the 'equipartition' region, and consider its dependence on material properties such as interparticle friction.

3.1. Methods

We simulate two-dimensional systems of rough disks using Particle Dynamics – normal contact forces are calculated using the linear-spring dashpot model, and tangential forces are calculated using the Cundall and Strack model (See Appendix). We consider systems with interparticle friction equal to $\mu = 0.5$ and 0.2. Packings are prepared by compression – a fixed force is applied to the horizontal walls, compressing the granular system to a specified vertical pressure, P_y, and yielding a static, nearly isotropic granular packing. The final system dimensions approximate a square. The granular system is bounded in the vertical direction by infinitely rough walls – where we impose a no-slip condition – and in the horizontal direction by a periodic boundary. (See Fig. 3.1)

Particle size distributions are bi-disperse, with size ratios of small to large particles, $d^* = d_s/d_l$, ranging from 0.1 to 1. For each size ratio, we consider a range of volume fractions, ϕ_s, where ϕ_s is the volume fraction of small particles:

$$\phi_s = \frac{n_s \pi (d_s/2)^2}{n_s \pi (d_s/2)^2 + n_l \pi (d_l/2)^2}. \tag{3.1}$$

where n_i is the total number of particles of type i. (See Fig. 3.2)

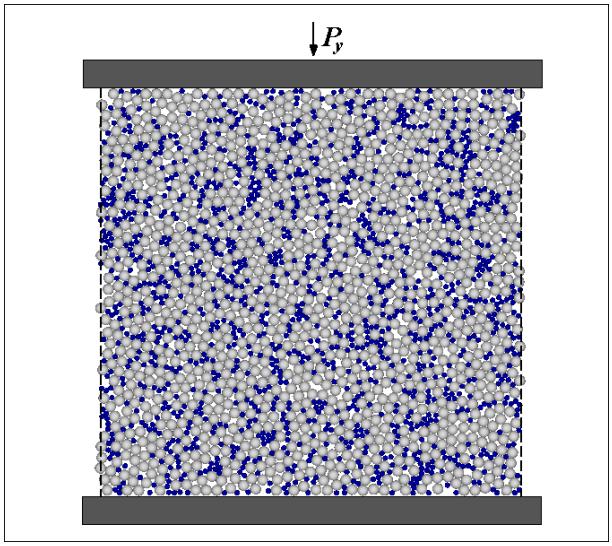

Figure 3.1. **Bidisperse granular packing, compressed between vertical walls.** 1250 large particles (gray) and 1250 small particles (blue) with size ratio $d^* = 0.5$ and coefficient of friction $\mu = 0.5$, compressed vertically to a pressure of P_y. The volume fraction of small particles, ϕ_s, is 0.2.

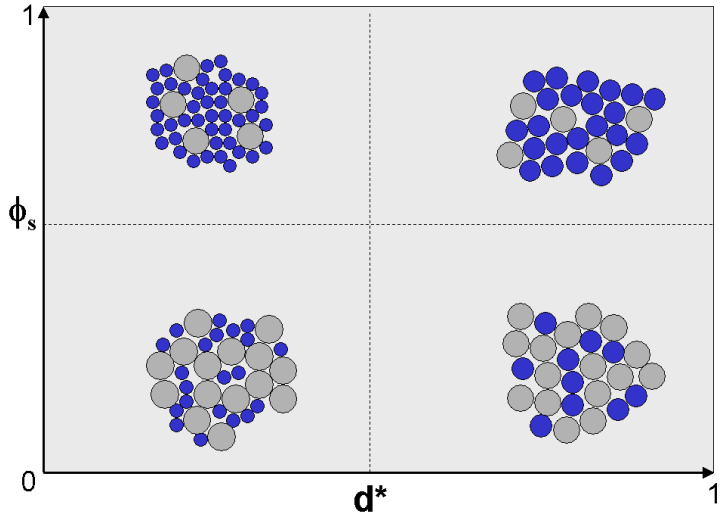

Figure 3.2. **The d^*, ϕ_s parameter space.** Large particles are shaded gray, small particles are blue.

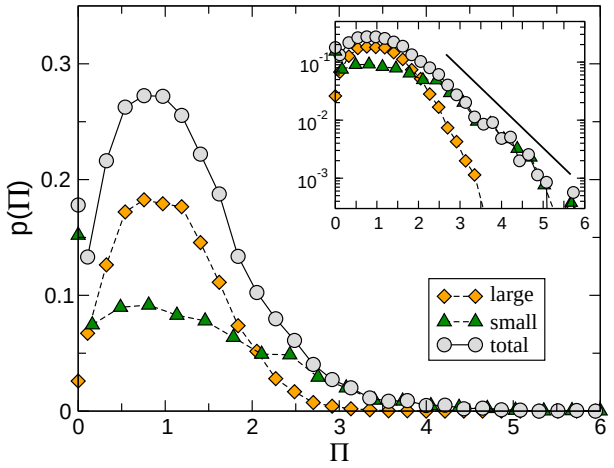

Figure 3.3. **The particle pressure distribution in a bidisperse packing.** The pressure distribution, $p(\Pi)$, shown for a packing with $d^* = 0.5$ and $\phi_s = 0.2$. The distribution has a peak at low pressures and decays exponentially at high pressures (see inset). $p(\Pi)$ can be viewed as the superposition of $p(\Pi_l)$(large particles) and $p(\Pi_s)$ (small particles). Note that there exists a finite probability for $\Pi = 0$, i.e. $p(\Pi = 0), p(\Pi_s = 0)$, and $p(\Pi_l = 0)$ are greater than 0. (Π values have been normalized with respect to the mean.)

3.2. The Pressure Distribution, Decomposed Into Subsets

We define the particle pressure, Π_i, as the average pressure acting on the surface of a particle i:

$$\Pi_i = \frac{1}{\pi d_i} \sum_j f_{ij} \tag{3.2}$$

where j are neighboring particles. We can then calculate the probability distribution function, $p(\Pi)$, for particle pressures in a granular packing. Like $p(f)$, $p(\Pi)$ is heterogeneous and broad-tailed, with most particles experiencing low pressure a few experiencing high pressure (See Fig. 3.3, and contrast inset with Fig. 2.2). The pressure distribution has a peak at low pressures and decays exponentially at large pressures.

We gain a more complete picture by decomposing $p(\Pi)$ into its small and large subsets, $p(\Pi_s)$ and $p(\Pi_l)$ (Fig. 3.3). We take a system with $d^* = 0.5$ and $\phi_s = 0.2$ as an example, noting that

(1) The pressure distribution for small particles, $p(\Pi_s)$, is broader than for large particles, $p(\Pi_l)$ (we say that $p(\Pi_s)$ has greater *breadth*); and

(2) despite markedly different distribution curves, the total pressure is partitioned equally between small and large particles, that is, $\overline{\Pi}_s$ and $\overline{\Pi}_l$ are nearly the same (this can be seen more clearly in Fig. 3.4, as discussed below).

To our knowledge, (1) has been neither discussed nor formally acknowledged in the existing literature. In what follows, we quantify the effect and offer a physical explanation. Equal partial pressures (2) was first observed by Tsongui *et al.* [**55**] for 2-D packings with the following d^*,ϕ_s pairs: $0.6, 0.45$; $0.4, 0.30$; and $0.4, 0.49$. We extend their work, looking at a broader range in the d^*, ϕ_s parameter space.

3.3. An Explanation for the Dependence of Breadth on Particle Size

The distribution $p(\Pi_s)$ is – over the entire range of d^* and ϕ_s – broader than $p(\Pi_l)$. Physically, this means that smaller particles are more likely than large particles to experience extreme pressures – either very small or very large. The difference can be quantified in terms of breadth, b:

$$b = \Pi^{20} - \Pi^{60} \tag{3.3}$$

where Π^x is the value for which $P(\Pi > \Pi^x) = x$. b can be visualized on the cumulative distribution function, $P(\Pi > \Pi')$ (See Fig. 3.4). In general b_s is larger than b_l, and

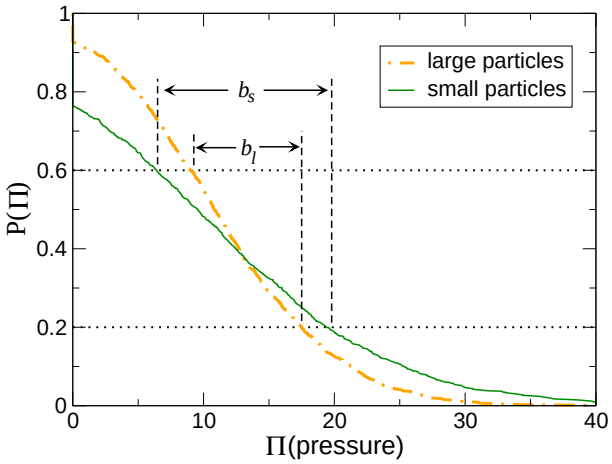

Figure 3.4. **Breadth, and the particle pressure distribution.** The cumulative distribution function, $P(\Pi > \Pi')$, is shown for a packing with $d^* = 0.7$ and $\phi = 0.4$. The breadth, b, is equal to $\Pi^{20} - \Pi^{60}$, where Π^{20} and Π^{60} are the values for which $P(\Pi > \Pi^{20}) = 0.2$ and $P(\Pi > \Pi^{60}) = 0.6$, respectively.

the difference between the two increases with the difference in particle size (i.e., $b_s - b_l$ increases as d^* goes to zero, see Fig. 3.5a). The phenomena can be explained by concepts of sampling statistics.

Consider a sample of n events, where the value, v_i, of an individual event is drawn from some arbitrary distribution, $p(v)$. The mean value of the sample is q:

$$q = \frac{1}{n}\sum_{i}^{n} v_i \tag{3.4}$$

The variance of the resulting probability distribution, $p(q)$, is inversely related to sample size. Specifically,

$$\sigma_q \propto n^{-1/2}, \tag{3.5}$$

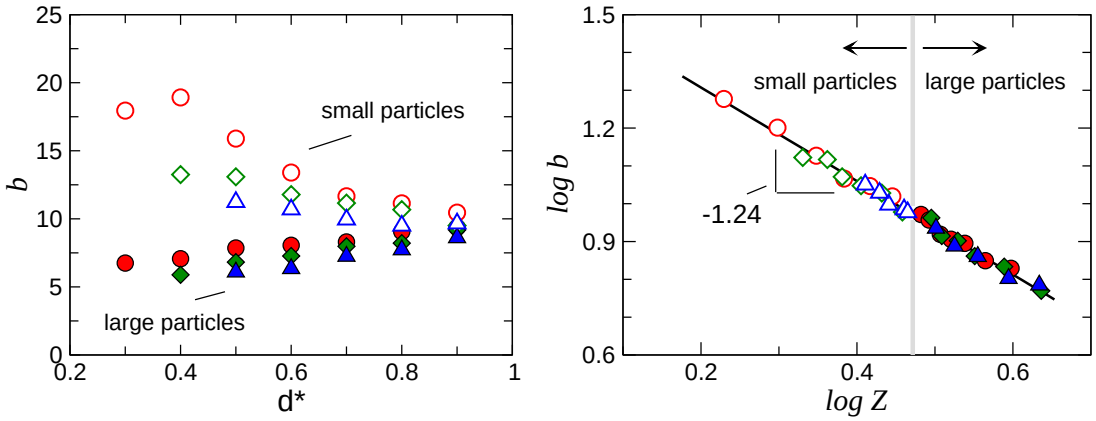

Figure 3.5. **Breadth as a function of particle size, coordination number.** (a) Breadth, b, of the pressure distribution is greater for small particles than for large; the difference increases with increasing size disparity (decreasing d^*). (b) b is inversely related to coordination number, Z, with all data collapsing onto the curve $b \propto Z^{-1.24}$. Key – $\triangle(\phi_s = 0.2)$; $\diamond(\phi_s = 0.4)$; $\circ(\phi_s = 0.6)$. Filled and outlined symbols denote large and small particles, respectively, in each bi-disperse packing.

where σ_q is the variance – or, precisely, the standard deviation – of the resulting distribution of q values. In other words, as more samples are taken, the mean of the sampled group more precisely estimates the mean of the entire set.

In the granular packing, analogues to q, n and v are Π, Z and f, respectively, where Z is the coordination number, and f is contact force. Each particle pressure, Π_i, then represents the average of a sample of Z_i contacts, whose values are drawn from the contact force distribution, $p(f)$. It follows that the variance, or breadth, of $p(\Pi)$ should decrease as Z increases. (Since smaller particles have lower coordination number, it also follows that b should be largest for small particles). A fit of the data (Fig. 3.5b) confirms that b is inversely related to Z, specifically:

$$b \propto Z^{-1.24} \tag{3.6}$$

b is an unusually strong function of Z (compare to equation (3.5)). This is likely because the 'sampling' of forces by a particle in a granular packing is correlated, not random; selection of one extreme value of f increases the probability of selecting additional values of f from the same extreme. This exaggerates the normal variation that would occur in random sampling.

3.4. Equal (and Unequal) Partitioning of Pressures

Close inspection reveals that the areas under the curves $P(\Pi_s)$ and $P(\Pi_l)$ in Fig. 3.4 are approximately equal; i.e., the average pressures $\overline{\Pi}_s$ and $\overline{\Pi}_l$ are approximately the same. This tendency of granular matter towards equal 'partial pressures' is not obvious – it was only recently shown to occur in two-dimensional size bi-disperse systems (peculiarly, 3-D packings do not exhibit equal partitioning of pressures) [**55**].

Equal partial pressures occurs over a limited range in the d^*, ϕ_s parameter space. Below some critical size ratio, d^c, equipartition of partial pressures breaks down, yielding $\overline{\Pi}_s < \overline{\Pi}_l$. In [**55**], it is posited that d^c corresponds to the size ratio at which small particles can fit in the interstices between large particles. For a triangular packing of large particles, this is $d^c \approx 0.15$. We find that d^c in a frictional system can be much larger, and is a function of the volume packing ratio ϕ_s. Regions of equal and unequal partitioning can be represented on the d^*, ϕ_s parameter space (See Fig. 3.6).

Equipartition breaks down when both d^* and ϕ_s are small, i.e. when the difference in size between the two classes of particles is large *and* the system is composed mostly of large particles (we say that large particles form the matrix). The curve $d^c(\phi)$ separates

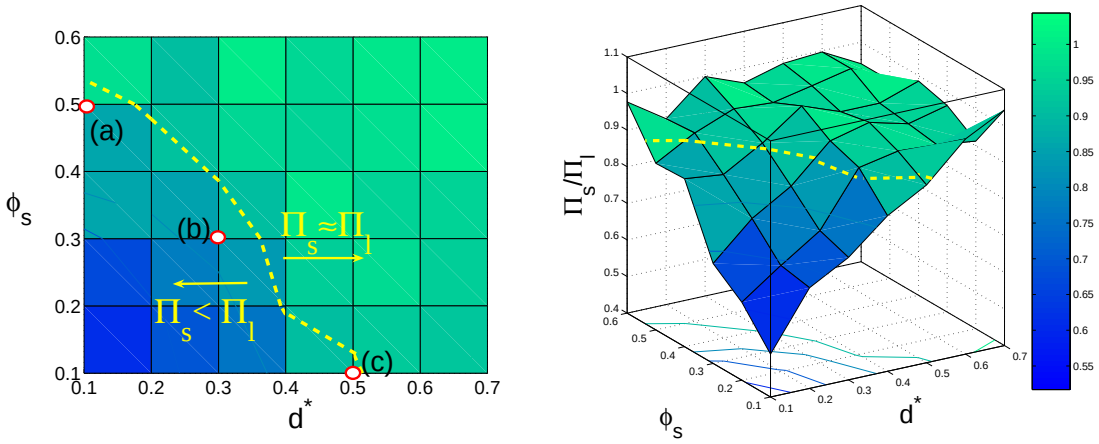

Figure 3.6. **Regions of equal and unequal partial pressures,** $\mu = 0.5$**.** The ratio $\Pi^* = \overline{\Pi}_s/\overline{\Pi}_l$ drops sharply for $d^* < d^c(\phi_s)$, indicating unequal partitioning of pressure. d^c is approximated by the iso-curve, $\Pi^* = 0.9$ (dashed line). The points a, b, and c on the d^*,ϕ_s parameter space correspond to the packings shown in Fig. 3.7.

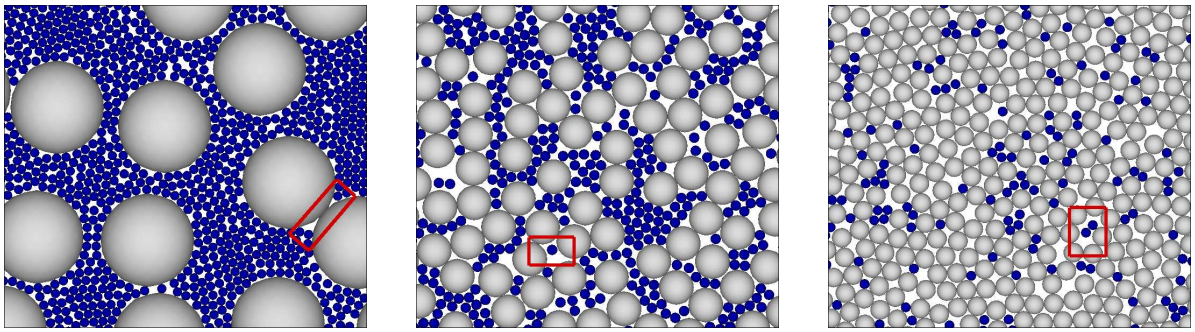

(a) $d^* = 0.1, \phi_s = 0.5$ (b) $d^* = 0.3, \phi_s = 0.3$ (c) $d^* = 0.5, \phi_s = 0.1$

Figure 3.7. **Near-critical packings in the** d^*, ϕ_x **parameter space.** Boxed areas indicate shielded, low pressure areas.

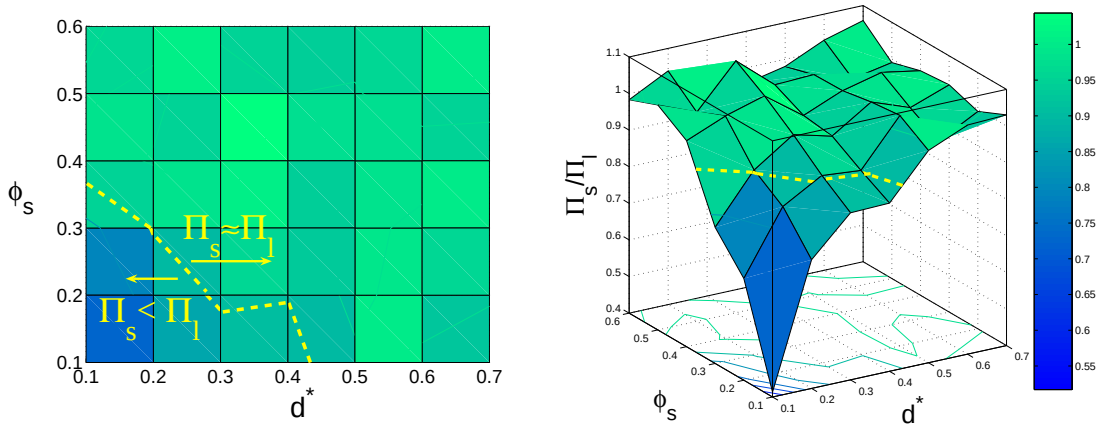

Figure 3.8. **Regions of equal and unequal partitioning of pressure, $\mu = 0.2$.** The ratio $\Pi^* = \overline{\Pi}_s/\overline{\Pi}_l$ drops sharply for $d^* < d^c(\phi_s)$, indicating unequal partitioning of pressure. d^c is approximated by the iso-curve, $\Pi^* = 0.9$ (dashed line).

regions of equal and unequal partition. Below d^c, in the non-equipartition region, Π^* decreases approximately linearly as either d^* or ϕ_s is decreased.

One explanation for the breakdown of equipartition may be that, at certain size ratios and fill fractions, larger particles tend to 'shield' smaller particles from the external compressive force. For example, consider a packing with $d^* = 0.1$ and $\phi_s > 0.5$. The packing consists of large particles in a matrix of small particles, and the probability that two large particles touch is virtually zero. The packing displays equal partitioning of pressure. As ϕ_s is decreased to $\phi_s \approx 0.5$, the volume fill fraction of small particles is small enough that large particles may touch each other (See Fig. 3.7a). Small particles lying in the space near one of these large-large contacts may be shielded from the external compressive force; the area near the large-large contact is effectively a 'low-pressure' area (this area is denoted by the red-box in Fig. 3.7a). As ϕ_s is decreased further, large particles touch more frequently, and more low-pressure areas are created.

At larger values of d^*, more large particles are needed to form a shielded space. For example, at $d^* = 0.3$, small particles are too large to fit in the area between two, or even a cluster of three contacting large particles. But a cluster of four or five large particles form a shielded space large enough to encompass small particles (See Fig. 3.7b). At $d^* = 0.5$, clusters of five to six large particles may form a sufficiently large shielded space (Fig. 3.7c).

The equipartition results above are for frictional packings with $\mu = 0.5$. For $\mu = 0.2$, the behavior is qualitatively similar, but equipartition occurs over a larger range in the d^*, ϕ_s parameter space (see Fig. 3.8).

3.4.1. A Virtual Work Solution

Tsoungui *et al.* predict equipartition in 2-D packings, on the basis of 'virtual work' [**55**]. Specifically, they propose the following relationships for partial pressures:

$$\Pi_s = \frac{P_{ext}}{\rho}\left(1 - \frac{d^*}{\rho\phi_s}\frac{\partial\rho}{\partial d^*}\right) \tag{3.7}$$

$$\Pi_l = \frac{P_{ext}}{\rho}\left(1 + \frac{d^*}{\rho(1-\phi_s)}\frac{\partial\rho}{\partial d^*}\right) \tag{3.8}$$

where P_{ext} is the externally applied pressure and ρ is the packing density. It follows that $\Pi_s = \Pi_l$ *if and only if* $\frac{\partial\rho}{\partial d^*} = 0$. If $\frac{\partial\rho}{\partial d^*}$ is negative, small particles experience greater pressure; the opposite is true if $\frac{\partial\rho}{\partial d^*}$ is positive.

It is unclear whether our results can be reconciled with the virtual work solution, as outlined above. Although we do find $\frac{\partial\rho}{\partial d^*} = 0$ in the equipartition region, we find $\frac{\partial\rho}{\partial d^*} < 0$

in the region with $\Pi_s < \Pi_l$, which seems to contradict the virtual work solution. The observed disagreement may be related to so-called *rattlers*, particles with $\Pi = 0$, which are presumed to be absent from the packings modeled by Tsoungui *et al.*, but may be present at large concentrations in the granular packings considered in this study. Also, an important assumption in the Tsoungui model is that all contact forces are identical; this assumption does not accurately describe most granular packings (see Section 2.2).

3.5. Discussion

The distinctions between forces on small and large particles in a size-bidisperse granular packing can be intriguing. Both of the primary results discussed above – that small particles are more likely to experience extreme pressures, and that equipartion of pressure occurs over a limited region – may have important practical implications. Consider, for example, the fragmentation of rocks or powders by crushing, a process relevant to both geology and powder technology [**56**]. It is possible that the differences in stress experienced by small and large particles in a packing may affect both overall crushing rates and final particle size distributions.

There are several possible extentions to the current work. More simulations, and perhaps experiments, should be performed to understand the relationship between our 'shielded space' hypothesis, and the virtual work model. Also, we have considered a single preparation method, and just two friction coefficients; it may be interesting to know if other preparation methods friction coefficients result in different $d^c(\phi_s)$ behavior.

CHAPTER 4

Case Study IIa. A Gradually Tilted Bed: Predicting Stress

'We derive a relationship describing the rate of memory loss...(which) appears to apply universally to packings with various friction coefficients.'

Perhaps the single defining characteristic of a granular packing is its response to shear stress – it dictates material strength as well as slow flow properties; it determines the occurrence of mudslides and gives rise to surprising segregation patterns in mixtures [**57**–**59**]. The shear response, however, is not easily predicted, even when the contributing material properties – particle shape, size, surface roughness, hardness, and adhesion – are known [**60**]. In fact, nonuniformity of granular packings means that the shear stress itself is often ill-defined and difficult to describe (even stresses in a symmetric granular pile, a relatively simple system, can be puzzling [**61**, **62**]).

Shear in granular matter is complicated by *memory* effects – stresses in a granular packing depend on the history of its preparation (this is why we leave behind footprints while walking along a beach). In turn, granular memory – and memory loss – depends on material properties such as friction and adhesion (this is why footprints left in wet sand look very different from those left in dry sand). This results in a unique mechanics problem, where internal stresses depend not only on boundary conditions, but also preparation and material properties. [**42**, **43**, **63**]

In this chapter, we investigate a prototypical granular system exhibiting memory and memory loss – a bed prepared via sedimentation and then gradually tilted under gravity. The preparation process results in residual shear stress, or memory, which slowly vanishes as the system is tilted. Accordingly, stresses within the bed evolve in a non-trivial manner. We propose a physical model describing stress evolution in the tilted bed, premised on the concept that the stress tensor is decomposable into two independent contributions: a *residual stress* contribution, which decreases with tilting angle, and a *gravity-induced* stress contribution, which increases with tilting angle.

In what follows, we (1) generate a dimensionless scaling relationship, collapsing stress data for beds with various friction coefficients onto a single curve; and (2) derive a relationship describing the rate of *memory loss* (the rate at which the residual stress contribution decreases) as a function of tilting angle. The dimensionless form of the memory loss function appears to apply universally to packings with various friction coefficients. Importantly, the results suggest that the scaling relationship might be used to predict the marginal angle of stability – prior to failure – from stress data sampled over a small tilting range.

4.1. Methodology

Randomly packed beds are generated by a sedimentation process (see Appendix). The horizontal boundary is periodic (no vertical walls), and the floor is infinitely rough, i.e., particles touching the floor are not permitted to move horizontally. Particle radii are normally distributed with a variance equal to 10 percent of the mean in order to prevent crystallization. The bed is $120d$ wide and approximately $20d$ deep, where d is the mean

particle diameter (Fig. 4.1a). We examine the role of interparticle friction, considering various packings over the range $0 \leq \mu \leq 0.5$, where μ is the Coulomb friction coefficient.

The tilting protocol begins after particles have been allowed to fully settle and equilibrate in the bed. We fix the orientation of the bed and allow θ_g, the angle of the gravity vector with respect to vertical, to increase in increments (for low tilting rates, this is equivalent to fixing the orientation of gravity and incrementally tilting the bed). See Fig. 4.2a for a definition of the tilting angle, θ_g. We alternate one-second tilting intervals (constant rotation rate of 0.01 rad/sec) with one-second rest intervals, allowing fluctuations caused by tilting to dissipate prior to generating each network matrix. We only consider networks formed at tilt angles at or below the marginal angle of stability. That is, the data and analysis in this and the next chapter apply to quasi-static, solid-like granular packings, *not* flowing material.

The resulting packing can be viewed as a network (See Fig. 4.1b). Due to gravity, contact forces, f, in the network tend to increase with depth. We remove this effect by normalizing contact force with respect to depth:

$$f'_{ij} = \frac{f_{ij}}{(H - y_{ij})/H} \tag{4.1}$$

where y_{ij} is the vertical position of the contact. H is the depth of the bed,

$$H = 2\frac{1}{n_c}\sum y_{ij} \tag{4.2}$$

where n_c is the number of contacts, and the sum is taken over all contact pairs. We exclude the top two layers of contacts – contacts with $(H - y_{ij}) < 2d$ – from our analysis, in order to avoid unrealisticly high values of f'_{ij}. The normalized network yields a more

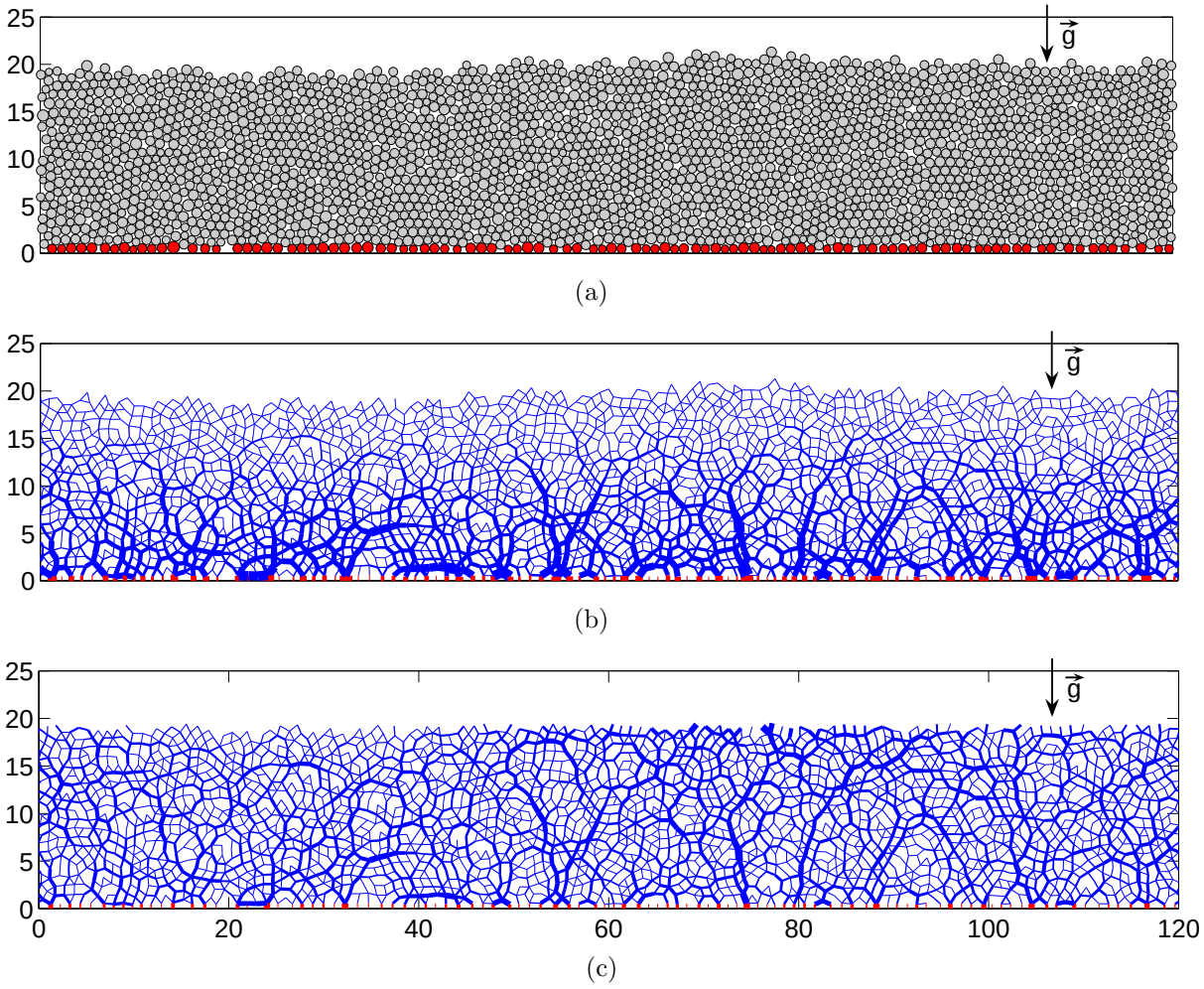

Figure 4.1. **The granular bed as a network**. *(a)* 2500 granular particles are allowed to settle under gravity and come to rest, forming a granular bed about 20 particle diameters deep and 120 particles in length (although the horizontal boundaries are periodic). The layer of particles touching the bed (shaded red)are fixed in place approximating an infinitely rough floor. *(b)* The bed can be represented as a network, where each contact is represented by an edge, and each edge is weighted according to the normal force along its corresponding contact. Thicker lines near the base signify a pressure gradient: pressure increases with increasing vertical depth. *(c)* The same network with edges normalized with respect to depth, so that the average edge weight of a layer is independent of its depth.

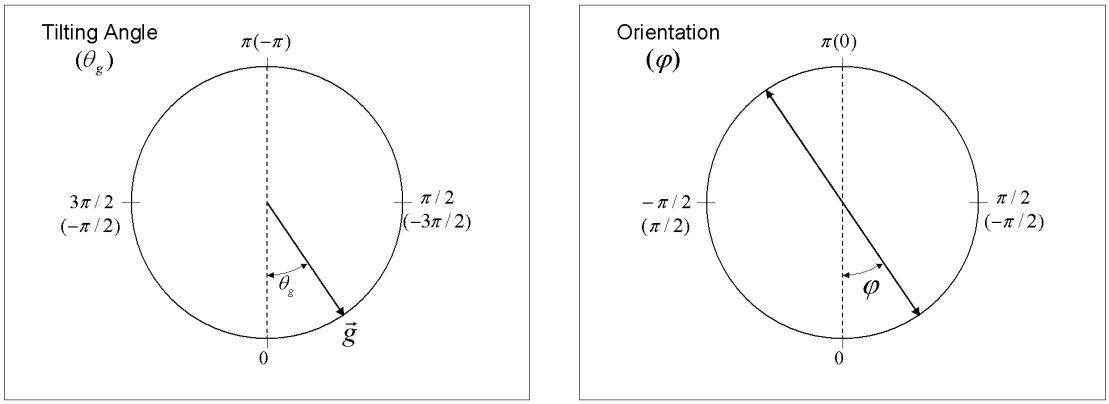

Figure 4.2. **Defining tilting angle, orientations.** (a) In tilting experiments, it is the direction of gravity – not the bed – which is tilted. During initialization, the gravity vector is directed downward. The tilting angle, $\theta_g = 0$, is the angle formed between the gravity vector and the downward vertical, such that a counterclockwise motion of the gravity vector corresponds to an increase in θ_g. θ_g has 2π periodicity. (b) φ, which we use to define stress orientation, is similar to θ_g, except that stress, unlike gravity, is symmetric: it acts equally and oppositely in both directions along a line. As a result, φ has π periodicity (e.g., there is no distinction between the vertical downward and vertical upward directions). In both figures, the values in parenthesis indicate the equivalent direction or orientation measured in the clockwise direction.

accurate average of the dimensionless shear stress and the shear orientation (See Fig. 4.1c).

4.1.1. Calculating the Stress Tensor: Dimensionless Shear and Orientation

We wish to derive the dimensionless shear stress and shear orientation for each granular network. To do so, we calculate the angular variation of the normal stress, $\sigma(\varphi)$, by averaging the individual contributions of each contact in the network (See Fig. 4.2b for

a definition of orientation, φ). The individual contribution, $\sigma_i(\varphi)$, of a contact i depends on its orientation and force:

$$\sigma_i(\varphi) = \xi_i f_i \left(\vec{c}_i \cdot \vec{e}_\varphi\right)^2 \tag{4.3}$$

where $\vec{e}_\varphi$ is the unit vector in the direction φ , $\vec{c}_i$ is the contact vector, f_i is the force along contact i, and ξ_i represents the contact density for contacts oriented in the direction $\vec{c}_i$, which yields the desired units of force per unit area. (We do not calculate ξ_i explicitly, rather we take ξ_i to be constant and independent of contact orientation; the term then cancels upon non-dimensionalization of the stress tensor.) The average normal stress varies with φ as

$$\sigma(\varphi) = \frac{1}{N}\sum_{i}^{N} \sigma_i(\varphi) \tag{4.4}$$

The resulting function $\sigma(\varphi)$ can be described by a sine wave:

$$\sigma(\varphi) = a + b\sin(2(\varphi - \varphi_o)) \tag{4.5}$$

such that the principal stresses, σ_1 and σ_2, have magnitude $a \pm b$ (we adopt, as convention, $\sigma_1 = a+b$ and $\sigma_2 = a-b$) and the dimensionless shear stress, τ, has extrema $\tau^+ = \tau^* = b/a$ and $\tau^- = -\tau^*$ (See Fig. 4.3). φ_o indicates the orientations of the principal stress axes, $(\varphi^{\sigma,+}, \varphi^{\sigma,-})$, and the maximum shear planes, $(\varphi^{\tau,+}, \varphi^{\tau,-})$:

$$\varphi^{\sigma,+} = \varphi_o + \pi/4 = \varphi_o - 3\pi/4 \tag{4.6}$$

$$\varphi^{\sigma,-} = \varphi_o + 3\pi/4 = \varphi_o - \pi/4 \tag{4.7}$$

$$\varphi^{\tau,+} = \varphi_o + \pi/2 = \varphi_o - \pi/2 \tag{4.8}$$

$$\varphi^{\tau,-} = \varphi_o = \varphi_o \pm \pi \tag{4.9}$$

For example, if $\varphi_o = 0$, then the principal stress axes form 45 degree angles with the horizontal ($\varphi^{\sigma,+} = \pi/4, \varphi^{\sigma,-} = 3\pi/4$) while the shear stress has negative and positive extrema oriented along the horizontal and vertical axes ($\varphi^{\tau,+} = \pi/2, \varphi^{\tau,-} = 0$). (The stress tensor can be equivalently viewed as a Mohr Circle centered on $(a, 0)$, with radius equal to b.)

In the following section, we consider the evolution of τ^* and φ_o as functions of the tilting angle, θ_g. We review their qualitative behavior, and then put forth a quantitative model.

4.2. Predicting Qualitative Behavior of the Stress Tensor: Investigating Limits

Granular beds prepared via sedimentation (see Appendix) tend to exhibit stress anisotropy, even prior to tilting. The vertical pressure, σ_y, is typically larger than horizontal pressure, σ_x, such that the untilted bed has some initial shear stress, $\tau_o > 0$, and an initial orientation $\varphi_o(\theta_g = 0) = -\pi/4$ (that is, the maximum shear planes form 45 degree angles with horizontal). We call this initial shear stress, τ_o, the *residual* shear stress.

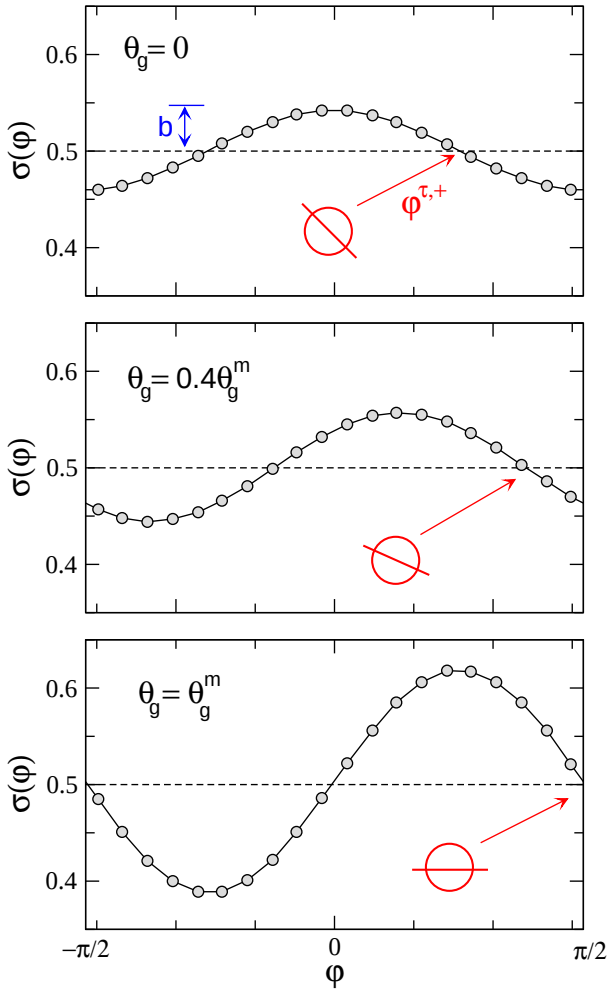

Figure 4.3. **Sine wave representation of the stress tensor of a granular bed, at various tilting stages.** The angular variation of normal stress, $\sigma(\theta)$, is described by a sine wave, where the amplitude, b, divided by the mean normal stress, $a = 0.5$ for the graphs shown here, yields the dimensionless shear stress, τ^*. As the tilting angle increases from 0 to the marginal angle of stability, θ_g^m, the orientation of the plane of maximum positive shear, $\varphi^{\tau,+}$, shifts from $\pi/4$ to the horizontal, $\pi/2$. (The plane of maximum positive shear for each curve is indicated by a line passing through a circle.)

As θ_g is increased from zero, the influence of the residual shear stress wanes, and gravity-induced shear stress increases. As θ_g approaches the angle of marginal stability, θ_g^m – the tilting angle beyond which steady flow occurs – we expect the following behavior. First, because steady shear flow is in the horizontal direction, we expect $\varphi^{\tau,+}$ to converge with $\pi/2$, the horizontal (i.e., $\varphi_o \to 0$ as $\theta_g \to \theta_g^m$). Second, as gravitational forces become the dominant source of shear, we expect τ^* to converge with the predicted dimensionless shear for a body resting on an incline:

$$\tau^*(\theta_g) = \tan\theta_g \tag{4.10}$$

We find that the limiting behavior of the simulated packed beds is in relative agreement with the expectations: φ_o increases from roughly $-\pi/4$ to 0 and $\tau^*(\theta_g)$ converges – particularly in beds with low μ – to $\tan\theta_g$ (see Figs. 4.4 and 4.5). In beds with higher μ, we find that $\tau^*(\theta_g) < \tan\theta_g$ for large tilting angles. This may be an effect of the rough floor – the distribution of particle-floor contacts may be skewed, not symmetric about the normal to the floor surface, such that the assumption of a flat surface overestimates the true incline between the bed and the floor. Similar behavior is found in the literature [**64**].

Above, we have shown that the properties of the stress tensor at the limits $\theta_g = 0$ and $\theta_g = \theta_g^m$ can be deduced in a rather straightforward manner; the quantitative transition between the two, however, is a much more complicated prediction. Below we propose a physical model for stress evolution in a tilted bed and show that, from it, we can derive a scaling relation describing φ_o as a function of θ_g.

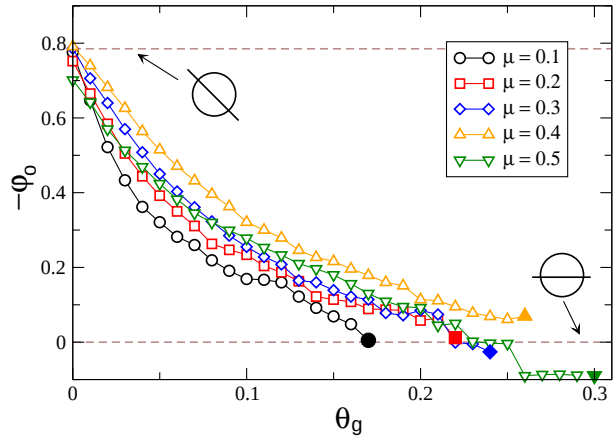

Figure 4.4. **Stress orientation as a function of tilting angle.** We plot data for granular beds with various Coulomb friction, μ. In each case, φ_o increases from roughly $-\pi/4$ to 0 (to plot data in the positive quadrant, we have plotted $-\varphi_o$). Filled markers indicate the marginal angle of stability, θ_g^m. The plane of maximum positive shear at each limit is indicated by a line passing through a circle.

4.3. The Relationship Between Tilting and Stress: A Physical Model

We develop a physical model on the premise that stress in the granular packing can be decomposed into two contributions: a residual stress contribution (whose normal and shear stress contributions we label as σ_r and τ_r, respectively) and a gravitational stress contribution (σ_g and τ_g). The orientations of the two contributions are fixed in space ($\varphi_{o,r} = -\pi/4$, $\varphi_{o,g} = 0$), and their maximum dimensionless shear stresses, τ_r^* and τ_g^* are functions of the tilting angle, θ_g. Based on these criteria, we can derive a relationship between the individual shear stress contributions, $\tau_r^*(\theta_g)$ and $\tau_g^*(\theta_g)$, and the orientation of the resultant stress tensor, $\varphi_o(\theta_g)$.

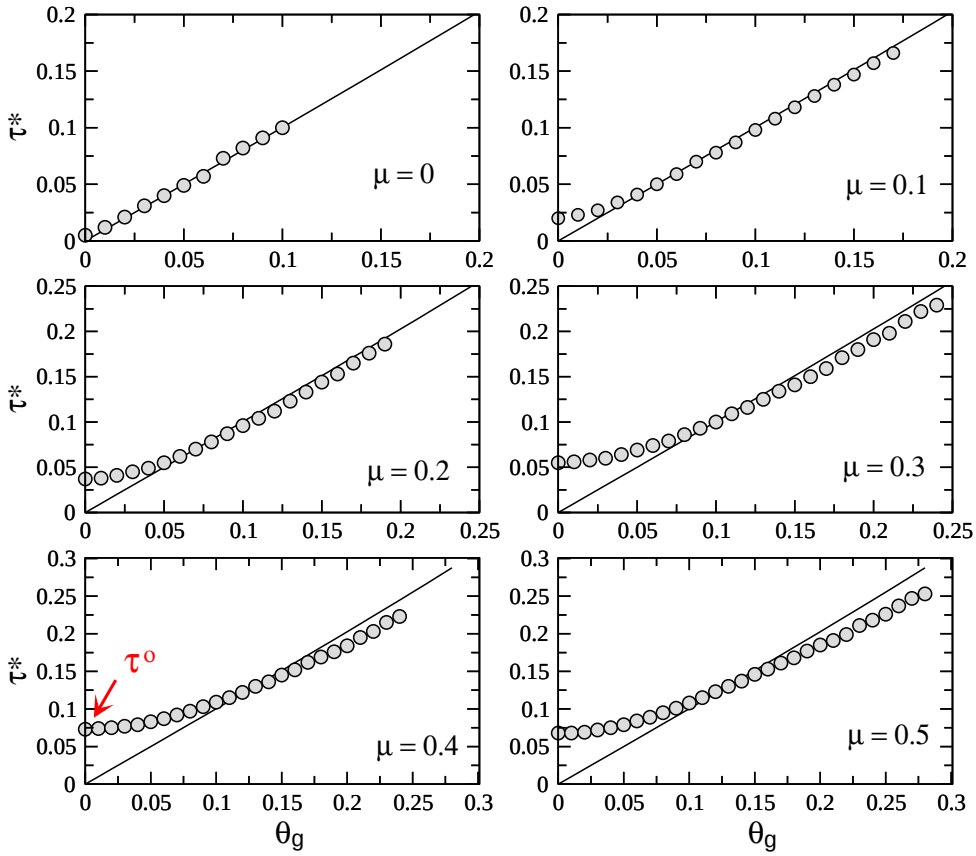

Figure 4.5. **Dimensionless shear as a function of tilting angle.** We plot $\tau^*(\theta_g)$ for granular beds with various Coulomb friction, μ. Frictional beds tend to exhibit significant residual shear, τ_o in the untilted state. As θ_g increases, τ^* tends to approach the expected limit for a solid body resting on an inclined plane, $\tan\theta_g$ (indicated by a solid line). Exceptions are the cases with high μ, for which it is proposed that the deviation, $\tau^* < \tan\theta_g$ may be an effect of the rough floor.

4.3.1. Calculating φ as a function of τ_r^*, τ_g^*

We begin by reviewing a relatively simple case: maximum shear orientation in a single stress field. Consider a box located in a stress field whose principal stresses are oriented along the x and y axes, such that $\sigma_y > \sigma_x > 0$, and $\tau_{xy} = \tau_{yx} = 0$ (see Fig. 4.6). When the box is tilted some angle, φ', and the stress field remains fixed, the stresses acting on

the surfaces of the box change as a function of φ'. Specifically,

$$\sigma_{y'}(\varphi') = \sigma_y \cos^2 \varphi' + \sigma_x \sin^2 \varphi' \tag{4.11}$$

$$\sigma_{x'}(\varphi') = \sigma_x \cos^2 \varphi' + \sigma_y \sin^2 \varphi' \tag{4.12}$$

The orientations of the principal stress axes, $\varphi^{\sigma,\pm}$, are recovered by maximizing or minimizing the difference $(\sigma_{y'} - \sigma_{x'})$ with respect to φ':

$$0 = \frac{d(\sigma_{y'}(\varphi') - \sigma_{x'}(\varphi'))}{d\varphi'} \tag{4.13}$$

$$0 = 4(\sigma_y - \sigma_x)(\cos \varphi^{\sigma,\pm} \sin \varphi^{\sigma,\pm}) \tag{4.14}$$

By definition, the maximum shear stress, τ^*, is equal to $1/2$ the difference of the principal stresses, $\sigma_y - \sigma_x$, so that

$$0 = 2\tau^*(\cos \varphi^{\sigma,\pm} \sin \varphi^{\sigma,\pm}) \tag{4.15}$$

In this case, we recover the original principal stress axes orientations, $\varphi^{\sigma,\pm} = 0, \pi/2$. As a rule, the maximum shear planes form 45 degree angles with the principal stress axes, such that $\varphi^{\tau,\pm} = \pm\pi/4$.

4.3.2. Stress field superposition

We now consider a slightly more complicated problem – superposition of the residual and gravity-induced stress tensors. The residual portion has principal stress axes, $\sigma_{r,1}, \sigma_{r,2}$,

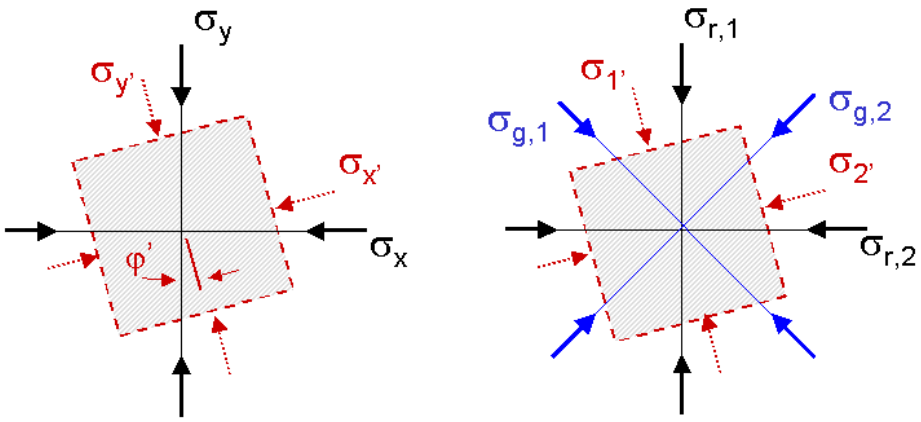

Figure 4.6. **Transforming stress as a function of orientation.** (left) We can calculate normal stress as a function of orientation, by considering a box subjected to a stress field with principal stresses σ_y and σ_y. If the box is tilted by some angle φ', new normal stresses are a function of tilt angle: $\sigma_{y'} = f(\sigma_y, \sigma_x, \varphi')$, $\sigma_{x'} = f(\sigma_y, \sigma_x, \varphi')$. (right) Angular variation of the normal stress resulting from two superimposed stress tensors ($\sigma_{r,1}, \sigma_{r,2}$ and $\sigma_{g,1}, \sigma_{g,2}$) can be calculated in a similar manner: $\sigma_{1'} = f(\sigma_{r,1}, \sigma_{r,2}, \sigma_{g,1}, \sigma_{g,1}, \varphi')$, $\sigma_{2'} = f(\sigma_{r,1}, \sigma_{r,2}, \sigma_{g,1}, \sigma_{g,1}, \varphi')$

with $\varphi_r^{\sigma,+} = 0$ and $\varphi_r^{\sigma,-} = \pi/2$ (so that the planes of maximum shear form 45° angles with the floor). The gravity-induced portion has principal stress axes $\sigma_{g,1}, \sigma_{g,2}$, with $\varphi_g^{\sigma,+} = \pi/4$ and $\varphi_g^{\sigma,-} = -\pi/4$ (so that the planes of maximum shear are horizontal and vertical, with respect to the floor, see Fig. 4.6). A box subjected to this stress field, and tilted at an angle, φ', from the vertical, experiences normal stresses

$$\sigma_{1'}(\varphi') = \sigma_{r,1}\cos^2\varphi' + \sigma_{r,2}\sin^2\varphi' + \sigma_{g,1}\cos^2(\pi/4 - \varphi') + \sigma_{g,2}\sin^2(\pi/4 - \varphi') \tag{4.16}$$

$$\sigma_{2'}(\varphi') = \sigma_{r,2}\cos^2\varphi' + \sigma_{r,1}\sin^2\varphi' + \sigma_{g,2}\cos^2(\pi/4 - \varphi') + \sigma_{g,1}\sin^2(\pi/4 - \varphi') \tag{4.17}$$

As previously, we can calculate the orientations of the principal stress axes by setting the derivative of the expression $(\sigma_{1'}(\varphi') - \sigma_{2'}(\varphi'))$ equal to zero:

$$0 = -4(\sigma_{r,1}-\sigma_{r,2})(\cos\varphi^{\sigma,\pm}\sin\varphi^{\sigma,\pm})+4(\sigma_{g,1}-\sigma_{g,2})(\cos(\pi/4-\varphi^{\sigma,\pm})\sin(\pi/4-\varphi^{\sigma,\pm})) \tag{4.18}$$

$$0 = -2(\tau_r^*)(\cos\varphi^{\sigma,\pm}\sin\varphi^{\sigma,\pm}) + 2(\tau_g^*)(\cos(\pi/4-\varphi^{\sigma,\pm})\sin(\pi/4-\varphi^{\sigma,\pm})) \tag{4.19}$$

We then get the expression

$$\frac{\tau_r^*}{\tau_g^*} = \frac{\cos(\pi/4-\varphi^{\sigma,\pm})\sin(\pi/4-\varphi^{\sigma,\pm})}{\cos\varphi^{\sigma,\pm}\sin\varphi^{\sigma,\pm}} \tag{4.20}$$

We consider $\varphi^{\sigma,+}$, recalling its relationship with φ_o:

$$\varphi^{\sigma,+} = \varphi_o + \pi/4 \tag{4.21}$$

Thus, we derive the following relationship between φ_o and the stress contributions τ_r^*, τ_g^*:

$$\frac{\tau_r^*}{\tau_g^*} = \frac{\cos(-\varphi_o)\sin(-\varphi_o)}{\cos(\varphi_o+\pi/4)\sin(\varphi_o+\pi/4)} \tag{4.22}$$

Eq. (4.22) indicates that φ_o – the lone variable on the right hand side – can be expressed in terms of the relative contributions of residual and gravity-induced shear stress – the ratio comprising the left hand side. As $\varphi_o \to \pi/4$ (which corresponds to the orientation of the residual shear stress), the denominator goes to zero, appropriately indicating that $\tau_r^* >> \tau_g^*$, and the residual portion is the sole contributor to shear stress. Likewise, as $\varphi_o \to 0$ (which corresponds to the orientation of gravity-induced shear stress), the numerator goes to zero, indicating that $\tau_g^* >> \tau_r^*$, and gravitational portion is the sole

contributor to shear stress. Next, we non-dimensionalize (4.22) and produce a scaling relationship for φ_o as a function of tilting angle.

4.3.3. Non-dimensionalization and scaling

We define the following dimensionless variables:

$$\overline{\theta}_g = \frac{\theta_g}{\theta_g^m} \tag{4.23}$$

$$\overline{\tau}_g^* = \frac{\tau_g^*}{\tau^m} \tag{4.24}$$

$$\overline{\tau}_r^* = \frac{\tau_r^*}{\tau^o} \tag{4.25}$$

where $\tau^m = \tau^*(\theta_g = \theta_g^m)$ and $\tau^o = \tau^*(\theta_g = 0)$. We can then restate (4.22) in terms of the dimensionless variables:

$$\frac{\overline{\tau}_r^*(\overline{\theta}_g)}{\overline{\tau}_g^*(\overline{\theta}_g} = \frac{\tau^m}{\tau^o} \frac{\cos(-\varphi_o(\overline{\theta}_g)) \sin(-\varphi_o(\overline{\theta}_g))}{\cos(\varphi_o(\overline{\theta}_g) + \pi/4) \sin(\varphi_o(\overline{\theta}_g) + \pi/4)} \tag{4.26}$$

We denote the right hand side of (4.26) as $\zeta(\varphi)$, so that

$$\frac{\overline{\tau}_r^*(\overline{\theta}_g)}{\overline{\tau}_g^*(\overline{\theta}_g} = \zeta(\varphi) \tag{4.27}$$

A plot of $\zeta(\varphi)$ versus $\overline{\theta}_g$ yields a collapse of the data for granular beds of various μ (see Fig. 4.7). Thus we can say – even prior to obtaining its specific form – that the function $\overline{\tau}_r^*(\overline{\theta}_g)/\overline{\tau}_g^*(\overline{\theta}_g)$ is universal. Next, we consider system constraints and propose functional forms for $\overline{\tau}_r^*(\overline{\theta}_g)$ and $\overline{\tau}_g^*(\overline{\theta}_g)$.

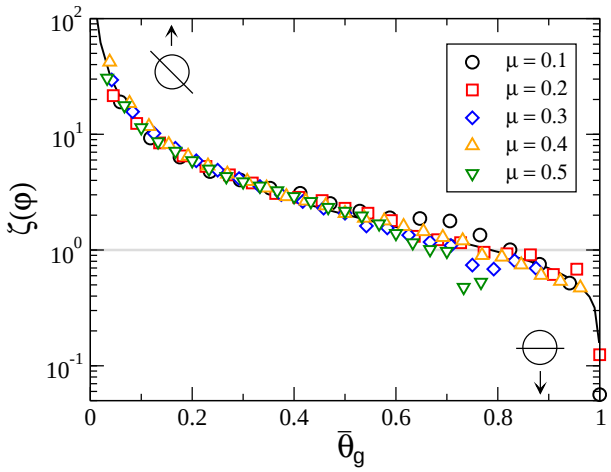

Figure 4.7. **Stress orientation scaling.** The right hand side of (4.26), defined as $\zeta(\varphi)$, is plotted against $\overline{\theta}_g$, showing a collapse of the data for granular beds with various Coulomb friction, μ. Lines passing through circles indicate the orientation of the planes of maximum shear for $\zeta(\varphi) >> 1$ and $\zeta(\varphi) << 1$, and the shaded line, $\zeta = 1$, indicates $\overline{\tau}_r^* = \overline{\tau}_g^*$. The solid line represents a fit of the data to the function $\overline{\theta}_g/(1-\overline{\theta}_g)^\lambda$, with $\lambda = 0.3$.

4.3.4. $\overline{\tau}_r^*$ and $\overline{\tau}_g^*$ as functions of $\overline{\theta}_g$

The functions $\overline{\tau}_r^*(\overline{\theta}_g)$ and $\overline{\tau}_g^*(\overline{\theta}_g)$ should display the following limiting behavior:

(4.28) $$\overline{\tau}_g^*(\overline{\theta}_g = 0) = 0$$

(4.29) $$\overline{\tau}_g^*(\overline{\theta}_g = 1) = 1$$

(4.30) $$\overline{\tau}_r^*(\overline{\theta}_g = 0) = 1$$

(4.31) $$\overline{\tau}_r^*(\overline{\theta}_g = 1) = 0$$

Over the tilting range considered in this study, the relationship $\tau_g^* = \tan\theta_g$, which defines gravity-induced shear on an inclined plane, is roughly linear (i.e., $\tau_g^* \approx \theta_g$). Thus, we propose a linearly increasing function for gravitational shear:

$$\overline{\tau}_g^*(\overline{\theta}_g) = \overline{\theta}_g \tag{4.32}$$

The function $\overline{\tau}_r^*(\overline{\theta}_g)$ defines the rate of memory loss – the rate at which the system loses the footprint of its initial preparation. $\overline{\tau}_r^*(\overline{\theta}_g)$ should decrease monotonically – but not necessarily linearly – from 1 to 0. We propose the form:

$$\overline{\tau}_r^*(\overline{\theta}_g) = (1 - \overline{\theta}_g)^\lambda \tag{4.33}$$

such that (4.26) becomes

$$\frac{(1 - \overline{\theta}_g)^\lambda}{\overline{\theta}_g} = \zeta(\varphi) \tag{4.34}$$

A nonlinear fit of the tilting data yields $\lambda \approx 0.3$.

4.4. Discussion

Our selected geometry, a granular bed with periodic horizontal boundaries, affords a convenient test of the hypotheses that (1) memory effects in a granular packing can be isolated from tilting effects, and (2) stress evolution can be modeled as a superposition of the two effects. Although the geometry is specific, the implications of the results are broad, and promising. We find not only that the superposition model can be used to describe stress evolution, but also that systems – when appropriately scaled – evolve in the same way, irrespective of interparticle friction. An important end result is a relationship

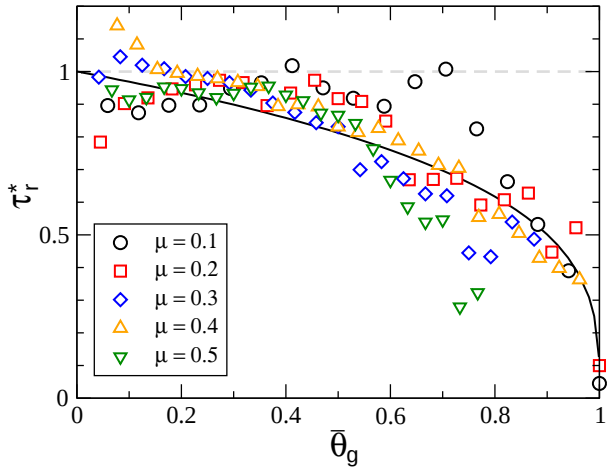

Figure 4.8. **Memory loss as a function of tilting**. We plot empirical values for the residual stress, $\overline{\tau}_r^*(\overline{\theta}_g) = \overline{\theta}_g \zeta(\overline{\theta}_g)$ as a function of $\overline{\theta}_g$. The function $\overline{\tau}_r^*(\overline{\theta}_g)$ defines the rate of memory loss – the rate at which the system loses the footprint of its initial preparation; The solid line represents a fit to the expression $(1 - \overline{\theta}_g)^\lambda$, with $\lambda = 0.3$.

that describes, quantitatively, how memory is lost as a granular bed is tilted. Such information may ultimately aid understanding of granular memory and memory loss in more complicated geometries.

CHAPTER 5

Case Study IIb. A Gradually Tilted Bed: Loops and Fragility

'...there are specific granular meso-structures – contact loops – which can support a finite range of compatible loads...the concentration and type of these structures present in a granular packing may indicate its stability.'

Stress evolution in a tilted bed implies complex, underlying dynamics in the granular network – new contacts are formed, old contacts are destroyed, and forces along enduring contacts change in magnitude as the bed is tilted. A practical question arises: do these changes have a coordinated effect on the structure of the granular packing, its strength and resilience? The prevailing view is yes – granule-scale changes that occur as a granular bed is tilted conspire to make it weaker and less resilient to perturbation [**48**]. This is why disturbing a level surface of sand results in only a localized failure (if any at all), while disturbing an inclined surface of sand is likely to trigger an avalanche.

This increased susceptibility to perturbation, known as *fragility*, is conceptually well understood. Cates *et al.* offer a precise description:

Its (fragile matter) incremental response can be elastic only to compatible loads; incompatible loads, even if small, will cause finite, plastic reorganizations. [**65**]

Although the dependence of fragility on structure is inherent, there currently exist no quantitative roadmap that relates the two. In this chapter, we probe structure-fragility relationships, revisiting the problem of the gradually tilted bed. We propose that there are specific granular meso-structures – *contact loops* – which can support a finite range of compatible loads, and that the concentration and type of these structures present in a granular packing may indicate its stability (and therefore, fragility). We find that contact loop structure in the granular bed (1) is sensitive to material properties; (2) deviates from the expected structure of a randomly wired lattice; and (3) is uniquely dependent on tilting angle. Furthermore, we introduce ξ as a quantitative measure of loop stability, and show that increased tilting results in a gradual destabilization of individual loops. The collective analysis yields a set of measurable structural changes characterizing the destabilization of a gradually tilted granular bed. (Again, the data and analysis in this chapter apply to quasi-static, solid-like granular packings, *not* flowing material.)

5.1. Contact Loops as Stable Structural Elements

A granular network can be viewed as a collection of meso-scale contact structures called *contact loops* (we define a contact loop as a path along the granular network that forms a non-intersected circuit) [**66**]. These loops are significant in that they are the smallest structural arrangements that can support load perturbation, as illustrated by the following thought experiment.

Consider three particles arranged in a straight line. The contact forces, f_{12} and f_{23}, define the external compressive forces, f_a and f_c, which are exerted at either end (see Fig. 5.1). It is easy to see that any orientational perturbations of the external compressive

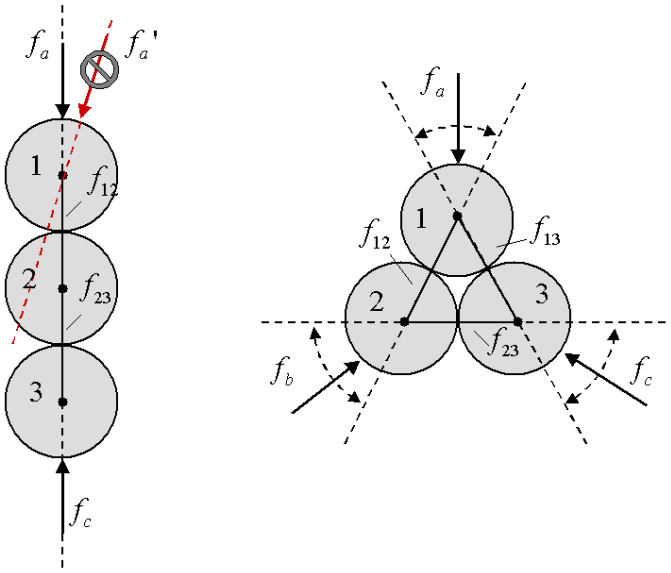

Figure 5.1. **Contact loops as stable meso-structures.** A linear contact structure (f_{12}, f_{23}) can support linear compression (f_a, f_b). But any perturbation of the compressive force (e.g., f_a') yields a load that is incompatible with the linear contact structure. For this reason we say that contact chains are *fragile*. On the other hand, contacts arranged in a triangular loop can support various compressive loads, f_a, f_b and f_c.

force results in an incompatible load [**65**]. Given the arrangement of particles, there is no combination of f_{12} and f_{23} that can support even a slight change in the direction of one of the externally applied forces. The incompatible load causes the linear contact structure to buckle.

Now consider the same particles arranged in a triangular loop, with contact forces f_{12}, f_{23} and f_{13}. Again, the contact structure defines a set of external compressive forces: f_a, f_b, and f_c. In this case, however, an orientational perturbation can be supported by an adjustment of the forces (f_{12}, f_{23} and f_{13}) *without* deforming the contact structure. In fact, we can define a finite range of compatible loads (the number of compatible arrangements is infinite), whereas the contact line has only one compatible load. The same is true for

larger contact loops and lines. For this reason, we say that contact loops are the smallest mechanically stable elements in a granular network; they can be viewed as the building blocks which comprise a stable network.

In the following sections, we investigate the statistics of contact loops in various granular networks. How often do loops arise? Which sizes are most prevalent? When do they destabilize and deform?

5.2. Contact Loop Statistics

Loops consisting of as many as seven edges occur with regularity in 2-D granular networks (see Fig. 5.2). Networks formed with smoother particles are denser and contain more low-order loops, whereas networks formed with rough particles are porous and more likely to contain higher order loops. In networks formed by particles with $\mu < 0.3$, third order loops are the most frequently occurring loop size; in those formed by particles with $\mu > 0.3$, fourth order loops occur most frequently.

The result suggests that networks formed by smooth particles are more stable (and less fragile) than those formed by rough particles – a conclusion stemming from the rationale that smaller loops, because they are more densely packed, are more stable to compression. It is reasonable, though perhaps not obvious, that rough particles should form more fragile networks. Higher friction granular systems are increasingly likely to jam far from equilibrium, forming more fragile networks.

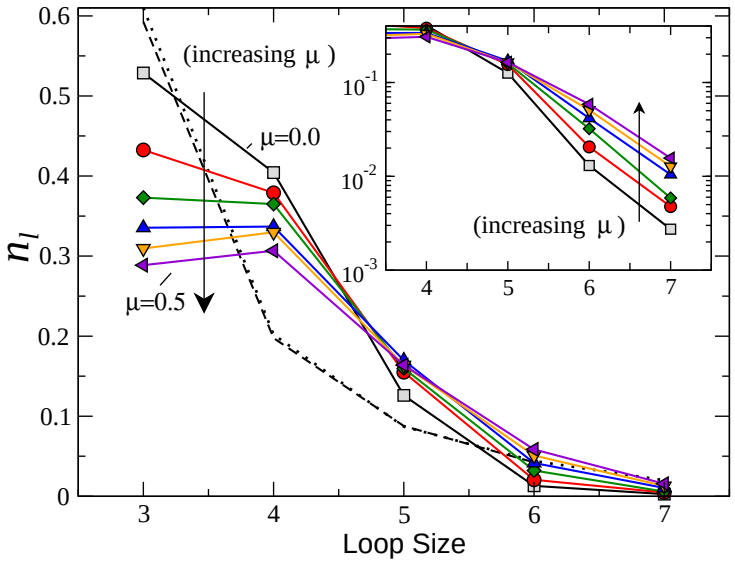

Figure 5.2. **Distributions of contact loops in untilted granular beds.** Loop fractions (n_l equals the total number of loops divided by the total number of nodes, or particles) are presented for granular systems with μ ranging from 0 to 0.5 (the tilting angle, θ_g, is zero. Increasing surface friction corresponds to a decreasing fraction of low order loops an an increasing fraction of high order loops. The dashed curve is the analytical solution for a randomly wired triangular lattice and the dotted curve is the numerical result from random rewiring in a granular network (both with $Z = 4$).

5.2.1. Loops in a Randomly Wired Lattice

We can compare loop statistics in the granular packing to those expected for a randomly wired lattice. We consider an infinite triangular lattice, with edges placed randomly between neighboring nodes. The probability, p_e of finding an edge between any two neighboring node pairs is

$$p_e = \frac{Z}{6} \tag{5.1}$$

where Z is the mean coordination number, or mean number of edges connected to a node ($Z = 2N_e/N_n$). It follows that the probability, $p_{l,3}$, that a group of three neighboring particles are connected by a triangular set of edges is equal to p_e^3. Since there are $2N_n$ unique potential triangular arrangements, the expected number of third-order loops is

$$N_{l,3}^{rand} = 2N_n p_e^3 \tag{5.2}$$

It is useful to represent the expected number of loops as a fraction:

$$n_{l,3}^{rand} = \frac{N_{l,3}^{rand}}{N_n} = 2p_e^3 \tag{5.3}$$

In a similar manner, we can derive $n_{l,4}^{rand}$. In this case $p_{l,4}$ is equal to $p_e^4(1-p_e)$, and the number of unique potential arrangements is equal to $3N_n$, resulting in

$$n_{l,4}^{rand} = 3p_e^4\,(1-p_e) \tag{5.4}$$

Using the same methodology for higher order loops, we obtain:

$$n_{l,5}^{rand} = 6p_e^5\,(1-p_e)^2 \tag{5.5}$$

$$n_{l,6}^{rand} = 20p_e^6\,(1-p_e)^3 + p_e^6\,(1-p_e)^6 \tag{5.6}$$

$$n_{l,7}^{rand} = 36p_e^7\,(1-p_e)^4 + 6p_e^7\,(1-p_e)^7 \tag{5.7}$$

We check the analytical prediction against the numerical outcome of randomly rewiring the neighboring particles in a granular packing, finding good agreement (compare dashed and dotted curves in Fig. 5.2).

Loop distributions in granular packings can differ significantly from the randomly wired lattice model – granular packings tend to have fewer third-order loops and more fourth-order loops than a randomly wired lattice (See Fig. 5.2). This is likely attributable to two factors. First the granular packing structure is not a triangular close-packed crystal, as per the randomly wired lattice, rather it approximates a glassy, random packing. Secondly, in the lattice model, we assume that nodes are connected to their neighbors with equal, random probability. However, the force balance constraint in real packings causes certain combinations of contacts to be preferable and more likely to occur than others.

5.2.2. Effects of Tilting on Loop Structure

Loop structure in the granular bed evolves as it is gradually tilted under gravity. Here, we focus on the changing fraction of third- and fourth-order loops. The third-order loop fraction decreases markedly as the bed approaches the angle of marginal stability indicating – according to the previously stated rationale – that the bed becomes more fragile as it is tilted (this agrees with our intuitive understanding of tilting and granular fragility)(See Fig. 5.3). The decrease in third-order loops, however, is tied to a decrease in coordination number, Z. A plot of $n_{l,3}$ versus Z shows that $n_{l,3}$, over the entire range of μ and all tilting angles, is a strong function of coordination number (See Fig. 5.4). From (5.3), we expect $n_{1,3} \propto Z^3$. The actual dependence observed in the granular packings is stronger.

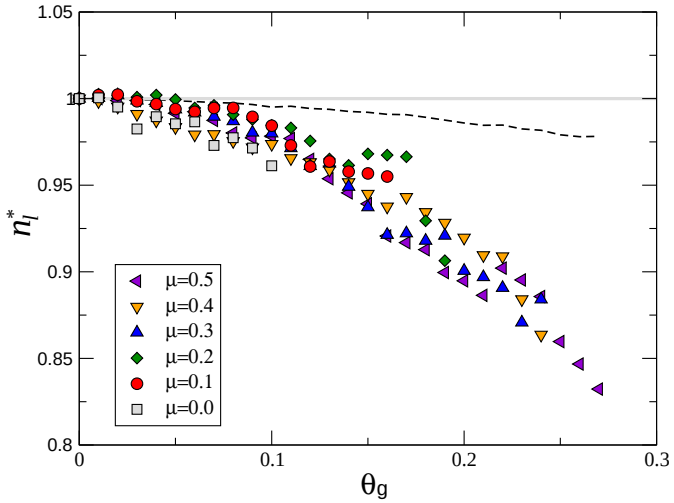

Figure 5.3. **Fraction of third order loops as a function of tilting angle.** The relative fraction of third order loops, $n_l^* = \overline{n}_l/\overline{n}_{l,o}$, tends to decrease with increasing tilting angle. This decrease is accompanied by a decrease in the mean coordination number Z (denoted by a dashed line).

A fit of the form

$$n_{l,3} = \alpha\,(Z-\beta)^{\gamma}\,, \tag{5.8}$$

yields $\alpha = 0.13$, $\beta = 1.39$ and $\gamma = 3.53$.

Note that the curve which describes $n_{l,3}(Z)$ as a function of packing density (i.e. $n_{l,3}(Z)$ in untilted beds with various μ) also describes $n_{l,3}(Z)$ over the tilted angles. As a result, we say that the effects of tilting on $n_{l,3}$ are *generic*: $n_{l,3}$ can always be described as a function of Z, and the tilting effect cannot be distinguished from packing density effects.

On the contrary, tilting has a unique effect on the fourth-order loop fraction, $n_{l,4}$. In granular beds with $\mu > 0.1$, $n_{l,4}$ tends initially to decrease with increasing tilting angle, then increase prior to reaching the marginal angle of stability (a possible explanation

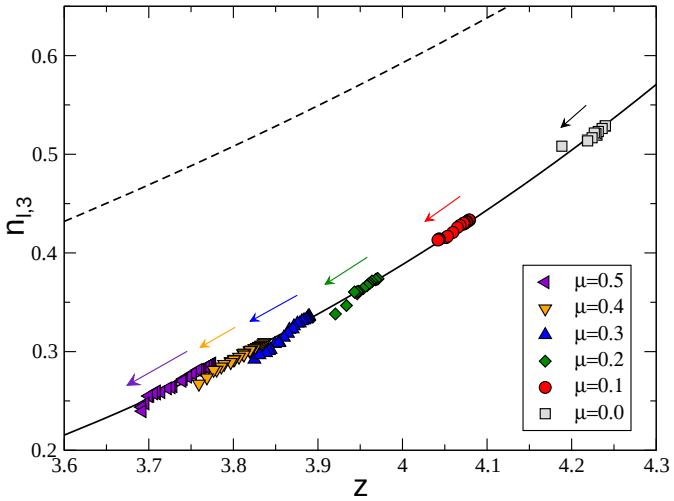

Figure 5.4. **Third-order loop fraction and coordination number.** From the randomly wired lattice model, we expect $n_{l,3} = 2(Z/6)^3$ (dashed curve). The data, however, are best fit by the functional form $\alpha(Z - \beta)^\gamma$, with $\alpha = 0.13$, $\beta = 1.39$, and $\gamma = 3.53$ (solid line). Data points for various packing densities and tilting angles lie on the same curve, indicating that tilting effects are *generic*. (Arrows indicate the direction of increasing tilting angle.)

is that third-order loops destabilize and become fourth-order loops as the system nears failure). Unlike $n_{l,3}$, the curve describing $n_{l,4}(Z)$ as a function of packing density tends to underestimate the fraction of of fourth-order loops when the bed is tilted, such that the tilting effect *can* be distinguished from the packing density effects (See Fig. 5.5).

5.3. Weighted Contact Loops

Loop structures, as described above, are purely topological constructs; they are defined solely by their number of comprising edges. However, loops with an identical number of edges do not necessarily have identical stability: the magnitude and arrangement of contact forces factor heavily into whether a particular loop will be able to withstand

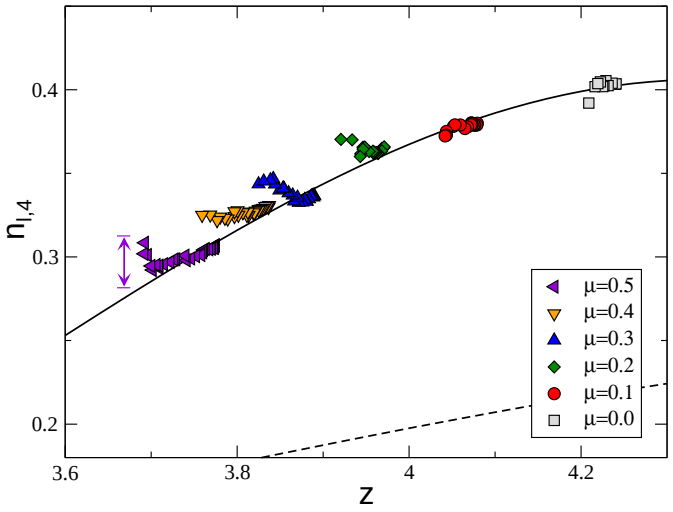

Figure 5.5. **Fourth-order loop fraction and coordination number.** From the randomly wired lattice model, we expect $n_{l,4} = 3(Z/6)^4(1 - Z/6)$ (dashed curve). In this case loop fractions in the untilted beds are described by a fit of the form $\alpha(Z - \beta)^\gamma(1 - Z/6)^\eta$(solid line). For beds with $\mu > 0.1$, $n_{l,4}(Z)$ tends a deviation from the calculated fit grows as θ_g approaches the marginal angle of stability, indicating that tilting effects on $n_{l,4}$ are unique.(Contrast with Fig. 5.4

perturbation. Below, we show that relative loop stability can be quantified with a weighting function, ξ. We then use ξ to revisit the problem of the tilted bed, constructing a more complete relationship between tilting and destabilization and identifying additional unique effects of tilting on network structure.

5.3.1. From Qualitative to Quantitative: Giving Stability a Number

For any contact loop there is a finite range of compatible loads, which corresponds to the allowable set of contact loop forces. Consider a third-order loop, where the contact forces, f_{12}, f_{23} and f_{13}, define the resulting compressive force vectors f_a, f_b, and f_c (See Fig. 5.6). The most stable arrangement of contact forces is $f_{12} = f_{23} = f_{13}$, such that

each of the resulting compressive force vectors lies in the center of its stable range, and small perturbations in either directions are unlikely to compromise the loop. On the other hand, consider the arrangement $f_{12} << f_{23} \approx f_{13}$, for which the compressive force vectors lie near the edge of the stable region (See Fig. 5.6). A slight perturbation is likely to move the loop into an unstable region. This loop property is captured with the weighting function, ξ:

$$\xi_{i,j,k} = \left(\frac{f_{ij}}{\overline{f}}\right)\left(\frac{f_{jk}}{\overline{f}}\right)\left(\frac{f_{ik}}{\overline{f}}\right) \tag{5.9}$$

$$\overline{f} = \frac{1}{3}\left(f_{ij} + f_{jk} + f_{ik}\right) \tag{5.10}$$

where i, j and k are neighboring particles that form a loop. $\xi_{i,j,k} = 1$ for a loop with equally weighted edges (the most stable force arrangement) and approaches zero as the relative weight of any edge in a loop goes to zero. ξ can be mapped onto a three dimensional phase space, where each dimension corresponds a contact force, and the stable region can be represented by an equilateral triangle. $\xi = 1$ lies at the center of the triangle and $\xi = 0$ lies at the perimeter, such that the inner region of the triangle corresponds to greater stability and the outer regions corresponds to increased fragility. We validate ξ as a stability indicator by mapping trajectories of ξ for individual loops in a gradually tilted bed.

Recall that the granular bed is tilted in intervals (1 second tilting interval followed by a 1 second rest interval). We label the granular network prior to each tilting interval as a stage, n, such that $n = 1$ corresponds to $\theta_g = 0$, $n = 2$ corresponds to $\theta_g = 0.1$, and

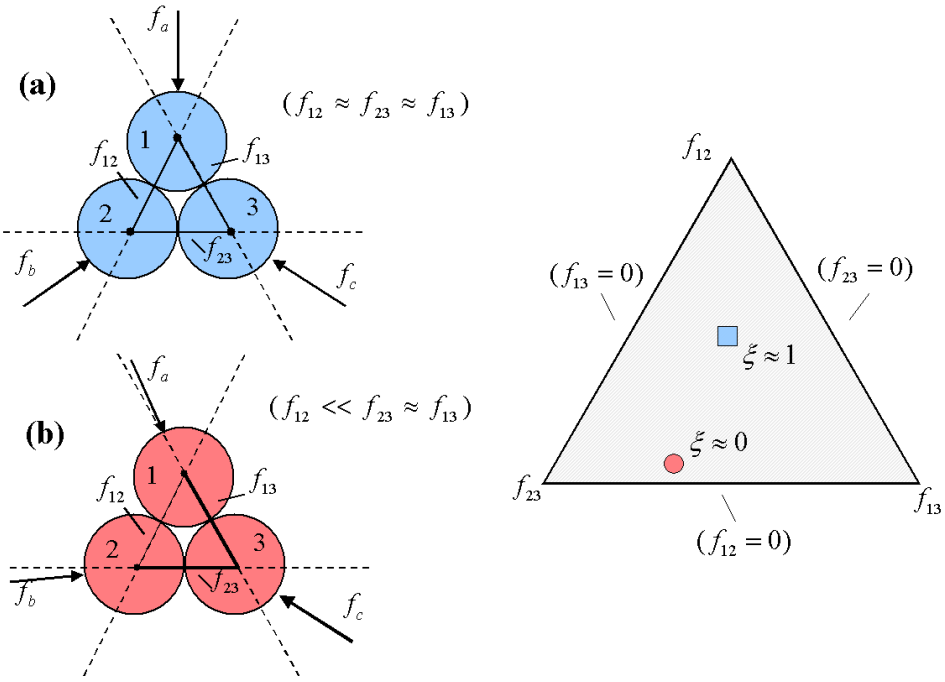

Figure 5.6. **Mapping of loop structures.** The stability of a loop can be represented as a function, $\xi(f_{12}, f_{23}, f_{13})$, of the contact forces which make it up. (a) Loops with $\xi \approx 1$ (i.e. $f_{12} \approx f_{23} \approx f_{13}$) are very stable and lie near the center of the stable region (represented as a square on the triangular map, at right). (b) Loops with $\xi \approx 0$ (i.e. $f_{12} << f_{23} \approx f_{13}$) are marginally stable and lie near the perimeter of the stable region (represented as a circle on the triangular map).

so on. This description affords a convenient distinction between stable and marginally stable triples: we say that a triple that exists during stage n is stable if, and only if, it also exists during stage $n+1$. Alternatively, we say that a triple that exists during stage n, but not stage $n+1$ is marginally stable.

A comparison of ξ values for stable and marginally stable triples suggests that ξ is indeed an indicator of stability. In frictional systems, the mean value of ξ drops from 0.58 for triples classified as stable (ξ^{stable}) to 0.30 for triples classified as unstable ($\xi^{marginal}$),

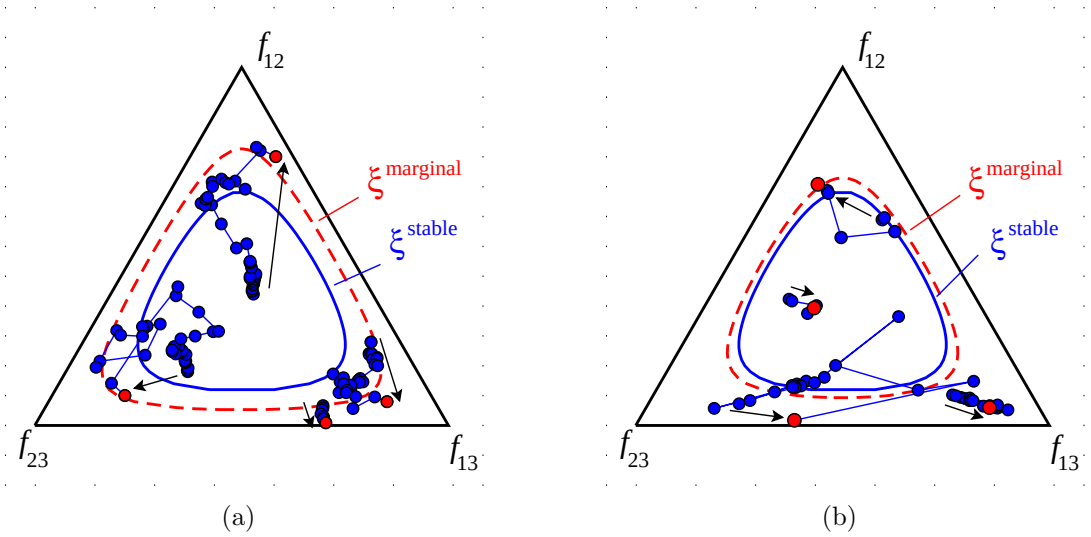

Figure 5.7. **Stability trajectories of individual loops**. Trajectories of third-order loops are mapped in the f_{12}, f_{23}, f_{13} triangular phase space for (a) a bed of rough particles ($\mu = 0.5$) and (b) a bed of smooth particles ($\mu = 0$). (Arrows indicate the net trajectory over the life span of the loop.) The overall tendency is for loops to migrate from the center of the triangle towards the perimeter. Each blue circle represents a stable stage in the loop trajectory, with a red circle indicating the final, marginally stable stage (after which the loop becomes unstable and fails). In systems of rough particles, ξ^{stable} is 0.58 (denoted by the solid blue isostability curve) and $\xi^{marginal}$ is 0.30 (denoted by the dashed red isostability curve). In systems of perfectly smooth particles, ξ^{stable} is 0.59 and $\xi^{marginal}$ is 0.41.

indicating that marginally stable triples tend to lie near the perimeter and stable triples towards the center of the stable triangle. (On the other hand, $\xi^{stable} \approx \xi^{marginal}$ would suggest that ξ is a poor indicator of stability.) In systems with perfectly smooth particles, the difference is less pronounced – $\xi^{stable} = 0.59$ and $\xi^{marginal} = 0.41$. We can visualize these results by plotting ξ^{stable} and $\xi^{marginal}$ as isostability curves on the stable triangle. The multi-stage trajectories of individual triples include several, seemingly random leaps, but have an overall tendency to migrate towards the outer region of the stable space (See Fig. 5.7).

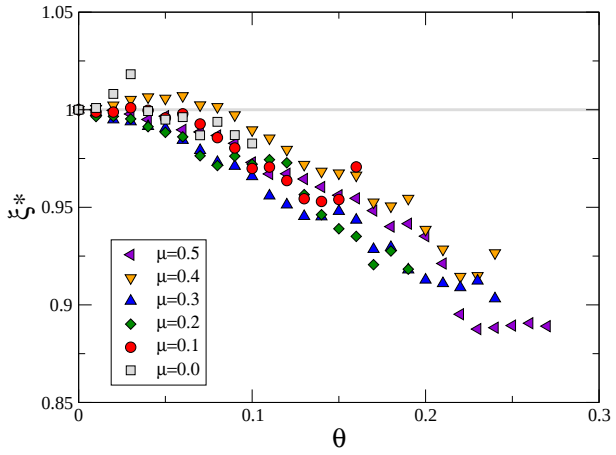

Figure 5.8. **Loop stability as a function of tilting.** The normalized mean loop stability (ξ^*) tends to decrease as the tilting angle (θ_g) is increased.

5.3.2. Effects of Tilting, Revisited

We previously showed that small loops in a granular packing tend to decrease in number as the bed is tilted; they also decrease in stability. The normalized mean stability of third-order loops,

$$\xi^*_{l,3} = \frac{\overline{\xi}_{l,3}}{\overline{\xi}^o_{l,3}} \tag{5.11}$$

can decrease by as much as 15% over the static tilting range (See Fig. 5.8). The mean stability of fourth-order loops, $\xi^*_{l,4}$ behaves similarly. These are unique effects of tilting: mean loop stability in an untilted bed, $\overline{\xi}^o_{l,3}$, is roughly independent of packing density, indicating that the tilting effect on loop stability can be isolated from density effects (See Fig. 5.9).

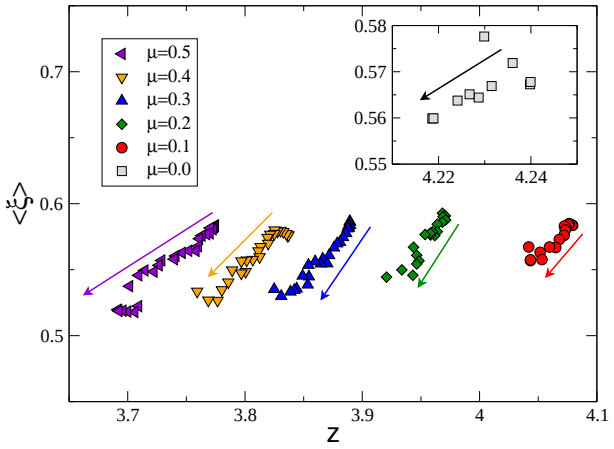

Figure 5.9. **Loop stability and coordination number.** A decrease in loop stability can be isolated as a tilting effect. ξ is roughly independent of packing density, but decreases with increasing tilting angle, suggesting that ξ varies independently of Z, and the observed decrease in ξ as a function of tilting is unique (contrast with Fig. 5.3). Arrows indicate the direction of increasing tilting angle.

5.4. Discussion

Questions regarding stability and fragility of granular packings have garnered much recent attention. Many studies use continuum-scale concepts (such as fabric tensor [**67**]) while others target statistics of single contacts. But perhaps the continuum scale is too large, and the single contact scale too small, for a suitable mechanical description of stability – it may be argued that granular stability and fragility arise from structures on the order of a few particles. In two-dimensions, these structures are contact loops. A contact loop analysis yields valuable insights: loop structure in a granular packing is strongly dependent on friction coefficient; granular packings (particularly frictional packings) are especially rich in fourth order loops, compared to a random lattice model; and tilting has unique, destabilizing effects on loop structure.

Other important questions may be addressed in future studies. For example, we have shown that third-order loops tend to migrate from the center of the stable triangular region to the perimeter, and then fail. But where on the perimeter do they most often exit? Near a vertex (i.e., $f_{12} \approx f_{23} << f_{13}$), or a midpoint (i.e., $f_{12} << f_{23} \approx f_{13}$)? Such information would be important for understanding failure mechanics. Also, we know that single forces in a granular packing exhibit spatial organization; are loop structures spatially organized as well? Do they destabilize (i.e., $\xi \rightarrow 0$) in clusters, chains, or randomly? Answers to these types of questions – along with possible extensions to three dimensions – may represent a significant step towards a first-principles understanding of stability and fragility in granular packings.

CHAPTER 6

Case Study III. Effects of Self-Organization on Transport

'...self-organization in the granular network promotes efficient transport...this can be understood within the framework of network theory'

Transport in heterogeneous media is a phenomenon of broad scope and ubiquitous importance – propagation of acoustic waves in sand [**50**, **51**], electrical conductivity of nanocomposite materials [**68**], and liquid flows in porous media are just a few examples relevant to physics [**69**], engineering, and material science. Of these heterogeneous media, granular matter, which exhibits both heterogeneity *and* self-organization, is unique.

In this chapter, we investigate – via numerical experiments – relationships between heterogeneity, self-organization and transport. Specifically, we consider heat transfer – a phenomenon relevant to industrial applications such as sintering and powder metallurgy, among others. We find that self-organization in the granular network promotes efficient transport and that, to a large extent, this relationship can be understood within the framework of network theory. Concepts such as *distance*, *efficiency*, and *betweenness centrality* are revealing. A simulated network attack experiment further demonstrates the utility of network theory as a predictive tool.

This chapter is based on published work by Smart *et al.* [**70**].

6.1. Methodology

We simulate two-dimensional systems of rough disks using Particle Dynamics – normal contact forces are calculated using the linear-spring dashpot model, and tangential forces are calculated using a damped variation of the Cundall and Strack model. The distribution of particle diameters is poly-disperse (normally distributed about the mean, $\overline{d}$, with 5% variance to reduce crystallization) and all particles have a friction coefficient $\mu = 0.5$. The granular system is bounded in the vertical direction by infinitely rough walls – where we impose a no-slip condition – and in the horizontal direction by a periodic boundary.

Granular packings are prepared via a three-stage simulation. In the *initiation* stage, $N = 2500$ point particles, with diameters equal to zero, are placed at random inside a box of prescribed width (L_x) and height (L_y). Next, in the *growth* stage, particles grow to their pre-specified sizes. In this stage, growing particles can collide, transferring small amounts of kinetic energy through dissipative collisions. In the *compression* stage, force is applied to the vertical walls, compressing the granular system to a specified vertical pressure, P_y, and yielding a static, nearly isotropic granular packing. (Although the horizontal pressure, P_x, is not explicitly controllable, it tends to be nearly the same as the vertical pressure.) The resultant packing fractions, $\phi = (L_x L_y)^{-1} \sum_{i=1}^{N} \pi(d_i/2)^2$, range from 0.803 to 0.807. The final system dimensions approximate a square, with lengths $L_x = 50\overline{d}$ and $L_y \approx 49\overline{d}$. See fig.6.1, top.

The granular packings can be viewed as networks: each particle is represented as a node, with two nodes connected by an edge if the corresponding particles are in contact. Specifically, we consider the weighted network, or force network, in which edges

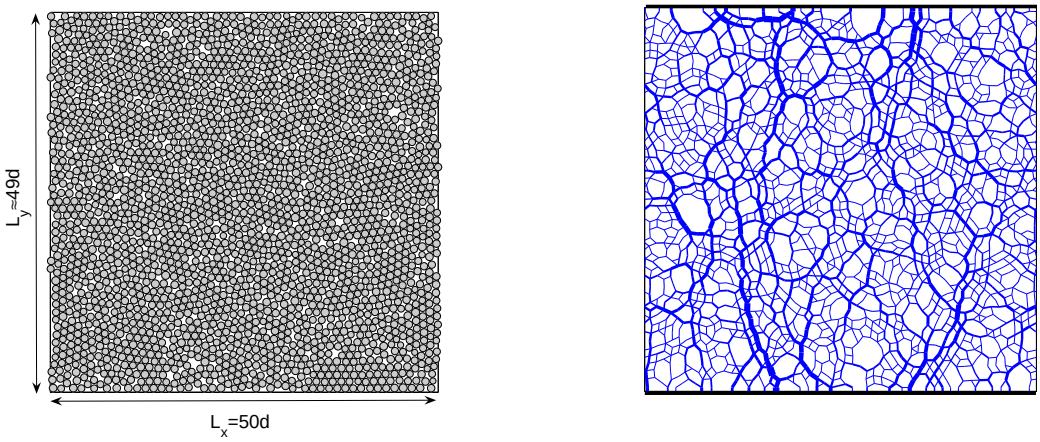

Figure 6.1. **The granular packing as a network.** (top) A system of rough disks is compressed between two walls (the horizontal boundaries are periodic). (bottom) The granular packing can be represented as a force network where nodes (representing particles) are connected by edges if the particles are contacting. Edge weight (line width) is proportional to the normal force along the corresponding contact.

are weighted according to the magnitude of normal force, f, along their corresponding contacts. See fig.6.1, bottom.

6.1.1. Heat Transfer Model

The local heat transfer coefficient, H_{ij}, between two contacting particles i and j is directly related to the area of their contact interface and, consequently, the magnitude of compressive force, f_{ij}. Specifically,

$$H_{ij} = A f_{ij}^{\eta} \tag{6.1}$$

where A is a collective term that includes particle diameter, the thermal conductivity of the solid material, and the effective Young modulus, each of which can be assumed

constant for a system of nearly uniform particles. Previously determined values of η range from 1/3 (analytical result for perfectly smooth, Hertzian spheres [**71**]) to 1.4 (analytical result incorporating surface roughness [**72**]) to 2.4 (experimental result for rough, spherical particles). In the current study we consider values of η over the range 0 to 3.

Two assumptions simplify the heat transfer calculations. First, we assume that the Biot number for granular particles is small, i.e., inter-particle resistance to heat transfer is large compared to intra-particle resistance, such that temperature distribution within a particle is homogeneous. This assumption is generally valid if the inter-particle contact radius is much smaller than the characteristic particle radius, as is typically the case for packings of hard, round granular particles (in our simulations, the ratio of contact radius to particle radius is on the order of 10^{-3}). Secondly, we assume that the interstitial space between particles is perfectly insulating (which approximates the behavior of a gas-solid particulate system), such that heat transfer occurs exclusively along inter-particle contacts. Interfacial heat fluxes across each inter-particle contact are then given by

$$Q_{ij} = H_{ij}(T_j - T_i) \tag{6.2}$$

where Q_{ij} is the flux from particle j to i; and the temperature evolution of particle i is found by integrating its energy balance over small time steps Δt:

$$\frac{\Delta T_i}{\Delta t} = \frac{1}{m_i c_i} \sum_j Q_{ij} \tag{6.3}$$

where interparticle fluxes, Q_{ij}, are summed over neighboring particles j, and m_i and c_i are the particle mass and heat capacity, respectively (the computational procedure is based on the method used by Vargas and McCarthy [**73**]).

6.2. Heterogeneity, Self-organization and Granular Heat Transfer

The heat transfer network (which has edges weighted by their heat transfer coefficient, H_{ij}) is related to, but not necessarily the same as the force network (which has edges weighted by f_{ij}). Recall the relationship between H_{ij} and f_{ij}:

$$H_{ij} = A f_{ij}^{\eta}. \tag{6.4}$$

When $\eta = 1$ the two networks are, for all practical purposes, identical. But changes in η affect the structure of the heat transfer network. Most importantly heterogeneity in the heat transfer network increases dramatically with η – the distribution of heat transfer coefficients, $p(H)$, shifts from exponential to power-law decay, as η increases from 1 to 3. For $\eta = 3$, some contacts may have H_{ij} as large as 10^2 times the mean (see Fig. 6.2). We show below that effects of heterogeneity, along with effects of self-organization, greatly impact the transport properties of a granular medium.

We isolate the influences of heterogeneity and self-organization on granular heat transfer in the following way. For each granular network we create (1) an equivalent uniformly weighted network (which exhibits neither heterogeneity nor organization of contact forces) and (2) a randomly rewired network (which exhibits heterogeneity, but not organization of contact forces). For any given granular packing, all three networks – the self-organized granular network (SO), the uniformly weighted network (UW), and the randomly rewired

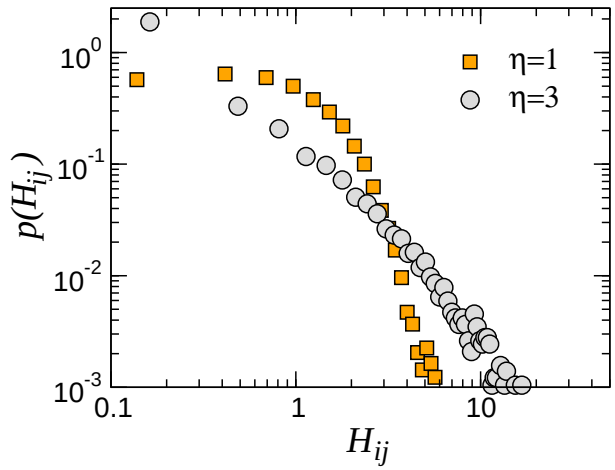

Figure 6.2. **Heterogeneity in the heat transfer network.** For $\eta = 1$, the heat transfer network is identical to the force network, and the probability distribution of single contact heat transfer coefficients, $p(H)$, decays exponentially at large H_{ij}. For $\eta = 3$, $p(H)$ decays as a power-law, and some contacts may have H_{ij} as large as 10^2 times the mean.

network (RR) – have identical topology. No edges are destroyed or formed in either modification; only their weights are changed. See fig.6.3. In the UW network all edge weights are set equal to the mean, and in the RR network edge weights are randomly reassigned, such that the sum over all edge weights in the network is unchanged from the original SO network. Two numerical heat transfer experiments – one transient, one steady state – reveal substantial differences between the transport properties of the real and modified networks, illustrating the effects of heterogeneity and self-organization.

6.2.1. Transient Heat Transfer: Calculating Thermal Diffusivity

In the first experiment, we calculate thermal diffusivity, α, by measuring the propagation speed of a traveling heat front. We define the initial temperature of the system (walls and

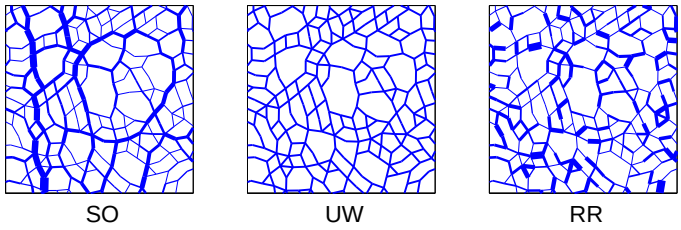

Figure 6.3. **Modifying the granular force network.** The granular force network (SO) exhibits self-organization of edge weights (contact forces, f). In the uniformly weighted network (UW) all weights are set equal to the mean, $\overline{f}$. In the randomly rewired network (RR), edge weights from the SO network have been randomly reassigned. All three networks have identical topology.

particles) to be zero. Then, at time $t = 0$, we impose a step change in the temperature at the bottom wall ($T_{y=0} = 1$). A threshold temperature (we choose $T^* = 0.01$) defines a heat front, which propagates in the positive y direction as heat flows from the hot to the cold wall. See fig.6.4. At small t, the system approximates transient conduction in an infinite slab, such that thermal diffusivity can be estimated by plotting the average position of the heat front – or penetration depth, δ – versus $t^{1/2}$ [**74**]. Specifically, for $T^* = 0.01$,

$$\delta(t) = 3.12\alpha^{1/2}t^{1/2} \tag{6.5}$$

A comparison of the SO, UW and RR networks is revealing – the calculated thermal diffusivity of the self-organized network is markedly higher than that of the uniformly weighted and randomly rewired networks. Specifically, α^{SO}/α^{UW} is a monotonically increasing, power-law function of the exponent η (recall that η relates the inter-particle heat

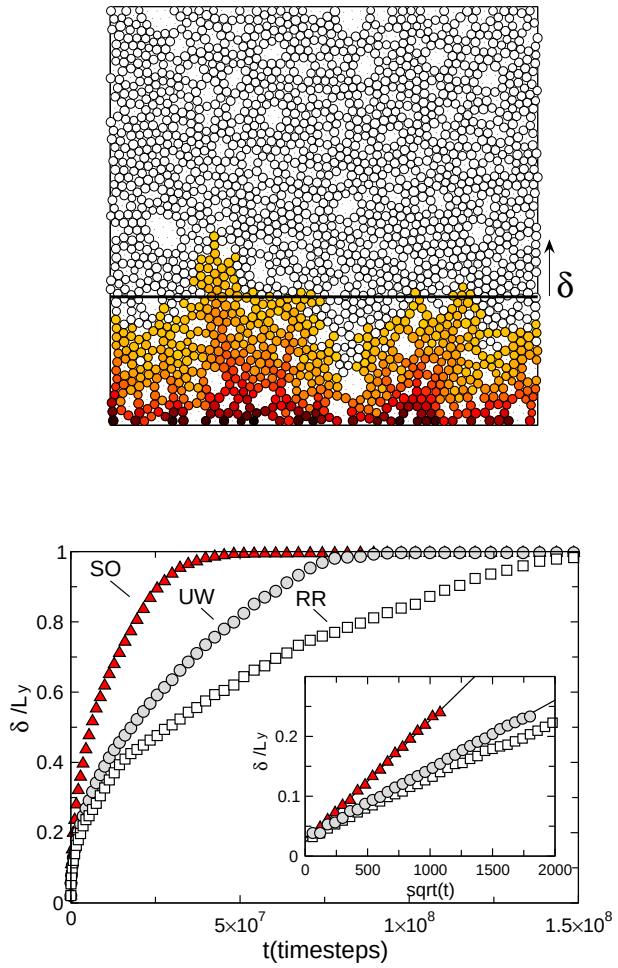

(b)

Figure 6.4. **Transient calculation of the thermal diffusivities of self-organized, uniformly weighted, and randomly rewired networks.** (a) At $t = 0$, a step change in the temperature of the bottom wall is induced (from $T_{y=0} = 0$ to $T_{y=0} = 1$), resulting in a vertically propagating heat front. Shaded particles correspond to those with a temperature greater than the threshold, $T^* = 0.01$, and the solid line corresponds to the penetration depth, δ, of the heat front. (b) At small t, penetration depth increases as $t^{1/2}$, such that a plot of δ vs. $t^{1/2}$ yields a line with slope $3.12\alpha^{1/2}$ (inset). In general, thermal diffusivity of the self-organized (SO) network is significantly greater than that of the uniformly weighted (UW) and randomly rewired (RR) counterparts. All data shown are generated with $\eta = 2$.

transfer coefficient to contact force):

$$\alpha^{SO}/\alpha^{UW} = 1 + \beta\eta^{\gamma} \tag{6.6}$$

with $\beta = 0.39$ and $\gamma = 2.31$, such that α^{SO}/α^{UW} is greater than one for all $\eta > 0$. See fig.6.5. The disparity between the self-organized and uniformly weighted networks is not explained by heterogeneity of inter-particle forces. The randomly rewired network – which, compared to the self-organized network, has an identically heterogeneous force (edge weight) distribution – is a relatively poor heat transfer medium, defined by a ratio α^{RR}/α^{UW} that is less than one for all $\eta > 0$. See fig.6.5.

6.2.2. Steady State Heat Transfer: Effective Conductivity

In the second experiment, we measure the effective conductivity of the *SO*, *UW*, and *RR* networks by allowing each system to evolve to a steady, equilibrium temperature profile. Then, consistent with Fourier's Law, the equilibrium flux across any line of constant y is directly proportional to the effective conductivity, k:

$$q_y|_{y=c} = \frac{k}{L_y}\left(T_{y=0} - T_{y=L_y}\right), 0 \leq c \leq L_y \tag{6.7}$$

Qualitatively, the results closely parallel those of the transient experiment – the self-organized network exhibits significantly higher conductivity than the uniformly weighted network, with k^{SO}/k^{UW} similarly approximated by a monotonically increasing power-law function of η. Again, the difference is not adequately explained by the heterogeneity of inter-particle forces, as the randomly rewired network has relatively low effective conductivity, defined by a ratio k^{RR}/k^{UW} that is less than one for all $\eta > 0$. See Fig. 6.5

In theory, the transient and steady-state methods are equivalent approaches towards calculating the conductivity of a regular material – by definition, $\alpha \equiv k/(\rho C_p)$, where ρC_p is the thermal capacity. Indeed, this appears to hold true for the UW networks, for which the steady-state-calculated conductivity, k^{UW}, and the transient-calculated conductivity, $k_{tr}^{UW} = \rho C_p \alpha^{UW}$, are close. That is, the normalized difference,

$$\epsilon^{UW} = \frac{\left(k_{tr}^{UW} - k^{UW}\right)}{k^{UW}} \tag{6.8}$$

is small ($\left\langle \epsilon^{UW} \right\rangle$, averaged over all η, is -0.06 ± 0.01, where the error interval represents a standard deviation), indicating that the transient method tends to slightly, yet consistently, underestimate the effective conductivity of the UW networks. This is likely an effect of finite system size. On the other hand, the differences ϵ^{RR} and ϵ^{SO} – defined as for the UW network – can be large ($\left\langle (\epsilon^{RR} \right\rangle = 0.11 \pm 0.16$, $\left\langle \epsilon^{SO} \right\rangle = 0.51 \pm 0.50$) and increase as a function of η (for $\eta = 3$, ϵ^{RR} and ϵ^{SO} are 0.32 and 1.27, respectively), indicating a tendency for the transient method to overestimate effective conductivity as heterogeneity increases. Such anomalous behavior is known to potentially occur in heterogeneous, disordered media [**75**].

6.2.3. A Networks Vantage Point: Distance and Efficiency.

The above results indicate that heterogeneity and self-organization of forces promote efficient heat transfer in granular media. This is not altogether surprising – for $\eta = 1$, it can be shown that the condition that gives rise to self-organization (i.e., balanced compressive force at each particle) is also the condition that optimizes conductivity [**76**]. However, the set of networks that lie away from this optimum (a set that includes the

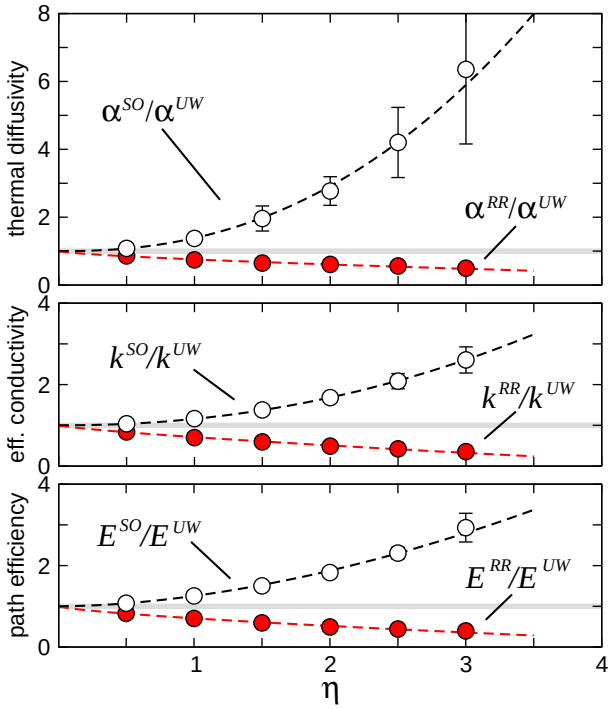

Figure 6.5. **Alternative measures of conductive efficiency in a granular packing.** Heat transfer properties of the self-organized network (empty circles) and the randomly rewired network (filled circles) are normalized with respect to the uniformly weighted network and plotted as a function of η. All curves are well approximated by a power-law fit, $f(\eta) = 1 + \beta\eta^{\gamma}$ (dashed lines), with two important implications: (1) Self-organization tends to promote efficient transport – the ratios α^{SO}/α^{UW} and k^{SO}/k^{UW} are greater than one for all $\eta > 0$; and (2) the network metric, path efficiency, quantitatively describes the relative conductivities of *SO*, *UW*, and *RR* networks. The fit parameters (β, γ) are: 0.39,2.31 $(\alpha^{SO}/\alpha^{UW})$; 0.16, 2.11 (k^{SO}/k^{UW}); 0.26, 1.78 (E^{SO}/E^{UW}); -0.24, 0.69 $(\alpha^{RR}/\alpha^{UW})$; -0.29, 0.77 (k^{RR}/k^{UW}); -0.29, 0.71 (E^{RR}/E^{UW}).

UW and *RR* networks, as well as the *SO* networks with $\eta \neq 1$) is not well understood. It is here that concepts of network theory are particularly useful, providing a quantitative means towards understanding the relationship between heterogeneity, self-organization, and transport efficiency. Particularly, we consider the concept of network distance.

In an un-weighted network, the *distance* between two nodes is defined as the minimum number of edges required to connect them along the network. By defining a length, l_{ij}, for each edge in the network, distance can be adapted to describe the connectivity of weighted networks – it is equal to the smallest sum of edge lengths from the set of all possible connecting paths between two nodes [**54**]. We are careful to distinguish between network distance measures (e.g. edge length) and the more familiar, physical measures of distance (e.g. Euclidean distance) – edge length, and therefore network distance, needs not correspond to physical proximity of node pairs. As we are concerned primarily with heat transfer, it is advantageous to define the edge length, l_{ij}, as the inverse of the local heat transfer coefficient, H_{ij}, such that the distance along an inter-particle contact is proportional to its resistance to heat transfer.

Path efficiency, defined as the inverse of the distance between node pairs, provides a quantitative measure of node to node conductivity; efficient paths have low resistance to heat transfer [**77**]. Indeed, a path efficiency analysis of the *SO*, *UW*, and *RR* networks yields remarkable results – similar to the thermal diffusivity and effective conductivity, the average path efficiency, E, of node-to-wall paths in the *SO* network is greater than that of the *UW* and *RR* networks. (Path distances are calculated using the Djikstra algorithm [**78**].) In fact, the network calculated efficiency ratios, E^{SO}/E^{UW} and E^{RR}/E^{UW}, are virtually identical functions of η as the measured effective conductivity ratios, k^{SO}/k^{UW} and k^{RR}/k^{UW}. See fig.6.5.

Increased efficiency, as a result of self-organization, is a pervasive theme in network theory. In several naturally occurring networks, known as *small-world* networks, long-range connections cause the average distance between node pairs to remain surprisingly

small even as the systems become very large [**79**]. Although granular networks are not small-world, the presence of spatially correlated, inter-connecting force chains plays a role similar to long-range connections, providing highly conductive conduits that effectively decrease the size of the transport network. This point is further illustrated in the following network attack experiment.

6.3. Network Responses to Attack

In terms of heat transfer, the effect of removing edges from the granular network is clearly deleterious – network conductivity diminishes with each additional edge removed. But an intriguing question arises: Which edge removal strategy yields the most rapid decrease in effective conductivity? We consider three such strategies: one random, one based on local heat transfer properties, and one – formulated within the networks framework – that incorporates both local properties and large-scale organization.

Random Removal. Random edge removal, or failure, serves as a benchmark – we remove edges at random and calculate the resulting change in the effective conductivity of the network.

Targeted Removal (Local Heat Transfer Coefficient). A naive hypothesis is that contacts with largest heat transfer coefficient, H, are most important for heat transfer. The second removal strategy – removing edges in decreasing order of H – is a test of this hypothesis. Since heat flow is in the vertical direction, we remove edges according to their vertical component, H^y. We find that the alternative - removing edges solely according to the scalar magnitude H - is less effective (data not shown).

Targeted Removal (Betweenness Centrality). Generally, many of the shortest paths between nodes in a network may pass through one or more common edges. Such an edge is said to have high *betweenness centrality*, B, where B_{ij} of an edge connecting nodes i and j is defined as the number of shortest paths in which it is included, divided by the total number of shortest paths. B is a particularly useful quantity in that it incorporates both local heat transfer properties and large-scale organization. Thus, as the third strategy, we remove edges according to their betweenness. The procedure is iterative – the single edge with largest B is removed, B values are then recalculated, and the process is repeated.

(We note that an edge removal, in the current context, affects only the transport properties of the network. That is, we do not consider the resultant disturbance to the mechanical equilibrium of the packing, such that a removal can be thought of, precisely, as replacing a conducting edge with a perfectly insulating edge that supports an equivalent mechanical load.)

We find that effective conductivity decreases most rapidly when edges are targeted according to betweenness (the least effective strategy is random failure). See fig.6.6. The inferable corollary is significant as well – the important contacts for heat transfer in a granular network are those with high betweenness. The role of high betweenness edges and nodes in complex networks is relatively well understood – they tend to act as connectors, controlling information flows and linking otherwise isolated clusters in various networks. High betweenness edges in the granular network appear to perform similar functions.

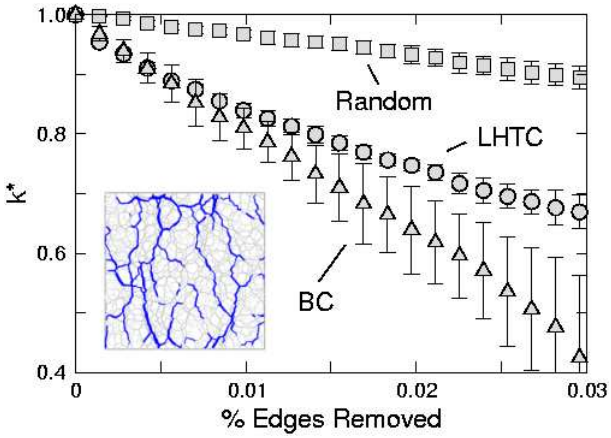

Figure 6.6. **Network responses to random and strategic attack.** In a network attack experiment, three node-removal strategies are employed: random removal, removal according to local heat transfer coefficient ($LHTC$) and removal according to betweenness centrality (BC). The normalized conductivity, $k^* = k/k^0$, decreases fastest when edges are removed according to the BC strategy (the least effective strategy is random removal). (inset) A threshold analysis reveals paths of high betweenness centrality, i.e. paths of low resistance in a granular network (edges with $B > 2.5\overline{B}$ are darkened)

6.4. Discussion

Granular heat transfer serves as a prototype for transport in heterogeneous, complex-structured media, revealing that (1) self-organization substantially impacts the transfer properties of a medium, and (2) this influence can be largely understood within the networks framework.

The impact of self-organization on conductivity is remarkable in its magnitude – under realistic heat transfer conditions, the conductivity or thermal diffusivity of a self-organized network (in this case, the granular contact network) may be several times larger than that of a comparable uniformly weighted network. Perhaps more surprising, however, are the

quantitative insights provided by network measures. Network distance (or more specifically, it's inverse – path efficiency) reproduces, typically within about a single standard deviation, the numerically calculated relationship between conductivities of the granular networks and their modified counterparts (uniformly weighted and randomly rewired networks). Another network measure, betweenness centrality, is shown to be useful for identifying the important contacts for heat transfer.

That network theory – with suitable adaptations – translates well to granular matter is broadly significant: its implications likely extend to other force-dependent granular transport phenomena (such as electrical conductivity and acoustic wave propagation), as well as other heterogeneous transport media (such as composite materials and porous media). These various transport systems, unified by a common need to understand relationships between structural, dynamical and equilibrium properties, constitute an ideal testing ground for applications of novel concepts in network theory.

CHAPTER 7

Introduction to Part II

Cells are among the most complex of the complex systems studied in science. As genomes are uncovered, the extent of cellular complexity comes into clear focus: a single cell can consist of tens of thousands of components – genes, proteins, enzymes, and other metabolites – existing in a delicate, interactive, and dynamic balance. The library of data, when approached via traditional methods of biology, is overwhelming. However, network theory provides an efficient statistical mechanical framework for extracting information at the genome, protein, and metabolism level [**13**]. In Part II of the dissertation, we use network analysis techniques to investigate metabolism-level cell behavior.

7.1. Constructing Metabolic Networks

The cell metabolism is a set of interacting bio-chemical reactions that converts nutrients into products (energy, cellular components, and waste products). This system can be thought of as a network of metabolites (each substrate or product of an intracellular reaction is a *metabolite*) and reactions. Below, we review the several ways to represent such a system as a network.

One method is to represent each metabolite as a node, where two nodes are connected by an edge if the metabolites participate in the same reaction (see Fig. 7.1a). This representation, which we call the *metabolite reconstruction*, yields networks with striking characteristics, most notably *scale-free* and *small world* properties [**80**–**82**]. That is,

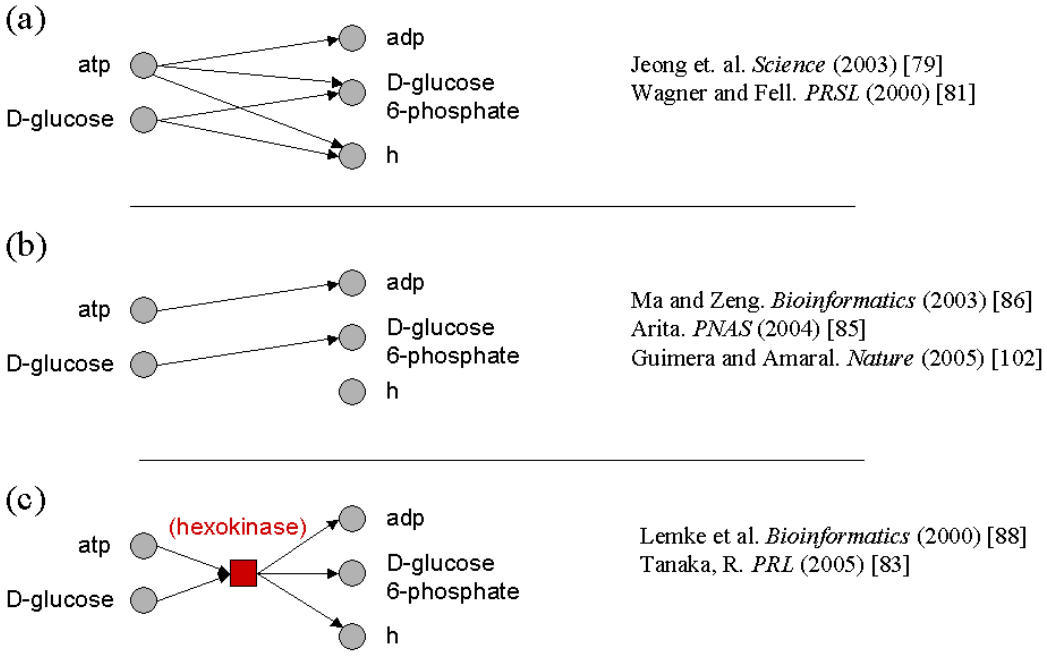

Figure 7.1. **Constructing metabolic networks** (a) Metabolite reconstruction of the glycolysis reaction, atp + D-glucose → adp + D-glucose6-phosphate + h. Directed edges connect the participating metabolite nodes. (b) Modified Metabolite reconstruction, where only the structurally related metabolite pairs are connected by edges. (c) Bi-partite graph, with both metabolite (circle) and reaction nodes (square). We adopt the Bi-partite graph representation for our study on metabolic robustness.

node degree distributions in metabolite reconstructions (the node degree, k, is equal to the number of edges connected to a node) obeys power-law scaling, and the average number of edges required to connect any two nodes on the network remains small (≈ 3) even when the system is large ($\approx 10^3$ nodes) [**80**]. In short, the structure of metabolite reconstructions is similar to other naturally occurring networks such as air-transport networks, social networks, and the internet, among others [**14**, **83**].

The results, however, are potentially misleading. On one hand, it can be argued that the node degree distribution in metabolic networks is best viewed not as a power-law, but as the superposition of a few exponentially-decaying sub-components [**84**]. On the other hand, and perhaps more importantly, it is unclear whether the metabolite network representation conveys useful information regarding bio-synthesis [**85**]. Shortest paths in the metabolite network tend to pass through highly connected *currency* metabolites (such as ATP, NADP, H_2O, etc.) and, although they may indicate regulatory properties, they do not necessarily correspond to valid biosynthetic pathways.

An alternative network representation incorporates an additional criterion – metabolite nodes are connected with an edge if they (1) participate in the same reaction *and* (2) are structurally related (See Fig. 7.1b). In this way, currency metabolites neither inflate the node degree distribution nor deflate the mean shortest path. By this and related reconstruction methods, it can be argued that metabolic networks are *not* small world [**86**, **87**]. However, a problem remains – paths in the modified metabolite representation do not necessarily indicate valid biosynthetic pathways.

A third representation is the *bi-partite graph*, which has also been called the *s-graph* representation [**88**, **89**] (Fig. 7.1c). The bi-partite graph consist of two types of nodes, metabolite nodes and reaction nodes, with a metabolite node connected to a reaction node if it participates as either a substrate or product. The bi-partite representation retains the important biochemistry of the network and is well suited for flux balance analysis and robustness studies. We adopt the bi-partite representation for Part II of the dissertation.

7.2. Cellular Robustness

The literature regarding robustness of metabolic networks is considerable. In particular, Flux Balance Analysis (FBA) and related numerical methods have been used – with remarkable success – to predict the effects of enzyme, reaction, and metabolite deletion [**90**–**92**]. However, the levels of detail and specificity associated with these methods make it difficult to extract generic trends. They identify *what* happens when a network node is affected, but not *why*. Recently, studies have begun to try to answer the 'why' – i.e., explain how network structure affects robustness [**85**, **93**]. In the following chapter, we apply an algorithm that is based on the principles of FBA, but that also offers the necessary flexibility to investigate generic relationships between network structure and robustness.

We consider the metabolic networks of four species (Fig. 7.2, Table 7.1):

(1) *Escherichia coli* (761 metabolites, 931 reactions), a potentially dangerous bacterium which can cause food poisoning in humans;

(2) *Saccharomyces cerevisiae* (1061, 1149), a yeast belonging to the kingdom *Fungi* and commonly used to produce ethanol via fermentation;

(3) *Staphylococcus aureus* (606, 645), a pathogenic bacterium widely known for its methicillin-resistant strain, MRSA, which is a leading cause of hospital infection;

(4) *Methanosarcina barkeri*(558, 619), an anaerobic archaea that can be found in the bovine intestinal tract, and is thought to be a major producer of atmospheric methane.

Notably, each of the above are single-cell organisms, and *S. cerevisiae* is the lone eukaryote (i.e., has a nuclear membrane) of the group. Each of the *in silico* reconstructions are

compiled and generously supplied by the Palsson group (University of California at San Diego) [**94**–**97**].

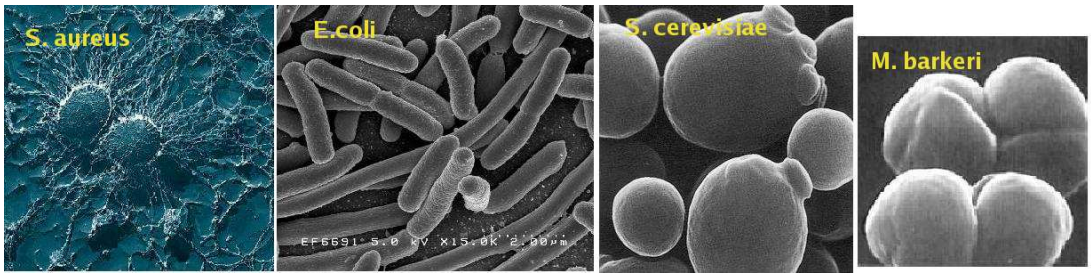

Figure 7.2. **Microorganisms used in our study.** The robustness of *E.coli*, *S. cerevisiae*, *M. barkeri*, and *S. aureus* metabolisms are investigated in Part II of the dissertation.

Organism	Reconstruction	Metabolites	Reactions
E. coli	iJR904	761	931
S. cerevisiae	iND750	1061	1149
S. aureus	iSB619	606	645
M. barkeri	msb4100046-s7	558	619

Table 7.1. **Metabolic reconstructions used in our study**. All reconstructions are provided by Palsson and others [**94**–**97**].

CHAPTER 8

Case Study IV. Cascading Failure in Metabolic Networks

'...aside from E. coli, the metabolic networks are exceptionally robust...(owing) primarily to the organization of non-rigid branches.'

The complexity of metabolic networks can be overwhelming – their architecture, despite being reconstructible at great levels of detail, remains poorly understood. Have cellular metabolisms naturally evolved to an optimal state? How does the metabolism respond to stress? Can it be altered to produce desired products? Such questions, addressing the relationship between metabolic form and function, are relevant to a broad scientific community, yet remain open [**85**]. In this chapter, we investigate the form-function relationship by looking at the influence of topology on robustness in metabolic networks.

It is well known that the removal of a single gene from a metabolic network - and consequently, its corresponding enzyme and reaction(s) - can have a cascading effect, resulting in the 'knockout' of several additional reactions and metabolites [**89**, **93**, **98**]. Such behavior is a common occurrence in complex networks - a single overloaded line in a power transmission network can lead to a blackout spanning millions of homes [**99**], a small nucleus of trendsetters can shift popular opinion [**100**], and congestion on a single router can lead to large-scale internet collapse. However, the mechanisms by which cascades

occur, and thus the network features that either induce or mitigate them, can differ significantly between systems. Metabolic networks are special, in that the mechanisms of metabolic robustness can seem counter to typical complex systems. For example, in typical scale free networks high degree nodes, or hubs, are most critical to network function – their removal quickly disables the network. But in metabolic networks the removal of low degree nodes may affect network function as much as, if not more, than those with high degree [**85**]. In this study, we use a topology-based algorithm, based on a Boolean interpretation of the flux balance criteria, to study cascading failure in *E. coli*, *S. cerevisiae*, *S. aureus*, and *M. barkeri* metabolic networks.

We find that, aside from *E. coli*, the metabolic networks are exceptionally robust – that is, they exhibit organizational motifs that reduce the likelihood of large failure cascades, as evidenced by comparison with randomly wired networks. We decompose the network into groups of *rigid clusters* and *non-rigid branches* (terms that we we will define below), and provide evidence that the enhanced robustness of metabolic networks owes primarily to the organization of non-rigid branches. We also show – by modeling random failure cascades as percolation on a Bethe Lattice – that the composition of the metabolic networks is *sub-critical* with respect to the formation of rigid clusters, and likely *super-critical* with regards to non-rigid branching.

8.1. Methodology and Failure Algorithm

We represent the cellular metabolism as a directed, bi-partite graph, with two types of nodes - one representing chemical reactions and the other representing metabolites. An edge connects a metabolite node to a reaction node if the metabolite participates in the

reaction as a reactant (in which case the edge is directed towards the reaction node) or product (in which case the edge is directed towards the metabolite node).

8.1.1. The Topological Flux Balance Criteria

Any metabolite, in order to persist in the metabolic network, must be able to maintain a steady, non-zero concentration (this is also the central argument of FBA [**90**]). It follows that, as a minimum requirement for flux balance, each metabolite must participate in at least one generating and one consuming reaction – the concentration of a metabolite that is consumed but not generated diminishes to zero, whereas the concentration of a metabolite that is generated but not consumed grows towards infinity. The topological equivalent is that each metabolite node must have at least one incoming and one outgoing edge. In terms of node degree, k, we say that a metabolite node, i, is viable if and only if $k_{in,i}, k_{out,i} \geq 1$.

Exceptions to the topological flux balance (TFB) criteria are (1) *external metabolite nodes*, which represent extracellular compounds such as nutrients and products; and (2) *dead-end metabolite nodes* which represent metabolites that, due to incomplete *in silico* reconstructions, appear to participate in either no generating or no consuming reactions. We treat external and dead-end metabolite nodes as infinite reservoirs; they are the only metabolite nodes allowed to exist in the network with either k_{in} or $k_{out} = 0$. (Transport - including diffusion - across cell membranes is considered a reaction, such that extra- and intra-cellular versions of the same metabolite are distinguished as separate nodes.)

In practice, metabolites may also be consumed or produced by non-metabolic processes, e.g. DNA replication. However, rates of non-metabolic consumption and production tend to be small, relative to typical steady state metabolic fluxes.

8.1.2. The Failure Algorithm

Prior to node deletions, all metabolite nodes (excluding external and dead-end nodes) meet the TFB criteria. However, the removal of a reaction node, along with its associated edges, may leave a neighboring metabolite node with either k_{in} or $k_{out} = 0$. Such a node is said to be *dead*, and is subsequently deleted from the network along with each reaction in which it participates (a reaction is viable – or can maintain a steady, non-zero flux – if and only if each of its reactants and products are viable). The result is an iterative algorithm by which the removal of a single reaction node can lead to large-scale cascading failure in the metabolic network:

(1) Initiate failure by deleting, or 'killing', a node and each of its connecting edges (both incoming and outgoing edges are removed)
(2) Delete any metabolite node for which k_{in} or $k_{out} = 0$, along with each of its remaining edges.
(3) Delete any reaction node that shares an edge with a dead metabolite, along with each of its remaining edges.

Steps 2 and 3 are iterated until all remaining reaction nodes and metabolite nodes meet the flux balance criterion (see Fig. 8.1). The algorithm is similar, in spirit, to that used in [**89**].

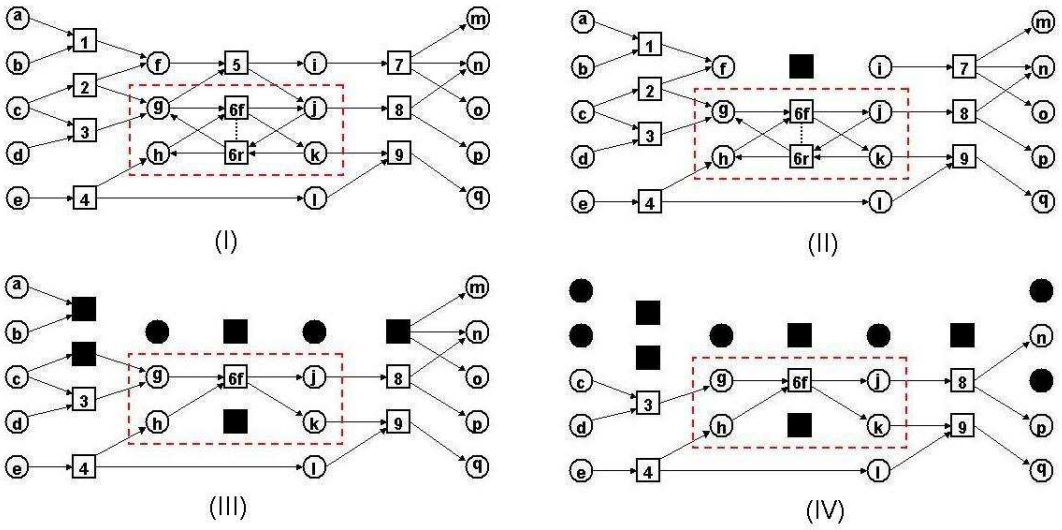

Figure 8.1. **The cascading failure algorithm.** (I) The metabolic network is represented as a bi-partite graph, with directed edges connecting metabolite nodes (circles) to reaction nodes (squares). Reaction 6 is reversible, and represented as a coupled pair of reaction half nodes. (II-IV) The removal of a single reaction node (5) has a cascading effect, resulting in the removal of several additional reactions and metabolite nodes, as well as the fixing of reaction 6 in the forward direction. (See Section 8.1.3 for an explanation regarding the treatment of reversible reactions)

A subtle, yet significant feature of the TFB failure algorithm is that it allows for bi-directional cascades. A reaction node deletion affects both its product and reactant metabolites, such that failure can cascade both forwards (towards products) and backwards (towards nutrients) along the network. This is biologically significant - assuming there are no alternative pathways, pathways that 'funnel' into a removed node are rendered non-operational, as are those that emanate from it.

8.1.3. A Note on the Treatment of Reversible Reactions

Reversible reactions give rise to a special problem – the TFB criteria fail if a metabolite node has incoming and outgoing edges connecting to the same reaction node. Consider a metabolite that is both fed and consumed exclusively by a single reversible reaction. Although the metabolite meets the TFB criteria, one can see that it and its associated reaction are effectively dead, since the reversible reaction must have zero net flux. Alternative approaches found in the literature are typically inadequate; they include treating reversible reactions as two separate reaction nodes (which gives rise to the same problem) and treating reversible reactions as directed reactions (which yields a less robust network) [**89**].

We resolve the reversibility anomaly by representing each reversible reaction as a coupled pair of *reaction half-nodes*, where one half-node is deleted if the topology of a neighboring node fixes the direction of positive reaction flux (See reaction 6 in Fig. 8.1). For example, if the lone incoming edge of a metabolite node is connected to the forward half-node of a reversible reaction, the reaction is necessarily fixed in the forward direction and the corresponding reverse half-node is deleted. This precludes the possibility for self-producing, self-consuming metabolites in the network.

8.2. Results – Cascade Damage

Failure cascades are initiated by the removal of a single reaction node (this may correspond to failure of a enzymes due to knockout or inhibition). The resultant cascade can be characterized by its total number of reactions killed, d_r (we refer to this as the *damage*).

For each network, we generate a cumulative distribution function (CDF), $P(d_r \geq d)$ – the probability that a random reaction node removal will produce a damage greater than or equal to d (see Fig. 8.2). This distribution characterizes the robustness of a network. Damage CDFs for *S. cerevisiae*, *E. coli*, *M. barkeri*, and *S. aureus* are similar: they are broad-tailed when plotted on linear axes (not shown), indicating that while most cascades are small ($\approx 90\%$ of cascades have $d_r \leq 10$), some are quite large (the largest cascades range from $d_r \approx 50$ to $d_r \approx 80$, depending on the species). These large failures represent catastrophic – and likely lethal – events, so that the behavior of the CDF at large d is of special interest. We find that the CDFs initially decay at a rate which is close to a power-law, but for large d they tend to tail off at a rate which is faster and closer to exponential decay.

What do these distributions signify? In part, they signify that the structures of these metabolic networks are exceptionally robust. We show below that large cascades in the metabolic network occur with much lower frequency than would be expected in a comparable, randomly wired network.

8.2.1. Metabolic vs. Randomly Wired Networks

We can identify the role of organization in the metabolic network – to either enhance or decrease robustness – by contrasting failure properties of real metabolic networks with randomly wired networks.

For each species, we construct randomly wired networks using the real metabolic network as the starting point. Pairs of edges are randomly switched, or rewired, conserving both node degree and edge orientation (k, k_{in}, and k_{out} for each node are the same as

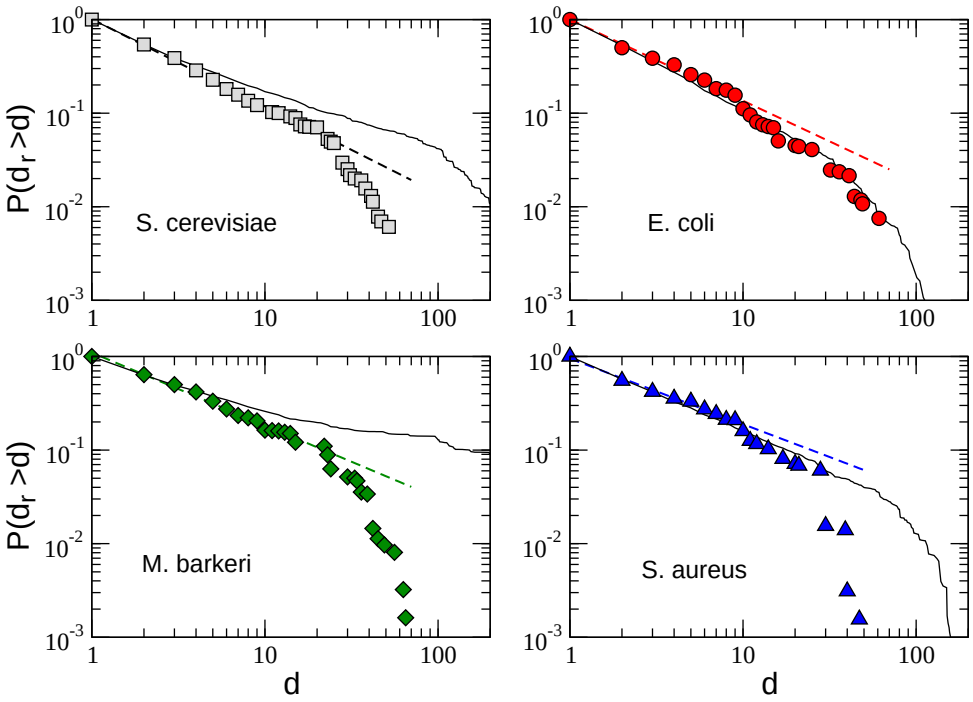

Figure 8.2. **Damage distributions** Damage probabilities are presented as Cumulative Distribution Functions, plotted on log-log axes. At small d, the CDFs tend to decay at a rate that is close to a power-law (dashed lines); at large d, they tend to tail off at a rate which is closer to exponential decay. With the exception of E.coli, the networks are less susceptible to large cascades than comparable randomly wired networks (solid lines), suggesting that organizational motifs present in the metabolic networks act to enhance robustness.

in the original metabolic network). A minimum of $100n_e$ switching moves are performed to ensure equilibrium, where n_e is the total number of edges in the network (switching is performed according to the method discussed in [**101**]). The resulting networks – like the corresponding real metabolic networks – have power law degree distributions, but – unlike real metabolic networks – lack organizational motifs.

We find that, for small cascade events, the randomly wired networks behave similarly to real metabolic networks (see Fig. 8.2). However, at large d, the CDFs of randomly

wired and real metabolic networks diverge – randomly wired networks are significantly more susceptible to large cascades (d_r larger than about 20). An exception is the *E.coli* network, which has nearly identical CDFs for its real and rewired versions. For the other species, the evidence suggests the existence of robustness-enhancing structural features. In the following sections, we attempt – via statistical analysis – to identify these features.

8.3. Rigid Clusters, Non-Rigid Branches

It is useful to distinguish metabolite nodes according to node degree: *uniquely produced–uniquely consumed (UPUC)* nodes have $k_{in} = k_{out} = 1$; *branching, susceptible* nodes have either k_{in} or $k_{out} = 1$; and *branching, non-susceptible* nodes have both k_{in} and $k_{out} > 1$. (We have adopted the term UPUC from [**93**].)

Consider a cluster of UPUC metabolite nodes adjoined by reaction nodes (i.e., a UPUC node feeds a reaction that has a UPUC product node, which in turn feeds another reaction that has a UPUC product node, and so on, see Fig. 8.3). This cluster displays the special property that if any of its reaction nodes are killed, the entire cluster will necessarily be killed; at minimum, a cascade will propagate until it is bounded by branched nodes. For this reason, we say that any cluster of nodes that does not contain a branched metabolite node is *rigid* (it follows that a *non-circular* cluster with n reaction nodes has $n - 1$ metabolite nodes, and every reaction node is part of a rigid cluster of at least size 1). A branched metabolite node, on the other hand is a non-rigid element, it may either propagate or halt a cascading failure, depending on the direction of propagation, and whether or not it is susceptible.

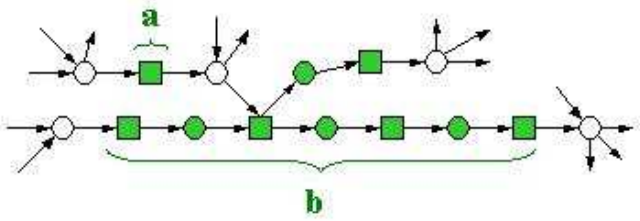

Figure 8.3. **Rigid clusters in the metabolic network.** The metabolic network can be decomposed into its rigid and non-rigid portions, where rigid portions, or clusters, are clusters of contiguous nodes that do not contain a branched metabolite node. In this example, a and b are rigid clusters of size $n_r = 1$ and $n_r = 5$, respectively. A rigid cluster has the distinguishing property that the removal of any of its nodes will necessarily 'kill' all remaining nodes in the cluster.

Rigid clusters in the metabolic networks analyzed here tend to range in size from 1 to about 20 reaction nodes. The cluster size CDF decays roughly as a power law – most clusters comprise just 1 or 2 reaction nodes, but a few can be large (see Fig. 8.4). Notably, the CDFs of the metabolic networks are similar to those of the corresponding randomly wired networks. This suggests that *no* organizing principle governs the clustering of UPUC metabolite nodes.

Next, we show that the random formation of rigid clusters approximates percolation on a Bethe Lattice.

8.3.1. A Bethe Lattice Model for Failure Cascades

The Bethe Lattice – an infinite tree consisting of self-similar branches – is a widely popular model for percolation problems (see Fig. 8.5). It is one of few lattices on which percolation can be solved analytically [**102**]. The key parameter governing percolation on the Bethe

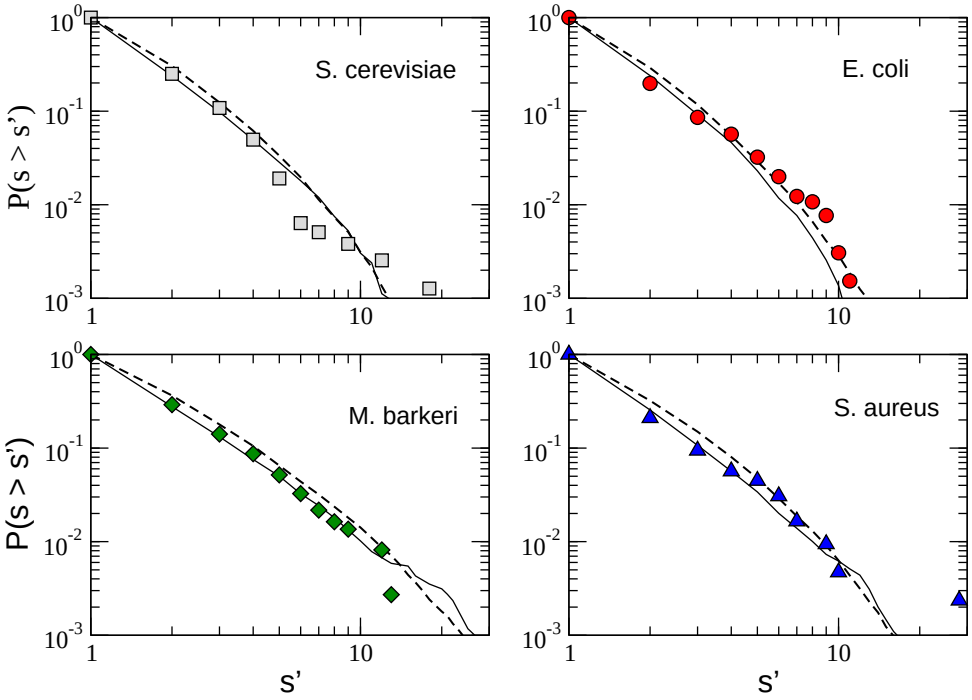

Figure 8.4. **Rigid cluster size distributions.** Rigid cluster size CDFs tend to decay at a rate close to power law. Notably, there is a relatively small difference between the cluster size distributions of real metabolic networks (data points) and their randomly rewired versions (solid lines). Notably rigid cluster formation in a randomly wired metabolic network can be accurately modeled as random percolation on a Bethe Lattice (dashed lines are the Bethe Lattice prediction), where all species have sub-critical composition ($\gamma < 1$).

Lattice is the branching parameter, b:

$$b = k - 1 \tag{8.1}$$

where k is the node degree. The branching parameter, in turn, determines the critical probability for percolation, ω^*:

$$\omega^* = \frac{1}{b} \tag{8.2}$$

If neighboring nodes are connected (i.e., their connecting edge is turned 'on') with probability ω equal to ω^*, the system is critical – clusters of connected nodes form with a size distribution that is scale-free, exhibiting power-law decay. Specifically, the probability, $p_{\omega^*}(s)$, of forming a cluster of size s is

$$p_{\omega^*}(s) \propto s^{-5/2} \tag{8.3}$$

Where s is the number of nodes in a cluster. This system can be characterized by a critical parameter, $\gamma = \omega/\omega^*$, which is equal to one at criticality. Systems with $\gamma > 1$ are *supercritical* – they yield an infinitely percolating cluster of connected nodes with a cluster size distribution that decays slower than power law. Systems with $\gamma < 1$ are *sub-critical*, and yield a cluster size probability curve that decays faster than power law. Specifically, the subcritical cluster size probability distribution, $p_\omega(s)$, is

$$p_\omega(s) \propto s^{-5/2} \exp(-s(\omega_e - \omega^*)^2) \tag{8.4}$$

(The above solutions are outlined in [**102**]).

Bond percolation on the Bethe lattice is analogous to rigid cluster formation in a metabolic network. Consider, for example, a metabolic network in which each reaction has two substrates and two products (i.e., each reaction node has degree, k_r, equal to 4). The reaction nodes correspond to nodes in the Bethe lattice, and – in this ideal case – produce self-similar branching (in modeling rigid cluster formation, the mean metabolite node degree is inconsequential). Two reaction nodes will be connected on a rigid cluster if they are connected by a UPUC metabolite node. The metabolite nodes in the metabolic network are equivalent to the edges on the Bethe lattice – a UPUC metabolite node

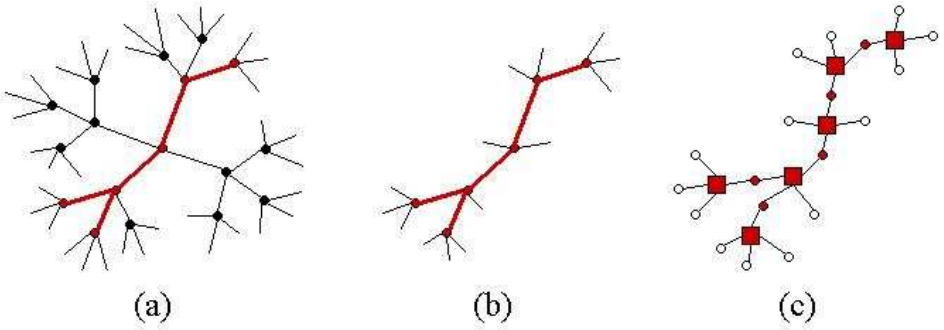

Figure 8.5. **Rigid cluster formation, modeled as percolation on a Bethe Lattice.** (a) A Bethe lattice with branching parameter, $b = 3$. Edges can be turned 'on' (red) with some probability, ω, producing various-sized clusters of connected nodes. (b) An isolated cluster on the Bethe lattice. (c) Rigid cluster formation on the metabolic network can be viewed in a similar manner: reaction nodes represent the nodes on the Bethe Lattice (squares), single-in-single-out metabolite nodes represent 'on' edges (filled circles), and branched metabolite nodes represent 'off' edges (outlined circles).

represents an edge that is turned 'on', while a branching metabolite node represents an edge that remains 'off'.

In the above example we have assumed that all reactions have identical degree. This closely approximates real metabolic networks, in which most reactions have k_r equal to 4 or 5, and variation in degree distribution is small. We therefore replace k in the Bethe Lattice model with the mean reaction node degree, $\langle k_r \rangle$. Thus, the key parameters for percolation of rigid clusters on a randomly wired metabolic network are:

$$b = \langle k_r \rangle - 1 \tag{8.5}$$

$$\omega^* = \frac{1}{\langle k_r \rangle - 1} \tag{8.6}$$

The probability, p_e of two reactions being connected by a UPUC metabolite node is equal to the number of edges connected to UPUC metabolite nodes divided by the total number of edges:

$$\omega = \frac{n_{e,UPUC}}{n_e} \tag{8.7}$$

The critical parameter, γ, for rigid cluster formation is then

$$\gamma = \frac{n_{UPUC}(\langle k_r \rangle - 1)}{n_e} \tag{8.8}$$

We find that each of the metabolic networks has a subcritical composition (see Table 8.1). Furthermore, the Bethe Lattice solution matches – with good agreement – the actual rigid cluster size distributions observed in both the real and randomly rewired metabolic networks (see dashed curve in Fig. 8.4).

This result (1) confirms our previous finding that the distribution of rigid cluster sizes in the metabolic network does not result from any particular organizing principle and also (2) validates the Bethe Lattice as a model for rigid cluster formation in metabolic networks. In the following section, we incorporate branching metabolites to construct a more complete picture of cascading failure.

Organism	$b\ (=\langle k_r \rangle - 1)$	$\omega\ (=n_{e,UPUC}/n_e)$	γ
E. coli	3.63	0.14	0.52
S. cerevisiae	3.47	0.16	0.54
S. aureus	3.80	0.16	0.61
M. barkeri	3.73	0.19	0.72

Table 8.1. **Key percolation parameters in the metabolic networks**.

8.4. Branching Structure in Metabolic Networks

A single cascade may comprise multiple rigid clusters. If a rigid cluster is connected to the *branch feeding* edge (either the lone incoming or lone outgoing edge) of a branched, susceptible node, it will produce a failure cascade that propagates to other rigid clusters. The probability, $P(n_s \geq n_s')$, that a failure cascade contains at least n_s' rigid clusters is broad-tailed – most cascades contain just one or two rigid clusters, but a few contain many (i.e., 20-40 rigid clusters, see Fig. 8.6). The observed $P(n_s)$ for metabolic networks is – by comparison to randomly wired networks – unusually small. This is particularly true in *S.cerevisiae*, *M.barkeri*, and *S. aureus*, for which random rewiring produces a significant probability for cascades with $n_s > 100$. The result suggest that branched nodes in metabolic networks are organized in a way that increases robustness. Furthermore, for all species except *E. coli*, the curve $P(n_s > n_s')$ for the randomly wired networks decays slower than power law (i.e., $d^2 \left[\log P(n_s > n_s')\right] / d \left[\log n_s'\right]^2 > 0$) suggesting that the metabolic composition may be supercritical with respect to branching.

8.5. Discussion

The species we have considered are found to be exceptionally robust; by decomposing failure cascades into rigid and non-rigid parts, we have shown that robustness derives primarily from the organization of the non-rigid parts. But E. coli is an intriguing anomaly. This may result from an incomplete in-silico reconstruction. Feist *et al.* have recently released an expanded genome-scale E. coli reconstruction, which has 2077 reactions and 1039 unique metabolites [**103**]. The updated E. coli model will possibly yield different cascading failure behavior.

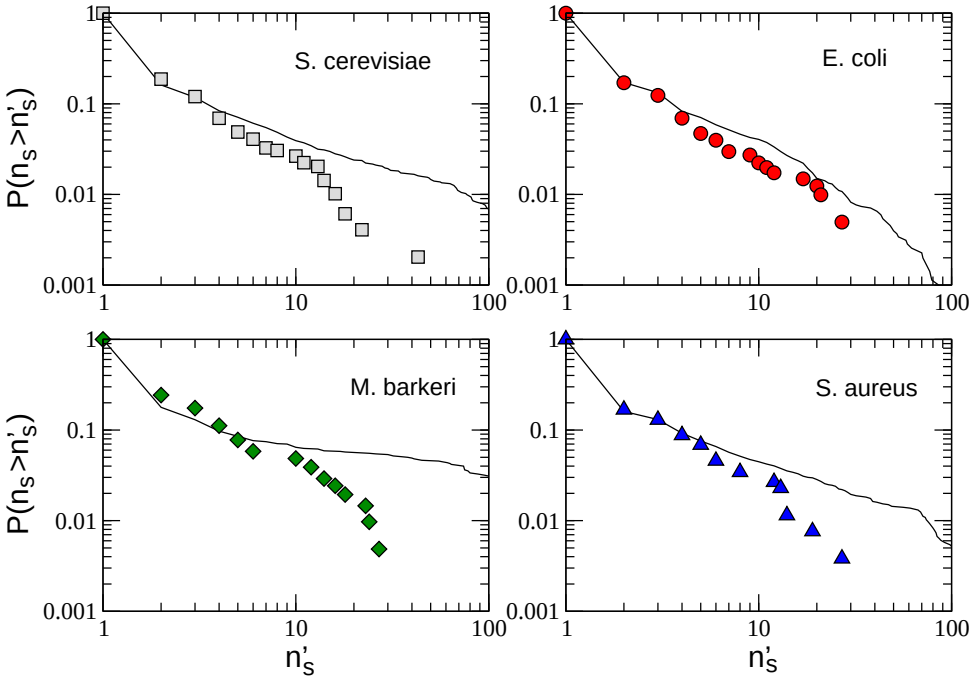

Figure 8.6. **Branch distributions.** The probability, $P(n_s)$, that a failure cascade in a metabolic network contains at least n_s rigid clusters is broad-tailed – cascades may contain as many $20-40$ rigid clusters, depending on the species. Random rewiring significantly increases the probability for large n_s – especially in the cases of *S.cerevisiae*, *M.barkeri*, and *S. aureus*. $P(n_s)$ for randomly wired versions are represented as solid lines.

The results of the current study are broadly significant. The Bethe lattice model – which we have used to predict rigid cluster formation – is a first attempt at mathematical modeling of failure in a metabolic network. It is likely that the Bethe lattice model can be adapted to include non-rigid portions of a cascading failure. This would be a powerful mathematical description of a system that, to our knowledge, has only been previously analyzed from an empirical standpoint.

CHAPTER 9

Looking Forward: Perspectives and Ideas for Future Studies

We have merely scratched the surface of what can be accomplished with network analysis. In Part I, we applied network tools to prototypical granular systems, but one can imagine that the same tools – loop analysis, path distance, etc. – might be extended and applied to a myriad of different granular systems with varying material properties and boundary conditions. In Part II we introduced a topology-based failure algorithm for the studying metabolic networks. This work may also have valuable extentions: cascading failure behavior may serve as a benchmark for testing various theories of metabolic organization.

9.1. Granular Networks: From Two to Three Dimensions

The analysis in Part I was limited exclusively to two-dimensional granular packings. An obvious extension is from two- to three- dimensions. In most cases, differences between two and three dimensional networks are quantitative, not qualitative. For example the distinguishing properties of granular networks – heterogeneity and self-organization – are present in both 2- and 3-D granular systems. Both 2- and 3-D packings exhibit exponentially decaying force distributions; both exhibit spatial correlations of forces.

A few properties change significantly: the packing fraction of randomly close packed disks is ≈ 0.82 for disks and ≈ 0.65 spheres; the maximum coordination number increases from 6 in 2-D systems to 12 in 3-D systems; and 3-D systems can assume a larger variety of

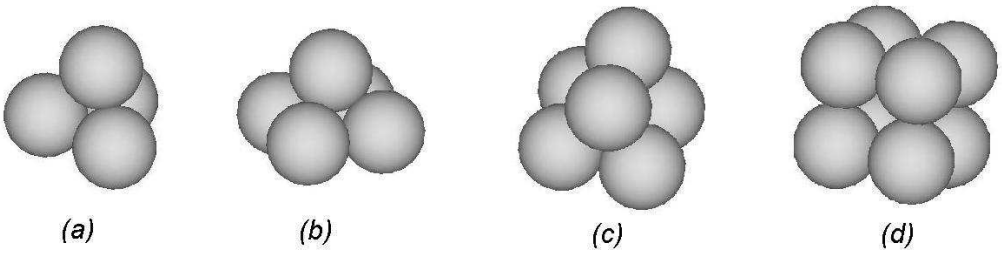

Figure 9.1. **Some minimal stable units in a 3-D granular packing.** (a) tetrahedron (b) square pyramid (c) triangular prism (d) cube. We define a minimal stable units as a structure that (1) can support 3-D perturbations of a compressive load, and (2) loses this robustness to perturbation if any one of its elements are removed.

packing structures. In some cases these differences have significant physical implications. For example, equipartition of pressure (Chapter 3) is observed over a large parameter space in 2-D systems, but not observed in 3-D systems [**55**]. But perhaps the area most enriched by the introduction of a third dimension is loop statistics (Chapter 4).

In two dimensions, contact loops are the smallest structures that can support a finite range of compatible loads. In three dimensions, the smallest stable structure – and the most common structure observed in real packings – is a tetrahedral arrangement (which has four particles and six contacts). We say that the tetrahedral structure is a *minimal stable unit* – if any of its elements are removed, the remaining structure is unstable to 3-D perturbations. Other such structures are likely present: square pyramids (5 particles, 8 contacts), triangular prisms (6, 9), and cubes (8, 12), among others (see Fig. 9.1). These minimal stable units – like loops in two-dimensions – may be viewed as the building blocks for a stable three-dimensional packing. Likewise, the concentration and types of minimal stable units may indicate fragility in three-dimensions.

9.2. Granular Networks: Looking at Mixed Systems

Part I, with the exception of Chapter 3 (Case I: Pressure in a Size Bi-disperse Granular Packing), deals with systems composed of nearly uniform particles. Only in Chapter 3 do we consider properties that arise in a disperse system of small and large particles. But dispersity – of size, shape, density and other material properties – may affect a much broader range of phenomena. For example, concentrations of the various loop structures (and minimal stable units, in 3-D) are likely to change with variations in size-dispersity. Little is known about the kind of loops present in a packing with bi-modal size distribution.

Mixing may have its most dramatic effect on transport. Consider a packing composed of particles of type 1, with uniform conductivities (k_1). If one of the particles is replaced with a second type of particle that has $k_2 \neq k_1$, the effective conductivity of the packing changes. But by how much? What is the effect of replacing a second particle? A third? We approximate such an experiment, replacing a single edge in the granular network with a 'superconducting' edge that has infinite conductivity, and measuring the overall gain in effective conductivity (see Fig. 9.2). From path distance analysis, it is clear that the change in conductivity depends not only on the properties of the substituted edge, but also on the structure of the surrounding force network. Currently, there is a limited capacity to understand the transport properties of a granular packing with a disperse distribution of conductivities, but network approaches may yield valuable insight.

9.3. Granular Networks: From Simulations to Experiments

With few exceptions, the granular networks discussed in this dissertation are generated by particle dynamics simulations (see Appendix). However, technological advances are

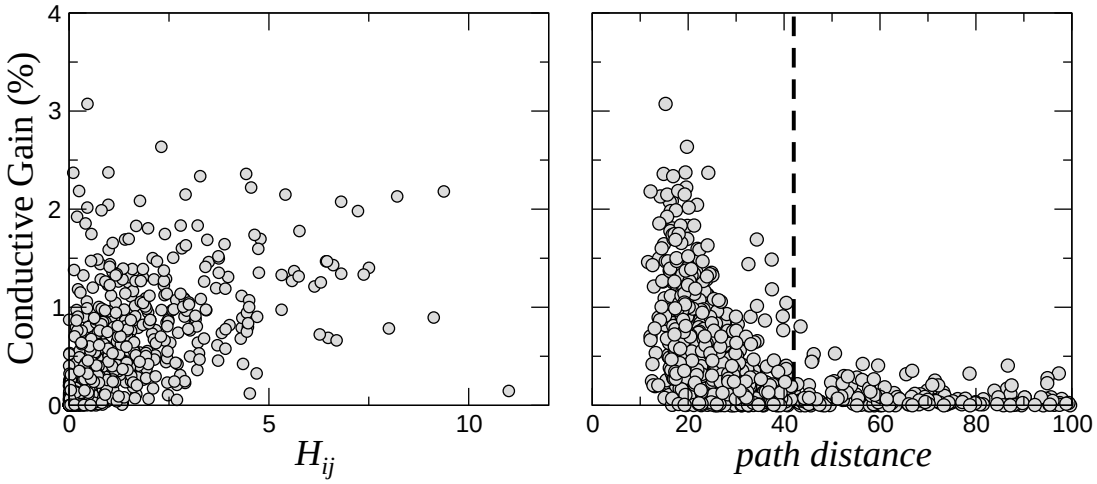

Figure 9.2. **Conductive gain in a granular network, when the conductivity of an edge is changed.** For each edge in the granular network, we calculate a single edge conductive gain – the increase in effective conductivity of the total network when the conductivity of that edge is set to infinity. We find that conductive gain is dependent not only the properties of the edge, but the organization of the surrounding network. (a) Conductive gain is weakly related to the conductivity, h_{ij}, of the replaced edge. (b) Conductive gain is inversely related to the distance of the mean shortest path connecting the edge to both walls – all edges with a conductive gain of greater than 1% lie on a path which is shorter than some threshold distance, which in this case is about 40 units (dashed line).

making it increasingly possible to obtain detailed, accurate granular networks from experiments. For example, constructing force networks using photoelastic disks has become an especially popular and effective technique [**40**]. Such tecniques may make it possible to extend the studies discussed in this dissertation to real granular systems. For example, much work has already been done regarding force distributions in a real packings, so an experimental study on pressure distributions in bi-disperse packings (as we have done numerically in Chapter 3) should be a feasible extension. Similarly, we expect that the contact structure of a tilted granular bed can be measured with sufficient accuracy to perform analyses similar to that of Chapters 4 and 5.

Perhaps the most intriguing translation from simulations to experiments is regarding the relationship between heat transfer and force structure (Chapter 6). Experiments have been done measuring heat flow and temperature profiles in granular sytems [**104**]. Likewise, there are numerous experiments measuring the force structure of granular packings (see Chapter 2). Although inferences between the two are often made, to our knowledge, no granular experiment has simultaneously measured heat flows and force structure. Such an experiment could provide new quantitative insights into the role of the granular force network as a transport medium.

9.4. Metabolic Networks: The Origins of Robustness

Several theories exist surrounding the organizational structure of metabolic networks. It has been separately suggested that metabolic networks are scale-free and structured similarly to the hub and spokes of the air transport system [**80**], that they are modular [**105**–**107**], that they are 'highly optimized' [**88**],and that they are hierarchical [**108**, **109**]. The cascading algorithm presented in Chapter 8 (Cascading Failure in Metabolic Networks) is an ideal testbed for examining these theories. For example, a first step has already been taken – we have shown that failure properties of the metabolic network are not recovered from the scale-free model. Our randomization, although it conserved scale-free structure, produced a dramatic change in robustness. To the same end, one can conceive randomizations that conserve other properties – modularity, hierarchy – in order to determine their impact on metabolic function.

References

[1] L.A.N. Amaral and J.M. Ottino. Complex networks. *The European Physical Journal B-Condensed Matter*, 38(2):147–162, 2004.

[2] J.M. Ottino. Engineering complex systems. *Nature*, 427(6973):399, 2004.

[3] J.M. Ottino. Granular matter as a window into collective systems far from equilibrium, complexity, and scientific prematurity. *Chemical Engineering Science*, 61(13):4165–4171, 2006.

[4] P. Bak and M. Paczuski. Complexity, Contingency, and Criticality. *Proceedings of the National Academy of Sciences of the United States of America*, 92(15):6689–6696, 1995.

[5] A.Q. Shen. Granular fingering patterns in horizontal rotating cylinders. *Physics of Fluids*, 14(2):462, 2002.

[6] P.B. Umbanhowar, F. Melo, and H.L. Swinney. Localized excitations in a vertically vibrated granular layer. *Nature*, 382(6594):793–796, 1996.

[7] SJ Fiedor and JM Ottino. Dynamics of Axial Segregation and Coarsening of Dry Granular Materials and Slurries in Circular and Square Tubes. *Physical Review Letters*, 91(24):244301, 2003.

[8] T. Mullin. Coarsening of Self-Organized Clusters in Binary Mixtures of Particles. *Physical Review Letters*, 84(20):4741–4744, 2000.

[9] P.M. Reis and T. Mullin. Granular Segregation as a Critical Phenomenon. *Physical Review Letters*, 89(24):244301, 2002.

[10] PM Reis, G. Ehrhardt, A. Stephenson, and T. Mullin. Gases, liquids and crystals in granular segregation. *Europhysics Letters*, 66(3):357–363, 2004.

[11] H.M. Jaeger, S.R. Nagel, and R.P. Behringer. Granular solids, liquids, and gases. *Reviews of Modern Physics*, 68(4):1259–1273, 1996.

[12] I. Newton. 1687. Philosophiae Naturalis Principia Mathematica. *London*, 1687:1972–1704.

[13] J.A. Papin, N.D. Price, S.J. Wiback, D.A. Fell, and B.O. Palsson. Metabolic pathways in the post-genome era. *Trends Biochem. Sci*, 28(5):250–258, 2003.

[14] AL Barabasi and E. Bonabeau. Scale-free networks. *Sci Am*, 288(5):60–9, 2003.

[15] J.H. Snoeijer, T.J.H. Vlugt, M. van Hecke, and W. van Saarloos. Force Network Ensemble: A New Approach to Static Granular Matter. *Physical Review Letters*, 92(5):54302, 2004.

[16] D. Deserable, P. Dupont, M. Hellou, and S. Kamali-Bernard. Cellular Automata Models for Complex Matter. *LECTURE NOTES IN COMPUTER SCIENCE*, 4671:385, 2007.

[17] R.F. i Cancho. The small world of human language. *Proceedings: Biological Sciences*, 268(1482):2261–2265, 2001.

[18] R. Guimera, S. Mossa, A. Turtschi, and L.A.N. Amaral. The worldwide air transportation network: Anomalous centrality, community structure, and cities' global roles. *Proceedings of the National Academy of Sciences*, 102(22):7794–7799, 2005.

[19] S. Milgram. The small world problem. *Psychology Today*, 2(1):60–67, 1967.

[20] P. Dantu. Contribution aıét mechanique et geometrique des milieux pulverulents. *Proc. 4th Int. Conf. Soil Mech*, 1:144–148, 1957.

[21] J. Duran and R.P. Behringer. Sands, Powders, and Grains: An Introduction to the Physics of Granular Materials. *Physics Today*, 54(4):63–64, 2001.

[22] C. Liu, S.R. Nagel, D.A. Schecter, S.N. Coppersmith, S. Majumdar, O. Narayan, and T.A. Witten. Force Fluctuations in Bead Packs. *Science*, 269(5223):513, 1995.

[23] H.A. Makse, D.L. Johnson, and L.M. Schwartz. Packing of Compressible Granular Materials. *Physical Review Letters*, 84(18):4160–4163, 2000.

[24] D.M. Mueth, H.M. Jaeger, and S.R. Nagel. Force distribution in a granular medium. *Physical Review E*, 57(3):3164–3169, 1998.

[25] G. Lovoll, K. Maloy, and E. Flekkoy. Force measurements on static granular materials. *Physical Review E*, 60:5872–5878, 1999.

[26] D.L. Blair, N.W. Mueggenburg, A.H. Marshall, H.M. Jaeger, and S.R. Nagel. Force distributions in three-dimensional granular assemblies: Effects of packing order and interparticle friction. *Physical Review E*, 63(4):41304, 2001.

[27] J.E.S. Socolar. Discrete models of force chain networks. *Arxiv preprint cond-mat/0212162*, 2002.

[28] S.N. Coppersmith, C. Liu, S. Majumdar, O. Narayan, and T.A. Witten. Model for force fluctuations in bead packs. *Physical Review E*, 53(5):4673–4685, 1996.

[29] L.E. Silbert, G.S. Grest, and J.W. Landry. Statistics of the contact network in frictional and frictionless granular packings. *Physical Review E*, 66(6):61303, 2002.

[30] A.V. Tkachenko and T.A. Witten. Stress in frictionless granular material: Adaptive network simulations. *Physical Review E*, 62(2):2510–2516, 2000.

[31] B.P. Tighe, J.E.S. Socolar, D.G. Schaeffer, W.G. Mitchener, and M.L. Huber. Force distributions in a triangular lattice of rigid bars. *Physical Review E*, 72(3):31306, 2005.

[32] AHW Ngan. Mechanical analog of temperature for the description of force distribution in static granular packings. *Physical Review E*, 68(1):11301, 2003.

[33] JD Goddard. On entropy estimates of contact forces in static granular assemblies. *International Journal of Solids and Structures*, 41(21):5851–5861, 2004.

[34] SF Edwards, DV Grinev, and J. Brujić. Fundamental problems in statistical physics of jammed packings. *Physica A: Statistical Mechanics and its Applications*, 330(1-2):61–76, 2003.

[35] C.S. O'Hern, S.A. Langer, A.J. Liu, and S.R. Nagel. Force Distributions near Jamming and Glass Transitions. *Physical Review Letters*, 86(1):111–114, 2001.

[36] E.I. Corwin, H.M. Jaeger, and S.R. Nagel. Structural signature of jamming in granular media. *Nature*, 435(7045):1075–1078, 2005.

[37] A.R.T. van Eerd, W.G. Ellenbroek, M. van Hecke, J.H. Snoeijer, and T.J.H. Vlugt. The tail of the contact force distribution in static granular materials. *arXiv:cond-mat/0702520v1*, 2007.

[38] T.S. Majmudar and R.P. Behringer. Contact force measurements and stress-induced anisotropy in granular materials. *Nature*, 435(7045):1079–82, 2005.

[39] F. Radjai, D.E. Wolf, M. Jean, and J.J. Moreau. Bimodal Character of Stress Transmission in Granular Packings. *Physical Review Letters*, 80(1):61–64, 1998.

[40] D.W. Howell, R.P. Behringer, and C.T. Veje. Fluctuations in granular media. *Chaos*, 9(3):559–572, 2006.

[41] J.S. Andrade Jr, H.J. Herrmann, R.F.S. Andrade, and L.R. da Silva. Apollonian Networks: Simultaneously Scale-Free, Small World, Euclidean, Space Filling, and with Matching Graphs. *Physical Review Letters*, 94(1):18702, 2005.

[42] SJ Friedmann, G. Kwon, and W. Losert. Granular memory and its effect on the triggering and distribution of rock avalanche events. *J. Geophys. Res*, 108(B8):2380, 2002.

[43] S.J. Friedmann, N. Taberlet, and W. Losert. Rock-avalanche dynamics: insights from granular physics experiments. *International Journal of Earth Sciences*, 95(5):911–919, 2006.

[44] J. Lee and HJ Herrmann. Angle of repose and angle of marginal stability: molecular dynamics of granular particles. *Journal of Physics A: Mathematical and General*, 26(2):373–383, 1993.

[45] N.A. Pohlman, B.L. Severson, J.M. Ottino, and R.M. Lueptow. Surface roughness effects in granular matter: Influence on angle of repose and the absence of segregation. *Physical Review E*, 73(3):31304, 2006.

[46] L.E. Silbert, D. Ertaş, G.S. Grest, T.C. Halsey, and D. Levine. Analogies between granular jamming and the liquid-glass transition. *Physical Review E*, 65(5):51307, 2002.

[47] A.S. Keys, A.R. Abate, S.C. Glotzer, and D.J. Durian. Measurement of growing dynamical length scales and prediction of the jamming transition in a granular material. *Nature Physics*, 3(4):260–264, 2007.

[48] L. Staron, J.P. Vilotte, and F. Radjai. Preavalanche Instabilities in a Granular Pile. *Physical Review Letters*, 89(20):204302, 2002.

[49] J.H. Snoeijer, W.G. Ellenbroek, T.J.H. Vlugt, and M. van Hecke. Sheared Force Networks: Anisotropies, Yielding, and Geometry. *Physical Review Letters*, 96(9):98001, 2006.

[50] C. Liu and S.R. Nagel. Sound in sand. *Physical Review Letters*, 68(15):2301–2304, 1992.

[51] X. Jia. Codalike Multiple Scattering of Elastic Waves in Dense Granular Media. *Physical Review Letters*, 93(15):154303, 2004.

[52] C. Liu and S.R. Nagel. Sound in a granular material: Disorder and nonlinearity. *Physical Review B*, 48(21):15646–15650, 1993.

[53] J.P. Maxfield. Telephone Transmitter, 1919. US Patent 1,296,683.

[54] R. Albert and A.L. Barabási. Statistical mechanics of complex networks. *Reviews of Modern Physics*, 74(1):47–97, 2002.

[55] O. Tsoungui, D. Vallet, J.C. Charmet, and S. Roux. Partial pressures supported by granulometric classes in polydisperse granular media. *Physical Review E*, 57(4):4458–4465, 1998.

[56] I. Hattori and H. Yamamoto. Rock Fragmentation and Particle Size in Crushed Zones by Faulting. *The Journal of Geology*, 107(2):209–222, 1999.

[57] H.A. Makse, S. Havlin, P.R. King, and H.E. Stanley. Spontaneous stratification in granular mixtures. *Nature*, 386:379–382, 1997.

[58] KM Hill, JF Gilchrist, JM Ottino, DV Khakhar, and JJ McCarthy. Mixing of granular materials: a test-bed dynamical system for pattern formation. *Int. J. Bifurcat. Chaos*, 9(8):1467–1484, 1999.

[59] KM Hill and J. Kakalios. Reversible axial segregation of binary mixtures of granular materials. *Physical Review E*, 49(5):3610–3613, 1994.

[60] RP Behringer, D. Howell, L. Kondic, S. Tennakoon, and C. Veje. Predictability and granular materials. *Physica D*, 133(1-4):1–17, 1999.

[61] G. Oron and HJ Herrmann. Exact calculation of force networks in granular piles. *Physical Review E*, 58(2):2079–2089, 1998.

[62] SF Edwards and CC Mounfield. A theoretical model for the stress distribution in granular matter. III. Forces in sandpiles. *Physica A*, 226(1-2):25–33, 1996.

[63] J. Geng, E. Longhi, RP Behringer, and DW Howell. Memory in two-dimensional heap experiments. *Physical Review E*, 64(6):60301, 2001.

[64] S. Deboeuf, O. Dauchot, L. Staron, A. Mangeney, and J.P. Vilotte. Memory of the unjamming transition during cyclic tiltings of a granular pile. *Physical Review E*, 72(5):51305, 2005.

[65] M.E. Cates, J.P. Wittmer, J.P. Bouchaud, and P. Claudin. Jamming, Force Chains, and Fragile Matter. *Physical Review Letters*, 81(9):1841–1844, 1998.

[66] R.C. Ball and R. Blumenfeld. Stress Field in Granular Systems: Loop Forces and Potential Formulation. *Physical Review Letters*, 88(11):115505, 2002.

[67] L. Staron and F. Radjai. Friction versus texture at the approach of a granular avalanche. *Physical Review E*, 72(4):41308, 2005.

[68] R. Gangopadhyay et al. Conducting polymer nanocomposites: A brief overview. *Chem Mater*, 12(3):608–622, 2000.

[69] K.E. Thompson and H.S. Fogler. Modeling flow in disordered packed beds from pore-scale fluid mechanics. *AIChE Journal*, 43(6):1377–1389, 1997.

[70] A. Smart, P. Umbanhowar, and J. Ottino. Effects of self-organization on transport in granular matter: A network-based approach. *Europhysics Letters*, 79(2):24002, 2007.

[71] G.K. Batchelor and R.W. O'Brien. Thermal or Electrical Conduction Through a Granular Material. *Proceedings of the Royal Society of London. Series A, Mathematical and Physical Sciences*, 355(1682):313–333, 1977.

[72] J.A. Greenwood and J.H. Tripp. The Elastic Contact of Rough Spheres. *ASME J. Appl. Mech*, 34:153–159, 1967.

[73] W.L. Vargas and JJ McCarthy. Heat conduction in granular materials. *AIChE Journal*, 47(5):1052–1059, 2001.

[74] W.M. Deen. *Analysis of transport phenomena*. Oxford University Press New York, 1998.

[75] N. Shah, J.E. Sax, and J.M. Ottino. Influence of morphology on the transport properties of polystyrene/polybutadiene blends. Pt. 2: modelling results. *Polymer*, 26:1239–46, 1985.

[76] M. Durand and D. Weaire. Optimizing transport in a homogeneous network. *Physical Review E*, 70(4):46125, 2004.

[77] V. Latora and M. Marchiori. Efficient Behavior of Small-World Networks. *Physical Review Letters*, 87(19):198701, 2001.

[78] E.W. Dijkstra. A note on two problems in connexion with graphs. *Numerische Mathematik*, 1(1):269–271, 1959.

[79] L.A.N. Amaral, A. Scala, M. Barthelemy, and H.E. Stanley. Classes of Small-World Networks. *Proceedings of the National Academy of Sciences of the United States of America*, 97(21):11149–11152, 2000.

[80] H. Jeong, B. Tombor, R. Albert, Z.N. Oltvai, A.L. Barabasi, et al. The large-scale organization of metabolic networks. *Nature*, 407(6804):651–654, 2000.

[81] R. Albert. Scale-free networks in cell biology, 2005.

[82] A. Wagner. The small world inside large metabolic networks. *Proceedings: Biological Sciences*, 268(1478):1803–1810, 2001.

[83] A.L. Barabasi and Z.N. Oltvai. Network biology: understanding the cell's functional organization. *Nature Reviews Genetics*, 5(2):101–113, 2004.

[84] R. Tanaka. Scale-Rich Metabolic Networks. *Physical Review Letters*, 94(16):168101, 2005.

[85] R. Mahadevan and BO Palsson. Properties of Metabolic Networks: Structure versus Function. *Biophysical Journal*, 88(1):7–9, 2005.

[86] M. Arita. The metabolic world of Escherichia coli is not small. *Proceedings of the National Academy of Sciences*, 101(6):1543–1547, 2004.

[87] H.W. Ma and A.P. Zeng. The connectivity structure, giant strong component and centrality of metabolic networks. *Bioinformatics*, 19(11):1423–1430, 2003.

[88] R. Tanaka, M. Csete, and J. Doyle. Highly optimised global organisation of metabolic networks. *Systems Biology, IEE*, 152(4):179–184, 2005.

[89] N. Lemke, F. Herédia, C.K. Barcellos, A.N. dos Reis, and J.C.M. Mombach. Essentiality and damage in metabolic networks. *Bioinformatics*, 20(1):115–119, 2004.

[90] J.S. Edwards and B.O. Palsson. Robustness Analysis of the Escherichia coli Metabolic Network. *Biotechnology Progress*, 16(6):927–939, 2000.

[91] M. Imielinski, C. Belta, A. Halasz, and H. Rubin. Investigating metabolite essentiality through genome-scale analysis of Escherichia coli production capabilities. *Bioinformatics*, 21(9):2008–2016, 2005.

[92] E. Almaas, B. Kovacs, T. Vicsek, ZN Oltvai, and AL Barabasi. Global organization of metabolic fluxes in the bacterium Escherichia coli. *Nature*, 427(6977):839–843, 2004.

[93] A. Samal, S. Singh, V. Giri, S. Krishna, N. Raghuram, and S. Jain. Low degree metabolites explain essential reactions and enhance modularity in biological networks. *BMC Bioinformatics*, 7(1):118, 2006.

[94] SA Becker and BO Palsson. Genome-scale reconstruction of the metabolic network in Staphylococcus aureus N315: an initial draft to the two-dimensional annotation. *BMC Microbiol*, 5(1):8, 2005.

[95] N.C. Duarte, M.J. Herrgård, and B.Ø. Palsson. Reconstruction and Validation of Saccharomyces cerevisiae iND750, a Fully Compartmentalized Genome-Scale Metabolic Model. *Genome Research*, 14:1298–1309, 2004.

[96] A.M. Feist, J.C.M. Scholten, B.O. Palsson, F.J. Brockman, and T. Ideker. Modeling methanogenesis with a genome-scale metabolic reconstruction of Methanosarcina barkeri. *Mol Syst Biol*, 2(2006.0004), 2006.

[97] J.L. Reed, T.D. Vo, C.H. Schilling, and B.O. Palsson. An expanded genome-scale model of Escherichia coli K-12 (iJR904 GSM/GPR). *Genome Biol*, 4(9):R54, 2003.

[98] T. Wilhelm, J. Behre, and S. Schuster. Analysis of structural robustness of metabolic networks. *Systems Biology, IEE*, 1(1):114–120, 2004.

[99] BA Carreras. Critical points and transitions in an electric power transmission model for cascading failure blackouts. *Chaos An Interdisciplinary Journal of Nonlinear Science*, 12(4):985, 2002.

[100] D.J. Watts. A simple model of global cascades on random networks. *Proceedings of the National Academy of Sciences*, 99(9):5766, 2002.

[101] R. Milo, N. Kashtan, S. Itzkovitz, MEJ Newman, and U. Alon. On the uniform generation of random graphs with prescribed degree sequences. *Arxiv preprint cond-mat/0312028*, 2003.

[102] Stauffer and Aharony. *Introduction to Percolation Theory*. Taylor and Francis, 1994.

[103] A.M. Feist, C.S. Henry, J.L. Reed, M. Krummenacker, A.R. Joyce, P.D. Karp, L.J. Broadbelt, V. Hatzimanikatis, and B.Ø. Palsson. A genome-scale metabolic reconstruction for Escherichia coli K-12 MG1655 that accounts for 1260 ORFs and thermodynamic information. *Molecular Systems Biology*, page 1, 2007.

[104] W.L. Vargas and J.J. McCarthy. Stress effects on the conductivity of particulate beds. *Chemical Engineering Science*, 57(15):3119–31, 2002.

[105] R. Guimera and L.A. Nunes Amaral. Functional cartography of complex metabolic networks. *Nature(London)*, 433(7028):895–900, 2005.

[106] R. Guimerà, M. Sales-Pardo, and L.A.N. Amaral. Classes of complex networks defined by role-to-role connectivity profiles. *Nature Physics*, 3(1):63–69, 2007.

[107] V. Spirin, M.S. Gelfand, A.A. Mironov, and L.A. Mirny. A metabolic network in the evolutionary context: Multiscale structure and modularity. *Proceedings of the National Academy of Sciences*, 103(23):8774–8779, 2006.

[108] E. Ravasz, AL Somera, DA Mongru, ZN Oltvai, and A.L. Barabasi. Hierarchical Organization of Modularity in Metabolic Networks, 2002.

[109] J. Gagneur, D.B. Jackson, and G. Casari. Hierarchical analysis of dependency in metabolic networks. *Bioinformatics*, 19(8):1027–1034, 2003.

[110] J. Schafer, S. Dippel, and D.E. Wolf. Force schemes in simulations of granular materials. *J. Phys. I France*, 6:5–20, 1996.

[111] P.A. Cundall and O.D.L. Strack. A discrete numerical model for granular assemblies. *Geotechnique*, 29(1):47–65, 1979.

[112] B.D. Lubachevsky and F.H. Stillinger. Geometric properties of random disk packings. *Journal of Statistical Physics*, 60(5):561–583, 1990.

[113] M. Lätzel, S. Luding, HJ Herrmann, DW Howell, and RP Behringer. Comparing simulation and experiment of a 2D granular Couette shear device. *The European Physical Journal E-Soft Matter*, 11(4):325–333, 2003.

APPENDIX A

Particle Dynamics

Particle dynamics (PD) is a powerful tool for studying granular systems. The technique is based on the methodology of molecular dynamics developed for the study of liquids and gases: a force model is used to calculate forces exerted on discrete particles, and ensuing particle motion is calculated by integrating Newton's laws of translational and rotational motion,

$$\frac{dv}{dt} = \frac{1}{m}\sum f_n \tag{A.1}$$

$$\frac{d\omega}{dt} = \frac{1}{I}r\sum f_s. \tag{A.2}$$

A.1. Force Model

We simulate granular systems with repulsive, dissipative contacts. These features are captured by the linear spring-dashpot model [**110**]:

$$f_n = -k_n\alpha_{ij} - \gamma_n\frac{d\alpha_{ij}}{dt} \tag{A.3}$$

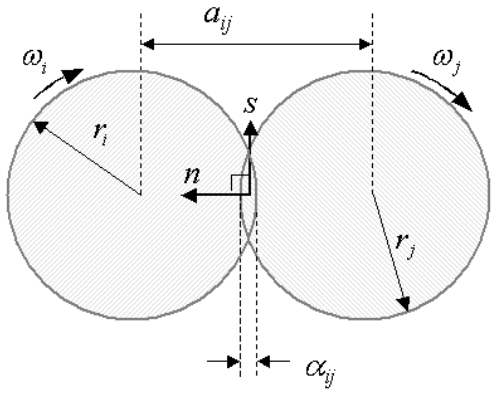

Figure A.1. **Definition of variables used in the PD force model.**

where k_n is the Hookean spring constant, γ_n is the dissipation term, and α is the inter-particle overlap,

$$\alpha_{ij} = max\left((r_i + r_j) - a_{ij}, 0\right). \tag{A.4}$$

so that f_n is zero for non-overlapping particles.

Frictional contacts may exert tangential force, i.e. transmit torque. Tangential forces are modeled using the Cundall and Strack method [**111**]:

$$f_s = -min\left(\left|k_s\zeta\right|, \left|\mu f_n\right|\right) \cdot sign(\zeta) \tag{A.5}$$

where k_s is the tangential stiffness, μ is the Coulomb friction coefficient, and ζ is the tangential displacement occur

$$\zeta(t) = \int_{t_o}^{t} v_s(t')dt' \tag{A.6}$$

Here, v_s is the relative tangential velocity between the two contacting particles.

The linear dashpot and Cundall and Strack models are among the simplest force models that capture the essential characteristics of granular contact: repulsion, dissipation, and friction. There are many others [**110**]. However, for systems like those considered in this dissertation, it can be shown that packing geometry is the primary determinant of force structure, and details of the force model (e.g. Hertzian vs. Hookean spring force) have little effect on the resulting force network [**29**].

A.2. System preparation

All granular packings are prepared via a three-stage procedure that is similar, in spirit, to the Lubachevsky-Stillinger method of producing jammed packings [**112**]. The first two stages in the preparation are always the same: (1) in the *initiation* stage, N point particles, with diameters equal to zero, are placed at random inside a box of prescribed width, L_x, and height, L_y; (2) in the *growth* stage, particles grow to their pre-specified sizes. In the growth stage, growing particles can collide, transferring small amounts of kinetic energy through dissipative collisions. Neither stage includes gravity as a body force.

The final stage in the preparation depends on the system considered. In Chapters 3 and 6, we investigate granular packings compressed between vertical walls, such that the final stage is a *compression* stage. A fixed force is applied to the vertical walls, compressing the granular system to a specified vertical pressure, P_y, and yielding a static, nearly isotropic granular packing. (Although the horizontal pressure, P_x, is not explicitly

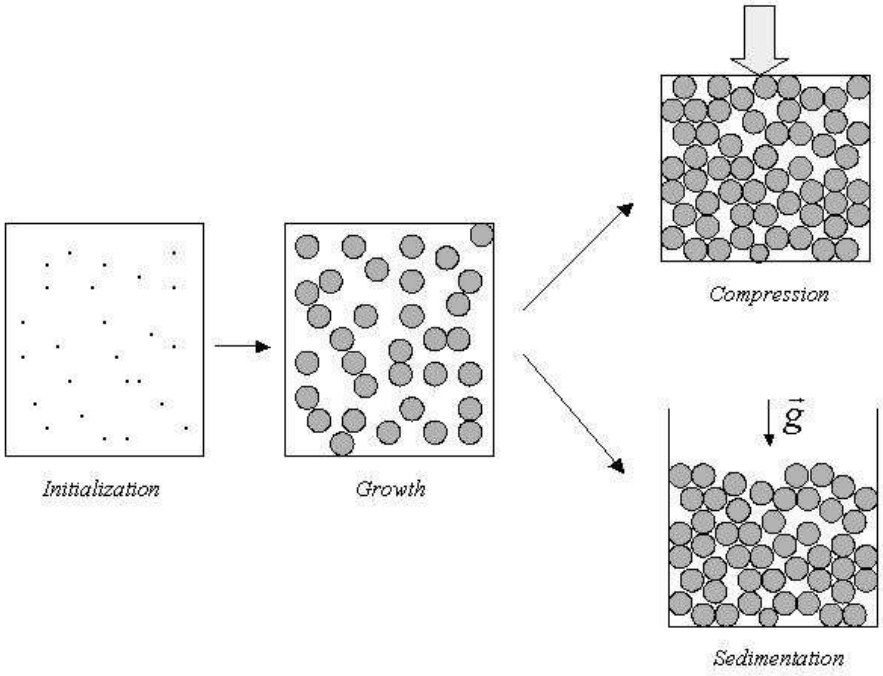

Figure A.2. **The three-stage preparation procedure.**

controlled, it tends to be nearly the same as the vertical pressure.) The final system dimensions approximate a square, with lengths $L_y \approx L_x = \overline{d}\sqrt{N}$.

In Chapters 4 and 5, we investigate a granular system tilted under gravity, such that the final stage is a *sedimentation* stage. Gravity is introduced and particles are allowed to settle, under their own weight, into an jammed state. The final dimensions approximate a rectangle, with $L_x \approx 5h$, where h is the bed height.

In all cases, simulations are ended when the system has sufficiently reached equilibrium. That is, the ratio of potential energy (E_p) to kinetic energy (E_k) is much greater than 1, for both translational and rotational energy. Typically, $E_p^{trans}/E_k^{trans} \approx 10^6$ and $E_p^{rot}/E_k^{rot} \approx 10^5$. The resulting packing fractions, $\phi = (L_x L_y)^{-1} \sum_{i=1}^{N} \pi(d_i/2)^2$, range from 0.800 to 0.801.

A.3. Outlook

With appropriate force models, parameters, and boundary conditions, PD models are capable of reproducing a wide range of granular phenomena, showing good qualitative and quantitative agreement with experimental results [**113**]. The result of a single PD simulation, however, is as specific as a single experiment - prediction is gained but understanding is not assured. The value gained from a PD simulation hinges on the techniques used to analyze its results. Network theory provides several insightful tools, as illustrated by the simulation cases presented in this dissertation.